Exploring the Feasibility of High Repetition Laser Ultrasound Non-Destructive Examination of Carbon Fibre Reinforced Polymer Composites

Shyam Dhulkhed

A Thesis

in

The Department

of

Mechanical and Industrial Engineering

Presented in Partial Fulfillment of the Requirements

for the Degree of Master of Applied Science (Mechanical Engineering) at

Concordia University

Montreal, Quebec, Canada

December 2016

© Shyam Dhulkhed, 2016

Concordia University

School of Graduate Studies

This is to certify that the thesis prepared

By: Shyam Dhulkhed

Entitled: Exploring the Feasibility of High Repetition Laser Ultrasound Non-Destructive Examination of Carbon Fibre Reinforced Polymer Composites

and submitted in partial fulfillment of the requirements for the degree of

Master of Applied Science (Mechanical Engineering)

complies with the regulations of the University and meets the accepted standards with respect to originality and quality.

Signed by the final Examining Committee:

_____ Chair

Dr. Ali Akgunduz

_____ Examiner

Dr. Mehdi Hojjati

_____ Examiner

Dr. Ashutosh Bagchi

_____ Supervisor

Dr. Sivakumar Narayanswamy

Approved by _____

Chair of Department or Graduate Program Director

_____ 2016 _____

Dean of Faculty

Abstract

Exploring the Feasibility of High Repetition Laser Ultrasound Non-Destructive Examination of Carbon Fibre Reinforced Polymer Composites

Shyam Dhulkhed

This thesis reports a reliable approach for Non-Destructive Examination (NDE) of the composite structure to inspect delamination with lasers, inspired by the conventional ultrasonic testing technique. This novel technique consists of a setup wherein a target is subjected to a calibrated mechanical stress, generating compressional and shear waves that propagate within the laminate by a laser source. These waves reflect off the back surface or if they encounter a discontinuity. Such a mechanism can be obtained by shock/stress waves induced by a laser that generates a high strain rate. The laminates are subjected to a wide range of duration and amplitudes of impact using lasers, according to the properties, particularly geometrical and mechanical. Coupled with the measurement of velocity/displacement of the free surface and the surface of impact, the study provides the understanding of the real-time diagnosis of a possible delamination consequent to the mechanical effects of the impact. The simulation validates the characteristics of the loading and material, in correlation with the experimental results, and postulates the complete cognisance of interpretation of results. The numerical study reveals constraints and propagation of stress waves within the target, and allows for quantification of the existence of a delamination and its depth. The relation between the displacement/velocity results and the material properties, to characterize the depth of delamination is established. The experiments are conducted on carbon/epoxy composite laminates with and without delamination at different depths. The delamination in the laminates is introduced using an aluminium foil. The experiments are conducted in the testing arrangements similar to conventional technique(s). An optical phase modulation system is used to capture the ultrasonic signals arriving as shock/stress waves. It is also reported how the numerical model can be used as a predictive tool for the rapid estimation of the shock/stress propagation, to carry out a feasibility of NDE by varying the laser parameters. One such variation is achieved for a laser that has high repetition rate and low energy. All the investigations reveal certain possibilities and some associated challenges, which are explained by the theoretical and numerical means. These observations are useful for a user to come to a resolution on adapting this technology.

Acknowledgements

With the support and motivation that I have always been garnering from my parents Mrs. and Mr. Dhulkhed, my sister Ms. Sushma Dhulkhed, and all the dearest ones, the academic pursuits have become an endeavour for me.

I would sincerely express my gratefulness to Dr. Sivakumar Narayanswamy, my supervisor, and advisor, whose diligent encouragement, constant financial support, unfaltering faith and friendship have been an important part of my research throughout my graduate studies at Concordia University.

I would like to extend my gratitude to the members of committee – Dr. Ali Akgunduz, Dr. Ashutosh Bagchi, and Dr. Mehdi Hojjati for their willingness to participate in my thesis defence and for spending their valuable time in perusing this thesis.

A special thanks to Mr. Viwek Vaidya, for continuously encouraging me to pursue the research work in the field of non-destructive testing. I extend my humble gratitude and appreciation to Dr. Marc Choquet for allowing me to use the state of the art facility to carry out the experiments at Tecnar Automation Ltée, and for mentoring me during my investigations. My sincere appreciation to Mr. Jean-David Grenon for assisting me during the experimental study at Tecnar Automation Ltée.

Last but not the least; I extend my deepest thanks and appreciation to my friend Ms. Jennifer Pepler Quinn, for her continuous encouragement, as well as unselfish willingness to translate some of the literature written in the French language to English. With her help, I could find highly relevant and beneficial technical information from the published work.

Contents

List of figures

List of tables

Nomenclature

Φ	laser irradiation power density/intensity	$W.cm^{-2}$
e	incident energy	J
τ	duration at half maximum of the pulse	s
S	irradiated surface	cm^2
l_{skin}	thickness of skin which experiences an electronic heat	µm
λ	radiation wavelength	µm
K_L	imaginary part of the complex refractive index of the material	--
e_t	ablated thickness	m
K	thermal diffusivity	$m^2.s^{-1}$
C_t	thermal conductivity of the material	$W.K^{-1}.m^{-1}$
ρ	density of the material	$kg.m^{-3}$
C_v	specific heat capacity	$J.kg^{-1}.K^{-1}$
$P(r,t)$	incident pressure as a function of time and the radial distance	GPa
$P(r)$	normalized spatial energy profile of laser beam as a function of radial distance	GPa
$P(t)$	normalized time profile of pressure	GPa
P_{max}	maximum amplitude of pressure at the centre of irradiation	GPa
r	radial distance	mm
R	radius of the irradiated area	mm
P_{abl}	amplitude of incident pressure in direct regime	GPa
P_{conf}	amplitude of incident pressure in confined regime	GPa
α	proportion of energy of plasma transformed into thermal energy in interaction	--
Z	material acoustic impedance	$g.cm^{-2}.s^{-1}$
u	displacement of the surface	m
C_0	hydrodynamic speed of sound in the medium	$cm.s^{-1}$
E	modulus of elasticity	Pa
v	Poisson's ratio	--
L	latent heat of vaporization of the solid	$J.kg^{-1}$

ζ	material removal rate	$m.s^{-1}$
T_v	vaporization temperature	K
T_o	initial temperature	K
Δl	lattice parameter (mesh size)	m
Δt	Iteration time step	s
$F(t)$	load vector	N
$[M]$	mass matrix	Kg
$\{\ddot{x}\}$	acceleration vector	$m.s^{-2}$
$[C]$	damping matrix	$N.s.m^{-1}$
$\{\dot{x}\}$	velocity vector	$m.s^{-1}$
$[K]$	stiffness matrix	$N.m^{-1}$
$\{x\}$	displacement vector	m
G	modulus of rigidity	GPa
T_L	total thickness of laminate	mm
T_P	thickness of a carbon/epoxy ply	µm
T_I	thickness of an epoxy interply	µm

List of abbreviations

AOM	Acousto-Optic Modulator
BC	Berek Compensator
BFSD	Back Free Surface Displacement
BFSV	Back Free Surface Velocity
CFRP	Carbon Fibre Reinforced Polymer
FEM	Finite Element Method
FP	Fabry-Perot
FRP	Fibre Reinforced Polymer
GFRP	Glass Fibre Reinforced Polymer
HIP	Hot Isostatic Press
ILSS	Inter-Laminar Shear Strength
ISD	Impact Surface Displacement
ISV	Impact Surface Velocity
LASAT	Laser Shock Adhesion Test
LDV	Laser Doppler Vibrometer
LMML	Laser Metrology and Micromachining Laboratory
MOPA	Master Oscillator Pulse Amplification
NDE	Non-Destructive Examination
OOA	Out-of-Autoclave
PBS	Polarizing Beam Splitter
PD	Photo-Detector
PDL	Pulsed Detection Laser
PRC	Photo-Refractive Crystal
SNR	Signal to Noise Ratio
ToF	Time of Flight
TWM	Two-Wave Mixing

CHAPTER 1. Non-destructive examination of composites – an overview

1.1 Introduction

The first chapter discusses the problems associated with conventional Non-Destructive Examination (NDE) techniques, more particularly for composite laminates. Initially, the types of flaws that may be generated in composite laminates during fabrication are discussed. This follows a brief introduction to the existing flaw detection techniques. The advantages and disadvantages related to these techniques are narrated. The solution for these problems thus, requires the development and implementation of laser ultrasound NDE.

Laser ultrasound is further divided into two parts. The first being the generation of ultrasound, and the second part involving the optical detection of ultrasound. In the generation part, the laser impact and its theoretical and phenomenological phenomena is comprehensively discussed. This includes the explanation of different modes of ultrasound signal generation also known as modes of irradiation. This leads to an estimation of the magnitude of laser induced mechanical impact.

To understand the ultrasound detection part of this technique, some of the widely used optical detection techniques are introduced. For all the optical detection techniques, the associated advantages and disadvantages are briefly described.

With an awareness of the challenges in the conventional techniques, and the capability of laser ultrasound NDE to overcome these, the objectives of this thesis are defined. Lastly, framework of this thesis including thesis organization is provided in the first chapter.

1.2 Overview of composites

Composites, as the name suggests, are the materials made of two or more constituent materials. These materials possess different physical and/or chemical properties which when combined will have better properties and exhibit superior characteristics than what they would have been individually. This combination of two materials would make the composites possess significantly better mechanical properties, compared to other materials such as, metals. Some of the engineering composite materials are, concrete, fibre reinforced polymers, metal matrix composites, and ceramic composites.

Here, we shall limit our discussion to Fibre Reinforced Polymer (FRP) composites. The two main constituents of FRP composites are the reinforced fibres, and the polymer/matrix. The reinforced fibres or generally termed as fibres, are usually glass, carbon, and aramid with most industrial applications. The commonly used polymers, which are also termed as the matrix of the composite laminate, are - epoxy, polyester and vinylester.

Some of the fabrication techniques of FRP composites are as follows –

- Hand laminating (or wet lay-up) and autoclave processing of composites
- Filament winding and fibre placement
- Pultrusion
- Liquid composite molding

More details about these manufacturing techniques can be found in [Hoa 2009]. With the combination of fibres and matrix, the composites have following advantages over other materials [Armstrong] –

- Lightweight, high strength, corrosion resistance.
- Superior resistance to deformation for an applied normal stress.
- Possibility to tailor the mechanical properties, which are dependent on fibre orientation.
- Excellent 'strength to weight' and 'stiffness to weight' ratios.

Some of the limitations of FRP composites are –

- Very high raw material and manufacturing cost.
- Mechanical properties significantly reduce in the transverse direction [Erhard 2006].
- Lack of knowledge has limited the usage of FRP composites in many industries other than defence, aerospace, automotive, marine, and construction.

1.3 Flaws in composites and their effects

During the fabrication of FRP composites, it is very relevant to say that inappropriate parameters do influence the flaws to come up in the bulk of the material. These flaws are highly dependent on the processing characteristics of matrix. For example, epoxy as a matrix material is used in many aerospace structures made of composites, for which the strongly influencing processing characteristics are viscosity, resin flow, curing temperature, curing time, and degree of cure. When

the layers/plies are laid on one another, the appropriate consolidation of layers/plies requires good resin flow and compaction. Otherwise, the fabricated composite laminate(s) may very well contain a variety of flaws such as, delaminations, voids, interply cracks, resin-rich areas, or resin-poor areas (dry spots) [Adams 1988, and Wilby 2012]. Among all the flaws that are produced during the fabrication of FRP composites, the delaminations are seen as one of the most critical flaw for the composite laminate's mechanical properties. The reason for the delamination formation is the inability of the resin to flow due to lack of compaction pressure in an extensively oriented laminate. If the adhesion of plies is weak, the plies tend to separate, which forms a delamination. The flaw may also come from the poor trimming of the plies and poor ply lay-up, which influences fibre orientation. Flaws can also be produced owing to quality of raw materials.

More information on fabrication; flaws associated with the process, and their effects can be found in [Mallick 2007]. Some of the adverse effects of the above-mentioned flaws on FRP composites are posited below –

- With increase in void content, the Inter-Laminar Shear Strength (ILSS) decreases, often linearly. ILSS also decreases if the laminate contains internal micro-cracks and dry spots [Summerscales 1994].
- If, during the fabrication, any cracks are produced in the laminate, the growth of these cracks may cause a premature failure. Subsurface delaminations can also be the source of these cracks, which might occur when the laminate experiences any static or fatigue loads [Summerscales 1994].
- Dry spots increase the likelihood of premature failure as there is a possibility of stress concentration in these areas [Guild, 1978, Davy 1988, and Guild 1989 a].
- If curing of the matrix is insufficient, the presence of unreacted sites in the bulk of the material can lower the glass transition temperature. A reduction in this temperature reduces the endurance limit of the composite laminate during fatigue/creep loading [Guild 1989 b].

Taking cognisance of the sharp decline in intended performance of the FRP composites, the FRP composites need to be examined for flaws. It is indeed necessary to ensure that, the flaw detection techniques are reliable, robust, and cost effective, because manufacturing of FRP composites is expensive as well.

1.4 Existing flaw detection techniques

With the ever-increasing need for higher performance, the composite structures must qualify for the increasing quality standards when it comes to the volume/size of flaws produced during the fabrication. Unfortunately, the detection of these flaws is a challenging task, because flaws are hidden in the bulk of the structure. For that reason, a number of Non-Destructive Examination (NDE) techniques for the flaw detection have been proposed such as X-ray computer tomography, thermography, shearography, and ultrasonic methods [Kapadia 2006].

1.4.1 X-ray computer tomography/radiographic inspection

This technique involves the distribution of ionising radiation beams for the NDE of structures/specimen. For the case of composites, two radiation types are applicable: X-rays and Neutrons. In a material, certain portions of the specimen have different radiation absorption properties as compared to the overall specimen. Using radiography, the portions with different radiation absorption properties can be distinguished in the captured image. This image is obtained by the beam, when it is transmitted through the specimen. The set-up for this inspection is shown in Figure 1.1.

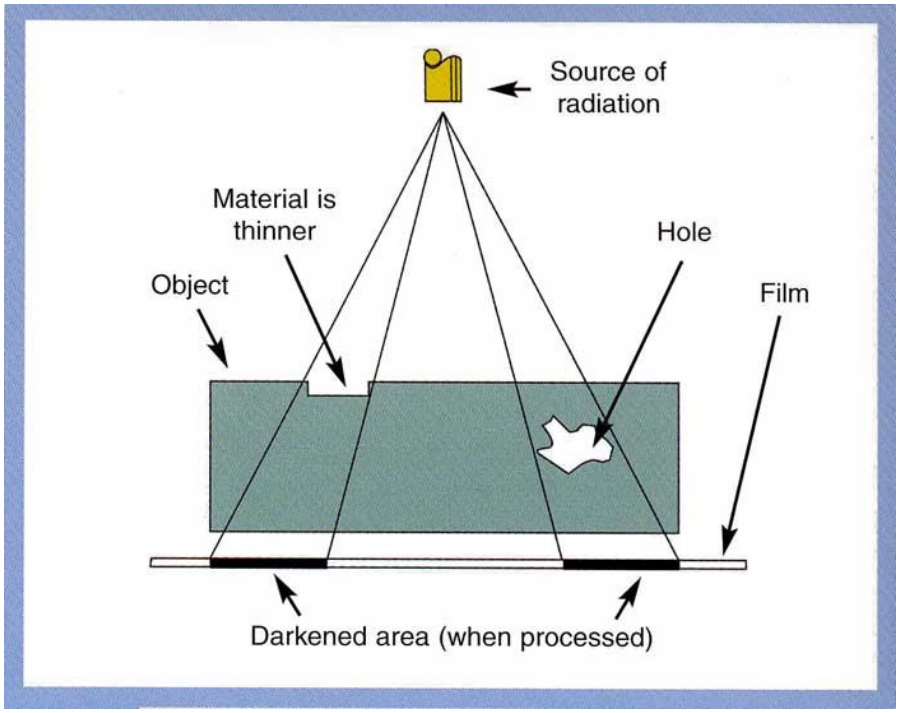

Figure 1.1: Schematic set-up of X-ray radiography test [Web link a].

Flaws such as, voids in composites can be detected, only if the voids reveal a 2% or more different absorption as compared to the surrounding material. Delaminations and cracks can be detected by the penetrant enhanced radiography, only if the flaws are open to the surface. Fibre volume fraction and fibre alignment of composites can be uncovered by enhanced radiography with radiation absorptive additives such as boron or glass (GFRP - Glass Fibre Reinforced Polymer). As the wavelength is notably shorter for X-rays, images with better resolution can be produced by radiography, as compared with other NDE techniques. Moreover, radiography has the capacity to inspect thicker sections than other techniques.

When a structure undergoes an in-service damage wherein the impact is largely composed of delaminations, X-rays are mostly not suitable for detecting them because of lack of resolution in the obtained image [Kapadia 2007]. One must also ensure that, the ionising radiation is carefully controlled during the inspection process, as the radiation is hazardous to health, which can damage body cells, and DNA molecules, leading to cancer [Brenner 2007]. Radiographic inspection would bear a considerable high cost compared to other NDE techniques. Radiographic methods are similar to a direct 'through transmission' image of the test specimen and hence cannot deduce the depth of flaws in a specimen unless further radiographic images are taken from different angles. To understand the radiographic images, extensive knowledge and experience is needed, as there are numerous types of artefacts seeming very similar to genuine flaws. The detector for the transmitted signals must be placed on the other side of the specimen, making the technique very difficult to be implemented on the structures, which are relatively big in size, and this technique is difficult to automate the inspection process [Lindgren 2013].

1.4.2 Thermography

It is a process wherein the flaws are detected in a structure by monitoring the flow of heat over the surface by an external temperature gradient. If the normal heat flow pattern is disrupted, as compared to what is expected in a flaw free structure, the presence of flaws in the structure is confirmed. This method of flaw detection is more sensitive and effective if the flaws are near to the surface of the structure. The basic set-up is shown in Figure 1.2.

Thermographic methods are further classified into two groups: active methods, and passive methods. In active methods, the thermal gradient is introduced and continuously maintained by

applying cyclic stress. In passive methods, the thermal gradient is established by a transient change. For the case of composites inspection, passive methods are widely used.

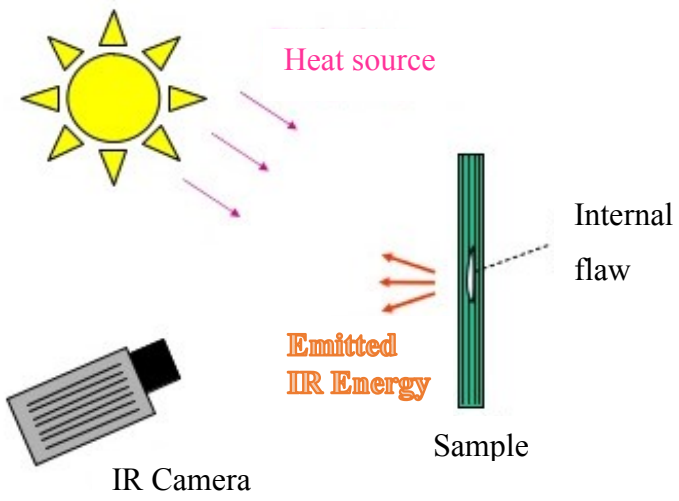

Figure 1.2: Experimental set-up for thermography [Web link b].

Flaws such as, inclusions, impact damage, voids, and cracks can be detected by thermography in FRP composites, and the translaminar cracks can also be detected. Care must be taken that, if the cracks are aligned parallel to the heat flow direction, they may not be detected. If the results obtained by the radiography and ultrasonic methods are difficult to understand, thermography can be substituted in composite NDE applications. An advantage of this technique is that, it can be used in applications where access from only one side of the test specimen is possible. Infrared cameras can give flexibility to be used from several metres, thus allowing remote sensing. However, the main disadvantage in applying thermography to inspect composites is that the anisotropy of the composite specimen that varies thermal properties with respect to the directions. The lightning protection mesh, which is present in some aerospace structures, can mask the observations. In addition, thermography requires the structure to be thermally conductive so that thermal radiation can propagate and heat transfer can be achieved, which is difficult in the case of Carbon Fibre Reinforced Polymer (CFRP) composites. As a drawback, the heating may induce thermal stresses, cause phase change, and initiate chemical reactions in certain structures. In addition to that, interpretation of results is a challenging task, especially in characterizing the depth of a flaw [Hung 2009, Garnier 2011, and Park 2014].

1.4.3 Shearography

This technique is an optical NDE technique, which provides observations about internal material discontinuities in non-homogenous materials. Figure 1.3 shows the basic set-up. A laser light is used by a shearing interferometer, to detect extremely small (sub-micrometre) changes in out-of-plane deformation of a surface. A proportional strain is induced on the test surface, as and when a test specimen is subjected to an appropriate load. The surface will undergo an uneven deformation at the locations where discontinuities are present. The shearing interferometer interprets this in terms of change in the phase of the laser light.

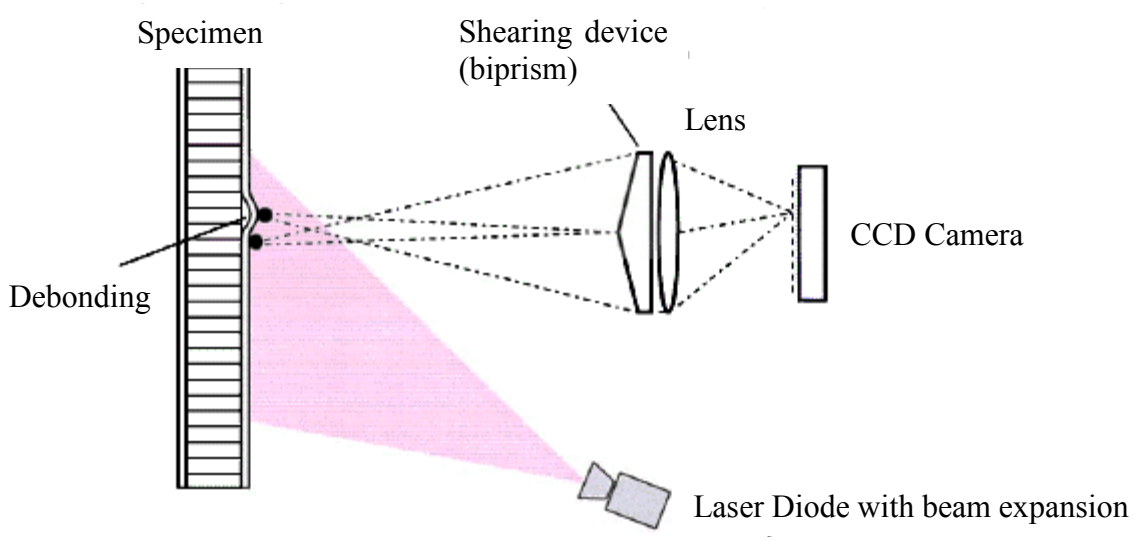

Figure 1.3: Basic Set-up for shearography [Mayer 2003].

Shearography can be used to scan the whole area of fuselages and wings from tripod positions or with the help of a vacuum stressing hood. The deformation can be achieved on test specimen by either in plane or out-of-plane stresses. To detect the surface-breaking and sub-surface flaws, such as barely visible impact damage, delaminations, and internal cracks, out-of-plane stressing is usually applied.

With a high degree of sensitivity, shearography enables non-contact inspections to be carried out very fast. However, to conduct the examination, the specimen must be loaded, which may damage the specimen. If the surface roughness is less than the order of one wavelength of light, shearography technique for NDE is invalid. Random interference will be produced if the surface of the specimen is smooth. The interpretation of result is complex, with respect to determining the depth of flaw. The result that is obtained is dependent on the lighting and the location of flaws,

requiring considerable experience to analyse [Steinchen 1998, Hung 2009, Garnier 2011, and Park 2014].

1.4.4 Ultrasonic methods

Ultrasonic methods are the most popular techniques of inspection for composites. For homogeneous materials, the usual frequency range during the inspection is between 20 kHz to 20 MHz. For composites, owing to their high attenuation and being prone to damages, the frequency range is reduced to anywhere between 5 MHz to 10 MHz. With reduction in frequency, it should also be noted that the ability of the ultrasonic wave to detect small flaws is minimized.

In most of the techniques, short ultrasound pulses (usually a few microseconds) are passed into the bulk of the composite material and detected to examine the structure. The examination is carried out with following techniques: pulse-echo, back scattering, through-transmission, and ultrasonic spectroscopy.

1.4.4.1 Pulse-echo

In this configuration, a pulse is directed normal to the testing surface of certain ultrasonic energy for typically a few microseconds. This pulse reflects from sound matrix-reinforcement boundaries and from the boundaries of flaws in the material. Figure 1.4 shows a typical pulse-echo set-up for a submerged immersion test.

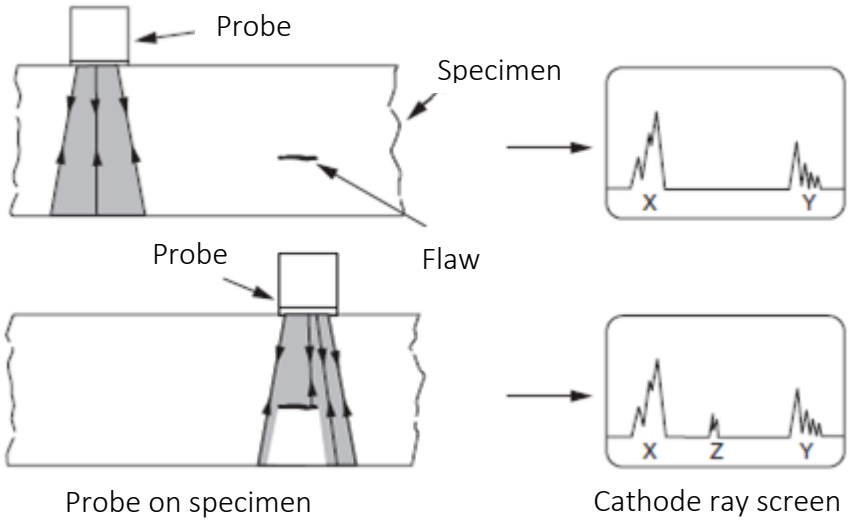

Figure 1.4: Immersion pulse-echo test with submerged specimen [Web link c].

The signals, which reflect towards the ultrasound-generating probe, are detected, and the features of the flaw, such as, depth, and size, are understood from the total pulse travel time or Time of Flight (ToF) and detected amplitude. In this 'A-scan' display, a series of peaks are formed, and the position of peaks along the horizontal axis can indicate the depth of flaw in the composite specimen. Each echo has certain amplitude, providing an indication of the size and nature of the reflector, which might be either a flaw or a specimen boundary. Alongside determining the depth and the size of a flaw, the technique can as well locate the flaw along the scanning axes. In the cases where, access to examine the composites is only from one side, this technique is quite useful.

1.4.4.2 Backscattering

This technique is a variation of pulse-echo, in which the transducer is inclined at an acute angle (α) to the normal direction of the surface of the test specimen. To detect the echoes, the transducer is rotated by the same angle about an axis normal to the surface. Figure 1.5 shows a typical backscatter set-up.

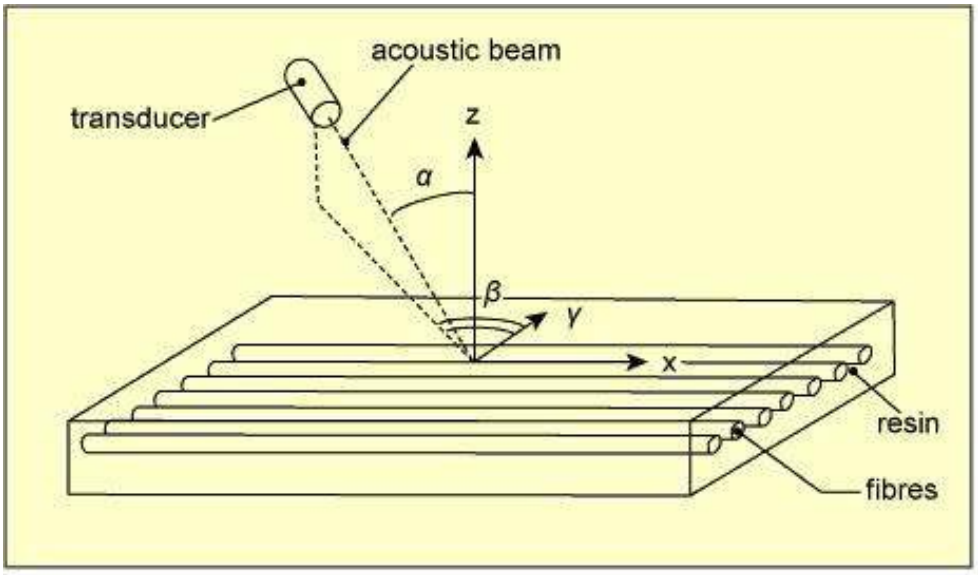

Figure 1.5: The backscatter technique [Kapadia 2006].

The backscattered signal reaches a maximum, when the angle of rotation (β) is such that, the transducer and the fibre direction are normal to each other in any of the layers of the specimen. A signal intensity versus the angle of rotation (β) plot is recorded. This method can also be set-up and implemented with a variable angle or with separated transducers for both transmission and reception. These transducers can as well be located on opposite sides of the specimen.

This technique is part of some of the very few methods to quality assure the ply lay-up sequence. However, the angle must be maintained accurately, because the orientation angle is very critical for successful examination, as this technique is very sensitive to the orientation of the fibres. To retain a proper alignment, a sophisticated setup is necessary.

1.4.4.3 Through-transmission

In through-transmission technique, typically two transducers are used: one to emit the signals and one to receive the signals. The receiving transducer would be placed on the opposite side of the test specimen facing the emitting transducer. It is at times termed as the 'obscuration' technique, because the total attenuation of signals happens within the material where the attenuation is affected by the features (flaws) that 'obscure' the beam. Examination of the attenuation can be derived between different specimens and between different locations of the same specimen.

Figure 1.6 shows a through-transmission immersion test in the jet probe set-up. A jet of water acts as a coupling agent, when projected on the surface of the test specimen for the ultrasound examination. Since, the water jet acts as the guide to ultrasound, the distance between the emitter transducer and the sample can be as long as the length of the water jet, also the misalignment of surface orientation can be tolerated.

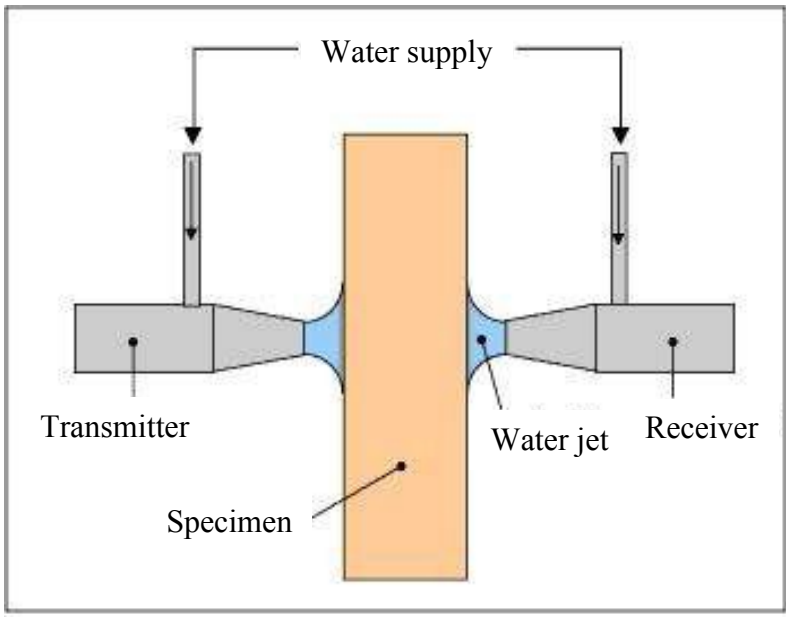

Figure 1.6: Immersion through-transmission test set-up implemented with jet probes [Kapadia 2006].

With this set-up, flaws at any depth can be located on the scanning axis, but the depth of the flaws cannot be known. Moreover, as the transmitter and detector must be well aligned, inspecting a specimen with a contoured surface is very difficult. In addition, access of the test specimen must be possible from both the sides, which might not be always possible.

1.4.4.4 Ultrasonic spectroscopy

In ultrasonic spectroscopy, the pulse is harmonically analysed when it is arriving at the detecting transducer. The recorded data can be deduced from characteristic changes to the frequency spectrum, concerning to the features within a composite specimen. This is illustrated in Figure 1.7, which shows a specimen being inspected in through-transmission set-up. A pulse-echo arrangement of this technique is also possible.

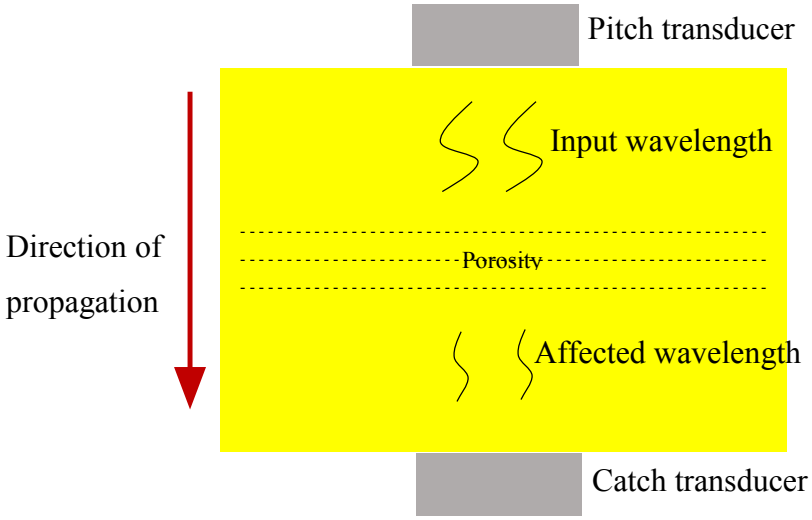

Figure 1.7: Wavelength interaction illustration for ultrasonic spectroscopy [Kapadia 2006].

To find out the thickness of thin test specimens, ultrasonic spectroscopy can be more effective than pulse-echo. This is because, for thin specimens, resolving the pulses reflected from the front and back-walls in the time domain it may not be easy. In addition, in the frequency domain, resolution of spectroscopy is much better as compared with pulse-echo, hence it is more likely that spectroscopy would be preferred. However, due to the signal attenuation in the material, the returning signal will definitely be affected, making it difficult to compare between different specimens, unless the signal attenuation is well known in both the specimen. In addition, a problem of poor Signal to Noise Ratio (SNR) would persist, as most of the techniques use a wide-band, pulsed input.

Although ultrasonic methods are very popular, they however have their own limitations [Krautkrâmer 1990, Garnier 2011, Schmerr Jr 2012, and Park 2014] –

- The need for trained and certified NDE personnel is required, as a high degree of operator skill and integrity is needed, because the signal amplitude is dependent on the thickness of the coupling fluid layer, which depends on the pressure applied by the probe on the fluid;
- The testing procedure may be heavily time consuming, especially for contoured parts;
- It requires a transducer to be in physical contact to the structure to carry out the examination, which limits the examination on structures whose surfaces are accessible and geometry is simple;
- A coupling medium is required to promote the transfer of sound energy into the test specimen;
- Inspection of materials that are rough, irregular in shape, very small, exceptionally thin or not homogeneous is difficult;
- Under harsh environments, such as varying pressure, high temperature and humidity or if the environment is radioactive, conventional ultrasonic techniques are neither feasible, nor as effective;

All of the above-mentioned limitations in the current techniques necessitate the introduction of laser-ultrasonics for NDE.

1.5 Theoretical and phenomenological description of the laser impact

The NDE of the targets using lasers can be achieved when, a high-energy ultrasound generation laser is projected on the test material, producing a high magnitude waves in the material. The energy of these waves propagates through the bulk of the material in the form of compressional waves and shear waves. These waves when they encounter a flaw such as a crack/void/delamination, a discontinuity in the wave propagation occurs, which prompts the waves to be reflected either partially or totally. This reflected wave is detected by a detection laser and the ToF or the change in phase is captured which gives an indication of the depth of flaw [Scruby 1990].

Many techniques reproduce the impact phenomena: explosive shock, impact plate, cannon etc. At an extreme stage of impact generation, the laser radiation generated by a short pulse (about ns duration), induces a strain rate of up to 107 s^{-1}, with laser induced pressure levels of up to 150 GPa

[Gay 2011]. The dynamic stress generation by high power laser was carried out in 1963 with the work of R. M. White [White 1963]. The technique is limited to the qualitative study of the strength of the interfaces of metal deposit [Yang 1974] and ceramics [Sarkissian 1978]. The diagnosis of free surface velocity measurement extends the test capabilities. Its implementation is done by C. S. Speight [Speight 1986], as per the principles established by L. M. Barker [Barker 1972].

The lack of suitable source to the process limited the applications until 80s, with the development and distribution of high-energy laser. Moreover, the advent of numerical techniques allows the possibility of simulation to understand the physical phenomena that is involved. The work on the laser induced waves increased, with the study of stress and damage of homogeneous metallic materials [Cottet 1988, Gilath 1989, Salzmann 1989, Eliezer 1990, Asay 1993, and Davison 2012].

Researching of thinly coated adherents by laser-induced waves was carried out by the team of V. Gupta in the 90's [Gupta 1990]. Optimization of wave parameters is described for the adhesion test of metal/ceramic interface [Gupta 1993 a, Gupta 1993 b, Yuan 1993 a, and 1993 b]. This research took place in 1995 leading to a patent describing the measurement of the force of an interface plane. This process is then applied to other pairs of metallic materials in experimental and numerical work [Boustie 1991 b, and Zhou 2003].

In the early 2000s in France, the laser shock related studies are oriented towards industrial application of the process, with the project Laser Shock Adhesion Test (LASAT) [Gay 2011]. It describes the testing of adhesion of the deposit material, and modelling the associated physical phenomena [Bolis 2007], the influence of interface flaws, and thicknesses of coated materials [Arrigoni 2006 a]. In these studies, the analysis of material velocity profiles can quantify the variables related to adherence. Heterodyne velocimetry, which is a material surface velocity measurement technique that has been developed and used in this study [Mercier 2009].

There is significant amount of studies concerning the laser impact on anisotropic materials [De Rességuier 2005], multilayer materials [Arrigoni 2008 a, and Radhakrishnan 2008] to name a few. Finally, applications are extended to the biomedical field with the study of adhesion between cells and biomaterial [Shim 2008], revealing the potential of this technique. The adhesion test using lasers was compared with other conventional tests [Arrigoni 2006 a, and Arrigoni 2006 b], and lasers offer consistent performance in terms of adhesion discernment.

A noncontact laser ultrasonic generation of surface acoustic wave signals in a metallic specimen was conducted, to characterize the acoustic nonlinearity in aluminium (Al. 6061) and steel (A36) [Swacek 2013]. An enhancement in lamb waves, with respect to the frequency content, using an all-optical laser-ultrasonics method was carried out for the diagnosis of machined flaws, and to detecting stress corrosion cracking [Clough 2013]. A remote, non-contact technique based on laser-ultrasound for analysing deterioration of concrete structures in high-accuracy safety surveys was carried out, wherein the measurement of the depths of artificially created surface cracks was performed [Kurahashi 2013]. The experimental measurement using laser generation and detection of ultrasound on machined slots with varied geometries, including the flaws that are normal or inclined to the surface was presented, and the experimental results were compared with the results from Finite Element Method (FEM) [Hernández-Valle 2013]. The successful development of laser shockwave technique for characterizing the interface strength between Hot Isostatic Press (HIP) bonded aluminium cladding and the fuel foil using depleted Uranium/Mo foils was carried out [Perton 2013]. A study has been conducted on the strength of bonding of CFRP composite laminates using laser shock waves [Ecault 2013, and Gay 2014 a]. To improve the efficiency of laser ultrasonics, a robotic inspection system has been introduced, with a specific objective of inspecting massive composite structures used on aircrafts [Néron 2013].

The resonant amplification of the high power laser induced surface acoustic waves was done, using phase velocity scanning, to maintain a dynamic range, so that a high amplitude waves can be detected for a clear evaluation of flaws [Sherman 2013]. Laser-ultrasonic techniques for non-contact generation and detection of high frequency ultrasound on a local scale are high power methods, which limits the spatial information that can be accessed from a measurement due to optical diffraction. In order to improve the lateral spatial resolution, an aperture-less near-field scanning microscope was incorporated into laser-ultrasonics for local detection of laser generated ultrasound [Ahn 2013].

The shock/stress waves are generated with a high power pulsed laser, by focusing the beam on a target surface, causing irradiation intensity of the order of $GW.cm^{-2}$. This energy is absorbed by the material over a small thickness, which is vaporized and sublimed in plasma within a few picoseconds. The rapid expansion of the plasma produces a short load pressure as a reaction. The mechanical properties of materials have a high dependence on strain rate, with an increase of

dynamic behaviour up to a factor of 5, compared to the quasi-static regime [Gay 2011]. It is hence, imperative to take into account the dynamic nature of behavioural characteristics and damage. The following section describes the process of generation and propagation of the waves due to shock, and its mechanical consequences.

1.5.1 Generating shock waves by pulsed laser

The study of laser-matter interaction is initiated in the 60s [White 1963, and Askar'yan 1963]. The pulsed regime gives reference to many studies, either in vacuum or in the air [Fox 1974, and Phipps 1988], with a confinement [Fabbro 1990, Devaux 1993, and Berthe 1997] and quantifies the relationship between the characteristics of the laser pulse (wavelength, pulse duration, confinement medium).

The laser-matter interaction is based on the transformation of the photon energy into mechanical energy. Irradiation is quantified by the power density or intensity Φ, expressed in W.cm^{-2} by (1.1),

$$\phi = \frac{e}{\tau . S} \tag{1.1}$$

where e is the incident energy (J), τ the duration at half maximum of the pulse (s), and S the irradiated surface (cm²). The intensity has an amplitude of 10^7 to 10^{12} W.cm^{-2} in ns regime.

The thermomechanical phenomena governing the generation of a laser shock are broken down into three chronological process: absorption, thermalization, and conduction [Scruby 1990, and Gay 2011].

- In absorption, the photon flux is absorbed by valence free electrons (less energy). The slowdown of photons by inelastic interaction with said electrons produces an electronic heat in a small volume of material to a depth called, thickness of skin, l_{skin}, expressed in µm by (1.2) [Rozmus 1990],

$$l_{skin} = \frac{\lambda}{2.\pi . K_L} \tag{1.2}$$

  where λ is the radiation wavelength (µm), and K_L the imaginary part of the complex refractive index of the material. The skin depth of an aluminium target subjected to a laser shock of wavelength λ = 1.06 µm is l_{skin} = 16.5 nm.

- Thermalization is the step during which the electric energy is converted into thermal energy by a collision between electrons and ions. This process, at a characteristic time of 20 ps for metals, is the balancing of temperature differences between the electrons and the lattice, causing the surface phase change (melting, vaporization, plasma). The temperature gradient within the plasma causes the transfer of the absorbed energy to the solid material by thermal diffusion.
- The conduction of this heat energy into the material supports the expanding plasma and ends the process of interaction. These phenomena consecutive to phase changes lead to the ablation of a thin layer of material, of the order of micrometer.

This ablated thickness is estimated in (m) by equation (1.3), and it increasing with an increase of pulse duration:

$$e_t = \sqrt{K.\tau} \tag{1.3}$$

where $K = C_t/\rho.C_v$ is the thermal diffusivity ($m^2.s^{-1}$) and τ the pulse duration (s). With C_t the thermal conductivity of the material ($W.K^{-1}.m^{-1}$), ρ the density ($kg.m^{-3}$) and C_v the specific heat capacity ($J.kg^{-1}.K^{-1}$). The relaxation of the plasma induces the compression of the material in reaction, its briefness causes a pressure peak which radiates a shock wave from the first instant of its propagation.

These phenomena differ in sub-picosecond regime. The material is heated at the end of the laser radiation, due to the thermalization time (20 ps in metals). The ablation of the material generates a pulse of a duration of a few ps, subjected to a significant hydrodynamic damping during propagation.

The analytical study of laser-matter interaction quantifies the conversion of optical energy of the incident beam into mechanical energy. The incident pressure P is given by, (1.4) as a function of time t and the radial distance r from the centre of the area under stress therefore is considered as axisymmetric [Gay 2011].

$$P(r,t) = P_{\max}.P(r).P(t) \tag{1.4}$$

Where P_{max} is the maximum amplitude of pressure at the centre of irradiation, $P(r)$ the normalized spatial energy profile of the focused beam as a function of the radial distance, r, with the centre of

the impact, and *P(t)* the normalized time profile of pressure. *P(t)* can be calculated from the profile of the laser pulse raised in ns regime by a fast response photodiode (<200 ps). The radial profile *P(r)* indicates the geometric dispersion of the beam, more energy in the centre than at the periphery [Gay 2011]. Its normalized expression is estimated by (1.5):

$$P(r) = \sqrt{1 - \frac{r^2}{R^2}} \tag{1.5}$$

where R is the radius of the irradiated area. The amplitude of the incident pressure P_{max} and its temporal characterization *P(t)* depend on the confinement of the radiation, in order to increase the pulse duration and pressure. The laser-matter interaction is then governed by the direct interaction regimes (or ablation system) and confined regime, whose principle is shown schematically in Figure 1.8.

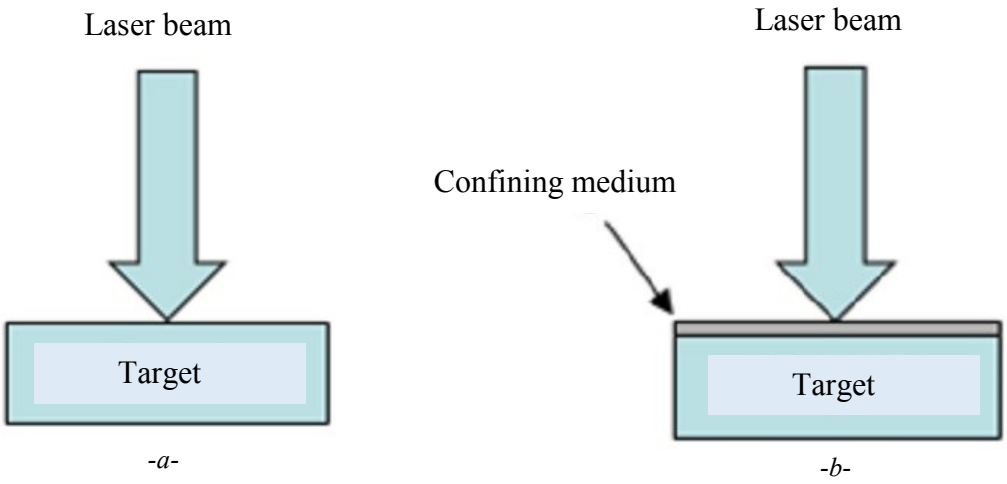

Figure 1.8: Laser-matter interaction: -a- direct ablation regime, and -b- confined regime.

The ionization potential in the confinement medium undergoes the action of an important energy flow beginning with a loss of transparency and partial absorption of the total incident energy. This phenomenon, called breakdown, is favoured by long pulses and short wavelengths [Berthe 1997]. The breakdown threshold is about 3 and 9 GW.cm^{-2} respectively in air and water for a wavelength of 1064 nm [Gay 2011].

1.5.1.1 Irradiation in direct mode

The amplitude of incident pressure P_{abl} in direct regime is given by (1.6) [Harrach 1982],

$$P_{abl} = K.\phi^m.\lambda^n.\tau^p \tag{1.6}$$

where Φ is the absorbed laser intensity, λ its wavelength, τ the pulse duration, K, m, n, and p the parameters dependent of the irradiation conditions and the irradiated material.

Grün's formula (1.7) [Grün 1981] quantifies the parameters of this expression for a pulsed laser of 1.06 microns wavelength on a polystyrene surface. This empirical relationship is validated by experiment over a wide range of materials (polymers, metals etc.).

$$P_{abl} = 1440.\phi^{0.8} \tag{1.7}$$

where P_{abl} is expressed in Pa, Φ in 10^{14} W.cm^{-2}. However, this maximum pressure is not enough to describe the pulse, and its temporal profile, which can only be perfected by modelling the laser-matter interaction [Gay 2011].

1.5.1.2 Irradiation in confined mode

The irradiation in a confined system consists of covering the affected area with a confinement medium, transparent to the wavelength of the radiation, which retains the volume expansion of the plasma. The duration and pressure of the impact are then increased respectively by a factor of 2-3 and 5-10 as compared to the direct regime [Fabbro 1990, and Berthe 1997]. The pressure P_{conf} generated by a confined plasma is estimated in GPa by the formula (1.8) assuming laser energy completely deposited at the interface [Fabbro 1990]

$$P_{conf} = 0.01.\sqrt{\frac{\alpha}{\alpha+3}}.\sqrt{\phi}.\sqrt{Z} \tag{1.8}$$

where α is the proportion of energy of plasma transformed into thermal energy in interaction, commonly retained at 0.25 [Berthe 1997], and Φ estimated in GW.cm^{-2}. The relative acoustic impedance Z, or reduced impedance, takes into account the difference in impedance between the confining areas and confined area. Z is expressed in g.cm^{-2}.s^{-1} by (1.9)

$$Z = 2.\frac{Z_{confinement}.Z_{target}}{Z_{confinement} + Z_{target}} \tag{1.9}$$

where the acoustic impedance is given by the relation $Z = \rho.C_0$; with ρ density of the material (g.cm^{-3}) and C_0 the hydrodynamic speed of sound in the medium (cm.s^{-1}) by (1.10),

$$C_0 = \sqrt{\frac{E.(1-\nu)}{\rho.(1+\nu).(1-2\nu)}} \tag{1.10}$$

where E is modulus of elasticity (Pa), ρ is density of the material (kg.m^{-3}), and ν is the Poisson's ratio. These shock waves tend to propagate faster than the speed of sound in the material, and this type of wave propagation is non-linear [Krehl 2008], whereas, the generation of stress waves by the light ablation phenomenon is linear. The mechanisms involving the propagation of laser induced stress waves in a composite target are illustrated in the next section.

1.5.2 Generation of laser induced stress waves

It is well understood that, as the incident energy increases, the temperature of the surface of the target increases, and at some point the material reaches its boiling point. At this boiling point, some of the material under the laser spot undergoes the phenomena of vaporization, ionization and formation of plasma is observed at the end [Scruby 1990]. It has been explained that, when using a non Q-switched normal pulse lower energy laser on a target, measuring the thermal conductivity into the bulk of the material is very important to control the amount of material that is vaporized [Ready 1971, and Scruby 1990]. However, with Q-switched lasers, much higher energy is obtainable and the heat transfer rate is very fast, for an appreciable conduction to occur. Thus, the amount of material that is vaporized under the laser spot depends entirely on the latent heat of vaporization of the material. Relation (1.11) posits an approximation of laser intensity/power density, Φ (W.cm^{-2}), above which thermal conductivity of the material can be neglected [Ready 1971]:

$$\phi \geq 2.L.\rho.K^{0.5}.\tau^{-0.5} \tag{1.11}$$

where τ the pulse duration (s), L the latent heat of vaporization of the solid (J.kg^{-1}), K the thermal diffusivity (m^2.s^{-1}), and ρ the density (kg.m^{-3}).

For the normal non Q-switched lasers, it can be assumed that the surface under the laser spot remains at the melting point, so that the material removal rate can be expressed by (1.12) [Ready 1971]:

$$\xi = \frac{\phi}{\rho.[L + C_v.(T_v - T_o)]} \tag{1.12}$$

where ζ the material removal rate (m.s^{-1}), Φ laser intensity/power density (W.cm^{-2}), ρ the density

($kg.m^{-3}$), L the latent heat of vaporization of the solid ($J.kg^{-1}$), C_v the specific heat capacity ($J.kg^{-1}.K^{-1}$) and T_v/T_o are the vaporization/initial temperature (K).

A net reactive force produced due to this ablation of the material from the surface, generates stress σ against the material. This can be calculated as the rate of change of momentum using Newton's second law of motion as in (1.13 and 1.14) [Scruby 1990].

$$\sigma = \frac{\phi.\xi}{L + C_v.(T_v - T_o)} \tag{1.13}$$

$$\sigma = \frac{\phi^2}{\rho.[L + C_v.(T_v - T_o)]^2} \tag{1.14}$$

This stress generated on the surface can help in estimating the magnitude of laser impact. In addition to that, this value can be helpful in the numerical simulation.

1.6 Optical detection of ultrasound

Optical detection of ultrasound is attractive because it is contactless, with a high bandwidth detection (unlike PZT transducers), and it can provide an absolute measure of the ultrasound signal. The optical detection sensitivity is at least an order of magnitude smaller than the contact based transducers, in particular on objects that scatter light in a diffusive manner [Krishnaswamy 2003]. Most of the recent works in laser ultrasound has been devoted to improving the optical detection sensitivity [Monchalin 1986, Wagner 1990, and Dewhurst 1999]. In this section, the initial description includes the methods in which the ultrasonic signal information can be encoded on a beam of light, followed by a discussion of some of the most common methods to demodulate the information encoded using optical interferometry.

1.6.1 Encoding information of ultrasound on an optical beam

To monitor ultrasound optically, a light beam must be made to interact with the object subjected to a motion/movement. Particular attention in this section will be limited to opaque solids that either reflect or scatter light. In this case, the light beam can be used to monitor the motion/movement of the surface associated with the ultrasound. The ultrasound can change the light beam property in multiple ways. These can be classified into intensity-modulated techniques and phase/frequency modulated techniques [Krishnaswamy 2003].

1.6.1.1 Intensity Modulation Techniques

The intensity of the reflected light beam may change, due to the ultrasound induced changes in the refractive index of the medium, and this can be detected with a photodetector. Although these changes are generally very small for most materials, this method has been successfully used in the picoseconds ultrasound [Grahn 1989], to measure the properties of thin films [Thompsen 1985], and nanostructures [Antonelli 2002]. Another technique based on the intensity-modulation uses the inclination of the surface associated with an ultrasonic motion [Adler 1967]. Here, the probing light beam is focused on an object surface of optical reflection. A partial opening is kept behind the lens, which is in the reflected beam path. This collimates the reflected beam, before being focused onto a photodetector. The reflected light beam will undergo a slight inclination due to the ultrasonic displacement, resulting in a change of intensity at the photodetector [Krishnaswamy 2003]. In general, intensity modulation techniques are less sensitive than phase/frequency modulated techniques, hence, limited application in NDE. Extensive review on intensity modulation techniques is presented in [Monchalin 1986, and Wagner 1990].

1.6.1.2 Modulation of phase or frequency induced by ultrasound

An ultrasonic motion on the surface of an object also affects the phase or frequency of the reflected or scattered light. For simplicity, consider a surface of an object illuminated at normal incidence with a light beam as shown in Figure 1.9. Let the normal surface displacement at the measuring point, due to the ultrasonic motion, be *u(t)*, where *t* is time. It is assumed that the inclination of the surface is not of high order that the reflected beam is inclined significantly. This results in the change of phase of light by changing the path length (equal to twice the normal ultrasonic displacement) [Krishnaswamy 2003].

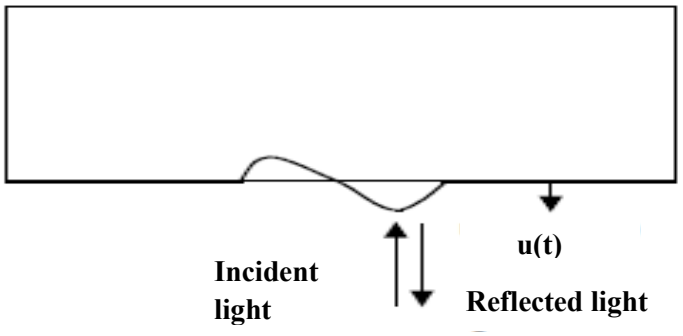

Figure 1.9: Illustration of Phase modulation of light due to ultrasonic displacement [Krishnaswamy 2003].

Since, an ultrasonic wave packet causes a time-varying phase modulation; it is also possible to view the optical interaction with the surface motion/movement as an instantaneous Doppler shift in optical frequency [Krishnaswamy 2003]. A Laser Doppler Vibrometer (LDV) operates on this principle, and this has widely been used for optical detection [Olsson 2009, Sun 2013, and Park 2014].

However, the phase information using a single optical beam cannot be measured directly, as the optical frequency is too high to be decoded by any existing photodetector. Therefore, a demodulation system has to be used to retrieve phase-encoded signal information [Krishnaswamy 2003], which will be discussed in the next section.

1.6.2 Optical interferometry

There are a number of optical interferometers available to perform the demodulation of phase-encoded signal. In this section, some of the more common systems that have found application in laser ultrasound detection are described. The interferometers can be broadly classified into reference beam interferometers and self-referential interferometers. In the reference beam interferometers, the optical signal beam from the object is mixed with a separate plane reference beam. As such, they work best on a polished mirror optical surface. The most popular configurations in this type of interferometers are (1) Homodyne interferometry and (2) Heterodyne interferometry. Self-referential interferometers offer significantly improved performance on relatively rough surfaces. The speckled object beam containing information about the displacement of the object is mixed with, a reference beam that is wave front matched, which may or may not possess any signal information. It is then possible to mix the two beams spatially to extract the signal of interest. Some of the popular self-referential interferometers are: (1) time-delay interferometer, (2) Fabry-Perot (FP) interferometer, (3) adaptive holographic interferometer [Malacara 1992, and Krishnaswamy 2003].

1.6.2.1 Two-beam homodyne interferometers

The simplest optical interferometer configuration is the two beam Michelson interferometer shown in Figure 1.10. The laser beam is split into two; one is projected on the test object, and the other is projected on a reference mirror. Post reflection, the two beams interfere at the photodetector.

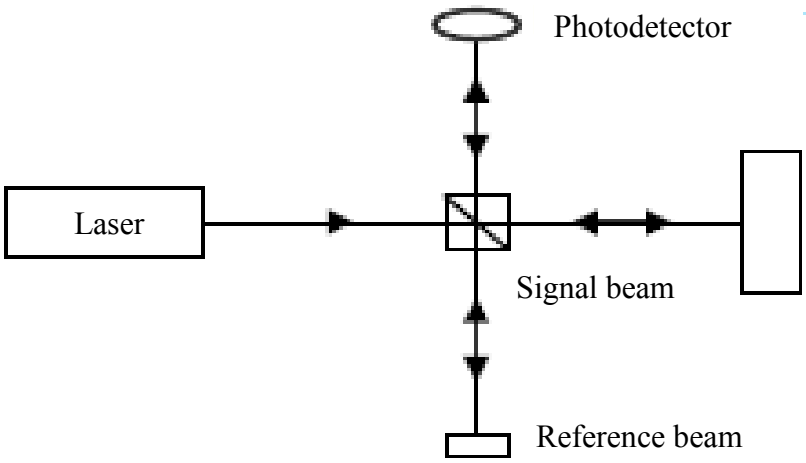

Figure 1.10: Setup of a two-beam homodyne interferometer (Michelson) [Krishnaswamy 2003].

However, the surface of the object needs to be reflective, for the successful measurement. The minimum detectable ultrasonic signal is dependent on the Signal to Noise Ratio (SNR $\geq$ 1). In an optical detection system, there are many possible noise sources such as the laser, photodetector, electronics, in addition to ambient noise in the optical path. With an increase in optical power, shot noise increases, and sets an absolute limit of detection for optical measurement systems [Krishnaswamy 2003].

1.6.2.2 Two-beam heterodyne interferometers

In comparison with the homodyne setup, the SNR of the heterodyne interferometer can be reduced to about a factor of half [Monchalin 1986]. Heterodyne, as the name implies, involves interference of light between two beams of different frequency. Typically, this frequency shift is obtained through an Acousto-Optic Modulator (AOM) as shown in Figure 1.11 [Krishnaswamy 2003]. The signal can be extracted either through the phase locked loops or using frequency discriminators. The former extraction technique provides a signal proportional to the surface displacement, and the latter provides a signal proportional to the surface velocity [Monchalin 1986].

Heterodyne interferometer provides an absolute measure of the ultrasonic signal. For example, at heterodyne frequency the ratio of the sideband amplitude to the carrier amplitude is directly proportional to the ultrasonic displacement in a spectrum analyser [Krishnaswamy 2003]. Furthermore, unlike homodyne interferometers, the heterodyne setup does not require active mechanical stabilization. Hence, the heterodyne interferometer is better suited for industrial applications [Monchalin 1993].

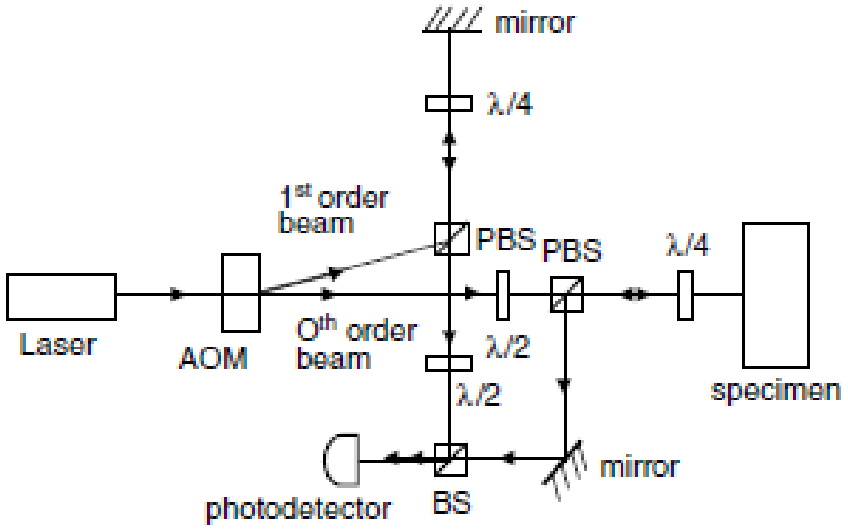

Figure 1.11: Setup of a two-beam heterodyne interferometer [Krishnaswamy 2003].

However, if the object diffusively scatters the light, the performance of the heterodyne interferometer degrades significantly, because the reflected beam cannot be recollimated into a plane wave. In addition, mixing of a non-planar object beam with a planar reference beam is inefficient [Krishnaswamy 2003].

1.6.2.3 Time-delay interferometer

Figure 1.12 shows the long-path time-delay interferometer. The scattered beam from the object is accumulated and split into two beams. Both the beams are reflected back by mirrors, but one beam travels via a short leg and the other travels via a long leg. The two beams are essentially wave front-matched, since both the beams that interfere arise from the scattered beam from the object surface; hence the spatial-mixing will be optimal. Nevertheless, one beam travels a distance longer than the other does. Hence, the frequency response of time-delay interferometers is not uniform. Time-delay interferometers are useful only for detecting fairly narrowband ultrasonic signals of known frequency range [Krishnaswamy 2003].

1.6.2.4 Fabry-Perot interferometer

In this interferometer, the light from the test object is assembled in a device that consists of two planar or confocal mirrors (curved mirrors facing each other with coincident focal point) that form a FP cavity also called as etalon. The mirrors are of very high reflectivity, such that the light goes through multiple reflections between the two mirrors and a part of the light exits from each end at

every reflection. Figure 1.13 shows a typical configuration of Fabry-Perot (FP) etalon interferometer.

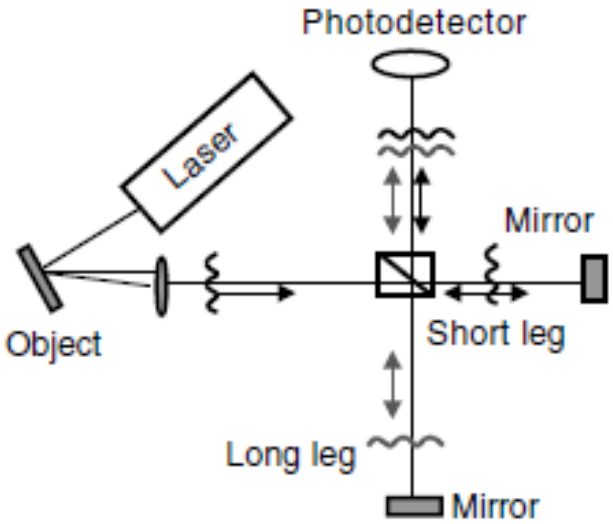

Figure 1.12: Setup of a long-path time-delay interferometer [Krishnaswamy 2003].

The FP interferometer is actually a very good instrument at moderate frequencies. However, the FP response varies inversely with respect to ultrasonic frequency, making its response at low frequencies very poor. In fact, the response is more complex, as multiple beams that interfere actually must have been incident on the object at different times, and therefore would possibly have sampled the ultrasonic wave packet at different times [Krishnaswamy 2003].

1.6.2.5 Dynamic holographic interferometer

This type of interferometer is based on dynamic holographic recording, usually in a photorefractive media such as a Photo-Refractive Crystal (PRC). The speckled object beam can be planarized in one approach using an optical phase conjugation [Paul 1987, and Delaye 1995 a]. This planarized object beam can be effectively mixed with a planar reference beam in a two-beam homodyne or heterodyne interferometer [Krishnaswamy 2003].

As another approach, a reference beam with the same speckle structure as the static object beam can be holographically reconstructed for an interference with the object beam that contains the ultrasonic information [Ing 1991, Delaye 1995 b, and Pouet 1996]. This can be achieved by using the process of two-wave mixing in photorefractive media [Malacara 2007].

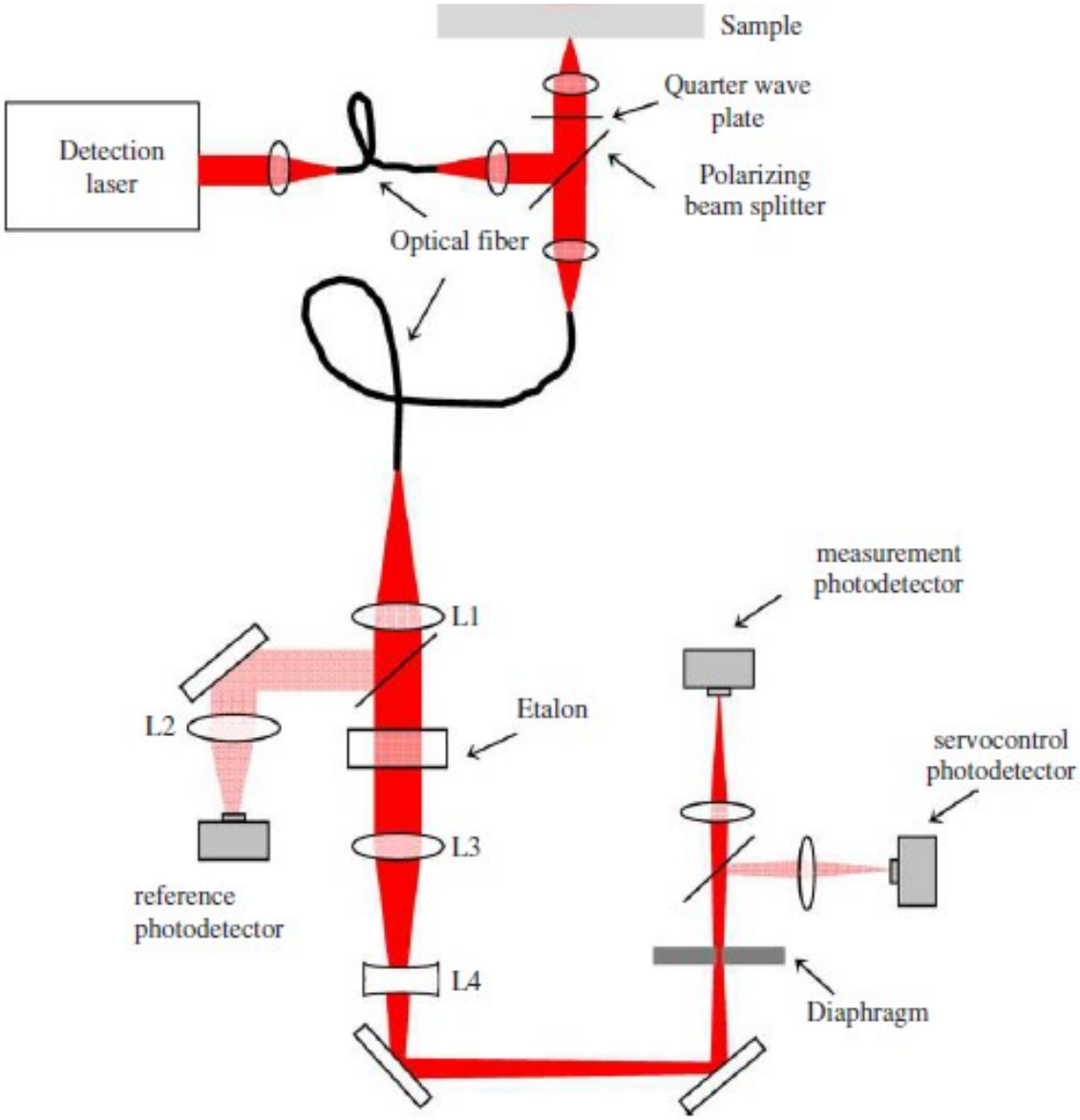

Figure 1.13: Optical layout of the Fabry-Perot etalon interferometer setup [Arrigoni 2008 b]; L1, L2, L3, and L4: the lenses; Etalon: two reflecting plates/mirrors for producing interfering light beams;

Two-wave mixing is a dynamic holographic process where two coherent optical beams (pump/reference and probe/signal beams) mix and interact within a PRC. As a consequence of this, not only a portion of the transmitted probe beam will be available at the exit of the PRC, but also a part of the pump beam that is diffracted into the direction of the probe beam will be available. The diffracted pump beam into the path of the signal beam will possess the same wave front structure as the transmitted signal beam [Krishnaswamy 2003]. Figure 1.14 shows an isotropic diffraction configuration.

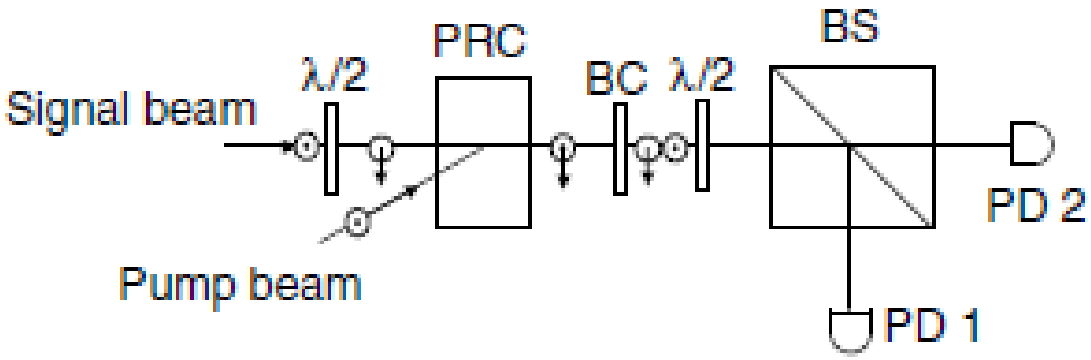

Figure 1.14: Setup of an isotropic diffraction. λ/2: Half-wave plate; PRC: Photo-Refractive crystal; BC: Berek Compensator; BS: Beam Splitter; PD: Photo-Detector [Delaye 1997].

Since a certain response time is associated with the PRC process (dependant on: the material, the applied electric field, and the total incident optical intensity), it cannot adapt to sufficiently high-frequency modulations in the signal beam, and can only adapt to changes in the incident beams that are slower than the response time [Krishnaswamy 2003].

As a summary, study of the laser generation of ultrasound in numerous settings and on a variety of materials was carried out. To ensure the robustness of the technology, an extensive study of some of the popular laser optical systems to detect the ultrasound was also carried out with respect to their advantages and disadvantages. The effective detection system for industrial applications that can be used on wide range of materials and environments would further be discussed in Chapter 3.

1.7 Problem identification and motivation

With the comprehensive study of the laser induced stress wave propagation and its application towards the NDE, the applicability of a high repetition rate and low energy laser for this application needs to be studied. Because, in many of the research works illustrated in the previous sections, high energy and low repetition rate lasers have been used. These lasers are very expensive in comparison with the high repetition rate and low energy lasers. In addition, in the Laser Metrology and Micromachining Laboratory (LMML) of Concordia University, significant amount of research is being performed in the field of peening using a high repetition rate and low energy laser. Hence, using the same theory, a new area such as a NDE is spurred for an elaborate research.

1.8 Objectives and scope of the current work

Primary goal of this thesis is to study the feasibility of using a high repetition rate and low energy laser for laser ultrasound NDE. A study that follows the principle of stress wave propagation and takes into account the ToF of stress waves, to carry out the NDE. To accomplish the objective, the scope of this research work would include –

a. Building a numerical model that posits the results based on the laser-matter interaction, followed by validating the model with experimental and numerical studies from literature for isotropic materials.
b. Validate the numerical model for multi-layered composites, by taking into account the important factors from the literature.
c. Conducting a feasibility study for a high repetition rate and low energy laser, and understanding its applicability for the NDE of structures, such that the technology can be affordable.
d. Extending the numerical study to understand the change(s) in ToF, to quantify the presence and depth of a delamination using the same composite model, for the loading parameters of a high repetition rate and low energy laser.
e. Carrying out the experiments on carbon/epoxy composite laminates, and deriving a correlation between the numerical and experimental study concerning the behaviour of laminated composites subjected to a laser impact.

Some of the scientific challenges:

- The generation and propagation of stress waves in layered materials.
- The dynamic response of composite and their assemblies to a laser impact.
- The study of the effects of impedance mismatch of the materials and interfaces.
- The effects of the process on the simulation parameters based on material properties.

This thesis is completed under the collaboration between Laser Metrology and Micromachining Laboratory (LMML), Concordia University, Montreal, Quebec and Tecnar Automation Ltée., Saint-Bruno-de-Montarville, Quebec.

1.9 Thesis organization

This thesis consists of five chapters. The first chapter has some theoretical concepts with respect to the generation and detection of ultrasound for pointing out to the objectives. The following chapters deal with modelling, then the experimental support of response of composite laminates to laser impact, and finally the analysis of investigations conducted.

- The first chapter is devoted to the flaws and their effects in the representative carbon/epoxy composite laminate for the aerospace application. The existing flaw detection methods are briefly described and the problems that persist are depicted. The potential of laser ultrasound NDE to overcome the problems with the existing methods to detect the flaws has been explained with theoretical and phenomenological backing of the laser impact. An introduction to the optical ultrasound detection systems is also given.
- The second chapter deals with the numerical study of the stress wave propagation in different materials. A re-work of simulation of selected publications will be carried out to validate the model for both metals and composites. Validation of numerical models will be carried out such that, the model is capable of positing the results relative to the ultrasound generation and detection. Multiple models will be compared to know the optimal design of the numerical model. Within the same composite model, delamination at different interplies will be introduced to attain the results and analyse the changes. This study should enable NDE to be performed successfully in the industrial contexts. The material parameters that have a significant effect on the change of model's behaviour will be noted. The simulation would also be carried out for the high repetition rate and low energy laser parameters, and changes in the results will be observed. Lastly, the numerical model will be redesigned in order to reduce the computation time, and the results will be compared.
- The third chapter details the manufacturing of the composites with respect to the lay-up, orientation, curing cycle, and introduction of delamination. The layout of experiments and other details of experimental set-up will be described. Finally, experimental results for the laminates with and without delamination will be presented. The experiments will also be conducted on a laminate with reduced thickness, and the changes in the results will be observed. Lastly, the effect of misalignment, in the ultrasound generation and detection beams, on the results will be investigated.

- The fourth chapter discusses the comparison and analysis of numerical and experimental results. A correlation will be derived in the experimental results with respect to the numerical study in characterising the delamination. Important material properties, concerning the propagation of stress waves, will be highlighted. Numerical study of using different inclusion metals to create a delamination like feature in laminates for the sake of experimental study, will conclude the chapter.
- The fifth and the last chapter gives a rundown of the understandings and observations at every stage of the research. Some of the possible future modifications that can be incorporated into the laser ultrasound NDE of materials will be briefly narrated.

1.10 Summary

In this chapter, a study is carried out on composites and the flaws. A brief elaboration of their adverse effects are asserted and several NDE techniques were reviewed. Laser generation and detection of ultrasound to carry out NDE of materials has the potential to overcome the problems that persist in the current technologies. A brief introduction of some of the popular optical detection systems hypothesizing their capabilities and some associated problems are posited. Problem identification and thesis motivation is clearly presented, so that the objectives and scope of the work is framed.

Having properly understood the generation of ultrasound and detection systems using lasers, next chapter would bring out the clarity of how the laser and material parameters effect the stress wave propagation using numerical simulation.

CHAPTER 2. Numerical study of stress wave propagation

2.1 Introduction

In this chapter, the mechanism of stress wave propagation in composite laminates, induced by laser, is initially discussed. With this understanding, the numerical model will be built based on the assumptions considered. Having surmised the modelling assumptions, a parametric study will be conducted, first on metals to validate the numerical model, and then on composites. The associated problems in the modelling will be explained. These problems may necessitate developing a model with better efficiency and accuracy, to study the stress wave propagation in multi-layered composites numerically.

With an efficient numerical model, comparative study will be carried out based on the variation of different material and laser parameters. The simulation settings will be adjusted based on the test set-up of conventional NDE techniques. In addition, this study would be extended to record the changes in results based on the depth of a delamination. To ensure a better computational efficiency, the numerical model will be further rebuilt, and the variation in the results will be noted.

2.2 Propagation of a laser induced stress wave

This section describes the mechanical stress waves in the case of the mono-dimensional plane, and passage of an interface in a composite laminate. During the passage of an interface, the incident wave from the upstream medium referenced 'A' is transmitted as a wave of the same nature in the downstream medium B which is in contact. The stress wave is simultaneously reflected in the medium A, and transmitted in the medium B, as a wave of relaxation or shock/stress respectively, depending on the nature of the incident wave and the adjacent material impedance ratio:

- If $Z_A < Z_B$, the reflected wave is of the same nature as the incident wave, and hydrodynamic pressure of the shock/stress transmitted is amplified.
- If $Z_A > Z_B$, the reflected wave is likely opposite to the incident wave, and the hydrodynamic pressure of the shock/stress is reduced.
- If $Z_A = Z_B$, the incident wave does not see the interface and continues to propagate.

These properties portray the mechanical continuity between the two media, in the case of impact in the mono-dimensional front: pressure, $P_A = P_B$; and displacement, $u_A = u_B$;

Figure 2.1 summarizes the four interface passage configurations depending on the material impedance ratio and the nature of the incident wave between the ply and the interply. The illustration explains the passage of a homogenized interply/ply interface (figure 2.1-a) and conversely (figure 2.1-b), with $Z_{ply} > Z_{interply}$.

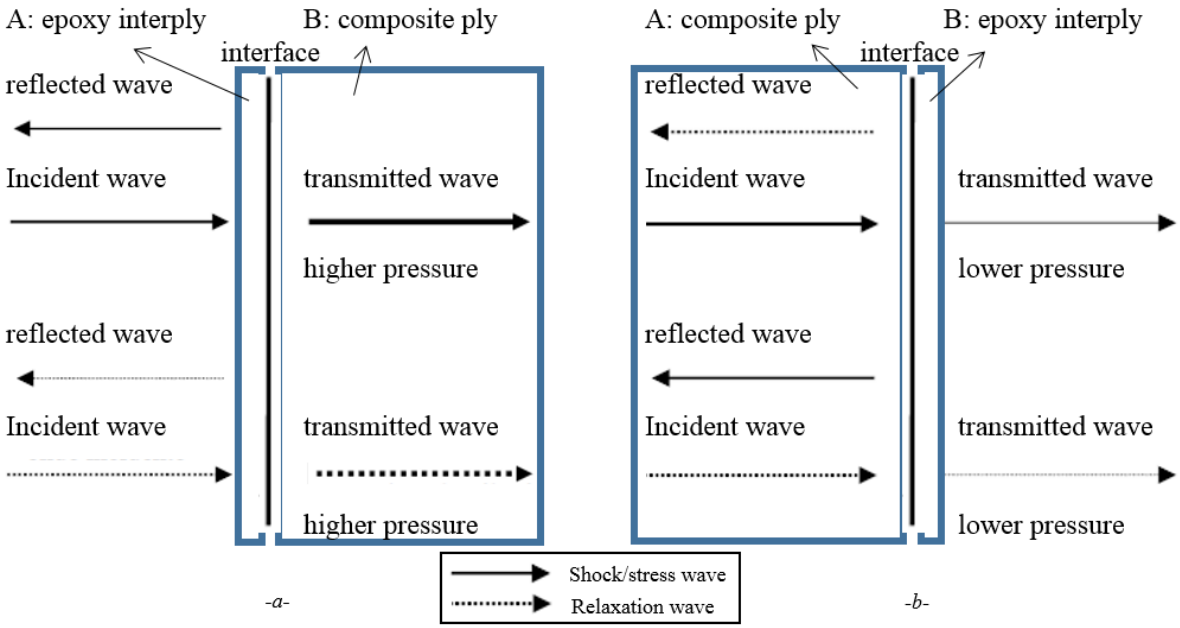

Figure 2.1: Nature of the transmitted and reflected waves at the passage of an interface according to the impedance ratio: -a- $Z_A < Z_B$: example of interply/ply interface, and -b- $Z_A > Z_B$: example of ply/interply interface (Picture not to scale).

2.3 Modelling of laser impact

The numerical simulation is an essential step in the characterization of, loading and dynamic behavior of the target. Interpretation of the results and quantification of stress levels requires control of the propagation of stress waves in the material, on which computer simulation is based. The model predicts the response of materials to a known load. The corollary of simulation leads to parameterizing the impact characteristics on the sample's morphology. The goal is to have options of models that support the experiments and as well to use as a tool to predict the behaviour. Figure 2.2 illustrates the approach of simulation, the calculations of laser-matter interaction and propagation of waves that are being decoupled. The modeling process is organized as follows:

The pressure amplitude is evaluated by the equations (1.6), (1.7) and (1.8) for a shock loading and for the stress generated on the surface by the laser by (1.14) or adjusted by the correspondence of the amplitude of the free surface velocity calculated with its experimental value. The equations can only approximate to a value of stress generated that ignores specific losses of energy by radiative transfer, and any changes in phase [Scruby 1990, and Bolis 2007]. The spatial pattern is given by (1.5), and this would be in accordance with the imprint left by irradiation on a photosensitive paper. These parameters, adjusted by reverse approach characterizes the loading, and concludes the numerical study of laser-matter interaction.

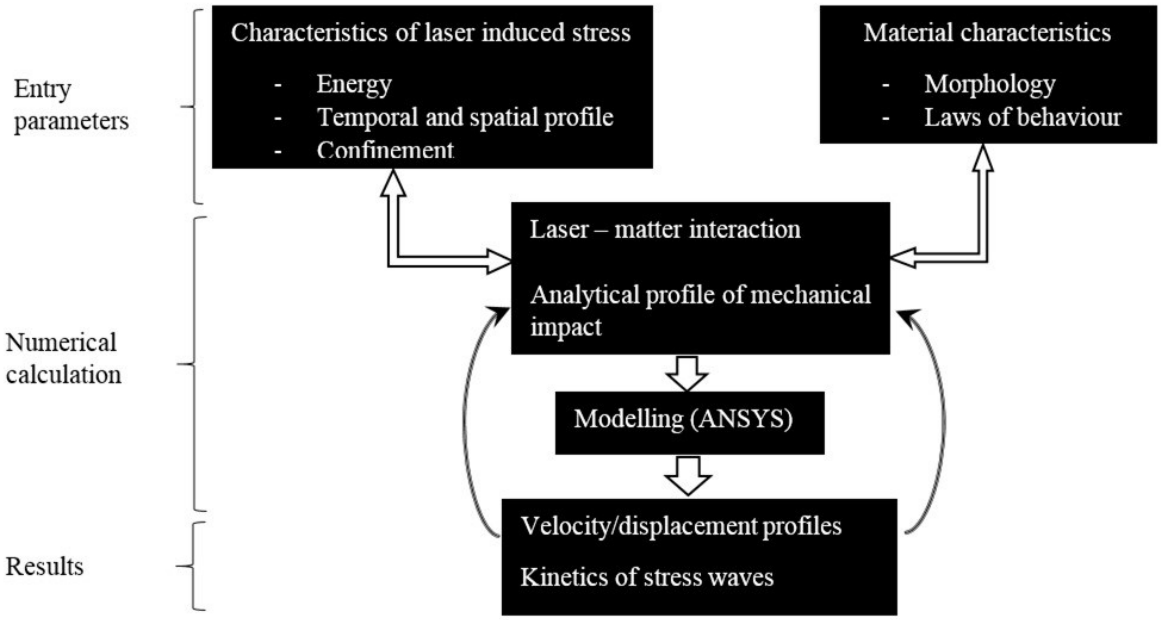

Figure 2.2: Schematic of the protocol of modelling of the laser impact and validation by inverse approach parameters [Gay 2011].

The materials are then modelled following their geometry (thicknesses of the layers), and parameterized according to the laws governing their dynamic behaviour. The load is applied to the model and the computation is launched following the settings described in section 2.3.2. The last stage of the modelling is to perform a parameter study of the characteristics of materials, and numerical models in order to observe their influence with respect to the laser impact on the target. The major challenge of modeling this phenomenon is the proper understanding of loading parameters and the target, to get accurate velocity/displacement profiles.

2.3.1 Framework of the simulation

2.3.1.1 Laser-matter interaction

Laser-matter interaction calculation involves the conversion of energy into an equivalent pressure profile. The input parameters have the description of characteristics of the laser pulse, namely, wavelength, temporal profile and energy. The profile of pressure is validated by inverse approach.

2.3.1.2 Parameters of the calculation

The formulation of the calculation is explicit, where the quantities are expressed in terms of their value at the previous time step, to assess real-time convergence calculations. This resolution method is used with caution, because the result depends greatly on the time step and the mesh size. The generated mesh is composed of quadrilateral structured elements, and the axial parameter Δl, is estimated by the equation (2.1) for the convergence of the calculation [Gay 2011, and Gay 2014 b].

$$\Delta l \leq \frac{C_0.\tau}{6} \tag{2.1}$$

The lattice parameter is of the order of μm, the wave is hence contained in more meshes during its propagation. The mesh is however less dense outside the propagation area of interest of one-dimensional waves, to reduce the computation time. The time step Δt between each iteration is adjusted according to the mesh by the differential equation of Courant-Friedrich-Levy (2.2) for the convergence assurance of computing [Gay 2011 and Gay 2014 b]. Therefore, the propagation then does not cross over the mesh between the two time increments.

$$\Delta t \leq \frac{\Delta l}{C_0} \tag{2.2}$$

2.3.2 Parameters of the numerical model and assumptions

The material is modelled according to its morphology, laws of behavior, and mechanical properties. Irradiation of the target is simulated by the pressure equivalent to the impact on the incident surface. The impact is considered mono-dimensional for composites, and the time profile is approximately predicted from the energy profile of the pulse during the experiments. The parameters of the pulse are adjusted by adequacy of numerical and experimental results on elemental targets.

Once the stress waves are generated, measurable broadband nature prompts the waves to disperse widely within the model. The mono- or bi-dimensional character of the propagation of waves is taken into account depending on the end supports used. The conditions applied to limits of the model are:

- All the degrees of freedom of the nodes of axis of symmetry/boundary are fixed, with the exception of simple displacement following the axis of the laser. This property is not applicable to the anisotropic materials, because the constraints no longer have axially symmetric distribution, and require 3D model or modelling of a cross-section at least.
- A quadrilateral mesh, following the relation (2.1), is generated throughout the sample, to prevent hourglass effect of the mesh elements, which could disrupt the evolution of waves.

2.4 Parametric study by numerical simulation

This section describes the modeling of composites subjected to a brief impact load that follows the procedure and the conditions described in section 2.3:

- The setting of the load (pressure amplitude, temporal and spatial profile) is taken from literature to validate the numerical model, for the simulation of stress wave propagation using transient structural module in ANSYS that solves the equation of motion given by (2.3),

$$[M]\{\ddot{x}\}+[C]\{\dot{x}\}+[K]\{x\}=\{F(t)\} \tag{2.3}$$

  where *[M]* is the mass matrix, *{ẍ}* is the acceleration vector, *[C]* is the damping matrix, *{ẋ}* is the velocity vector, *[K]* is the stiffness matrix, *{x}* is the displacement vector, and *{F(t)}* is the load vector.

- The material parameters and validation of the numerical models are established from the references [Berthe 1997, Gay 2011] and from detailed review of the laser ultrasound technique.
- The initial conditions of the model, as illustrated in the work of [Gay 2011] of axial symmetry/mono-dimensional cross-section, applied to the loading and the target, is maintained during the pressure propagation phase within the materials and isotropic stacks.

2.4.1 Validation of numerical model using metals as target

The purpose of modeling is to replicate as closely as possible the propagation of stress waves in the material. The laser shock/stress wave propagation was studied on aluminium by D. Devaux

[Devaux 1993], and Laurent Berthe [Berthe 1997]. It is hence reasonable to simulate one of the works as first part of the numerical study of this thesis. For that reason, a simulation of an aluminium target - subjected to laser impact - was carried out to validate the 3D numerical model with respect to the mesh sizing and the iteration time steps, such that the results closely match the experiments. In addition, this study is useful to understand the influencing factors in the numerical modelling that affect the results when a comparative analysis is performed with the experimental data. Table 2.1 describes the simulation parameters adjusted with respect to the laser parameters set by Laurent Berthe [Berthe 1997].

Young's Modulus: E (Pa)	71000000000
Density of Al.: ρ ($kg.m^{-3}$)	2770
Poisson's Ratio: ν	0.33
Speed of Sound Wave: C_0 ($m.s^{-1}$)	6162.563569
Element Size: Δl (mm)	0.025
Time Step: Δt (s)	$4.167.10^{-9}$

Table 2.1: Parameters selected for computer simulation for a laser of intensity of 2 GW/cm².

The pressure profile used in the simulation software can be seen in Figure 2.3. The pressure magnitude is calculated using equation (1.8) and the laser parameters mentioned in Table 2.2. The pulse duration is used to fit the rise of the laser pulse and its decay. For simplicity of simulation, the exponential decay of the pressure pulse has been ignored in this work.

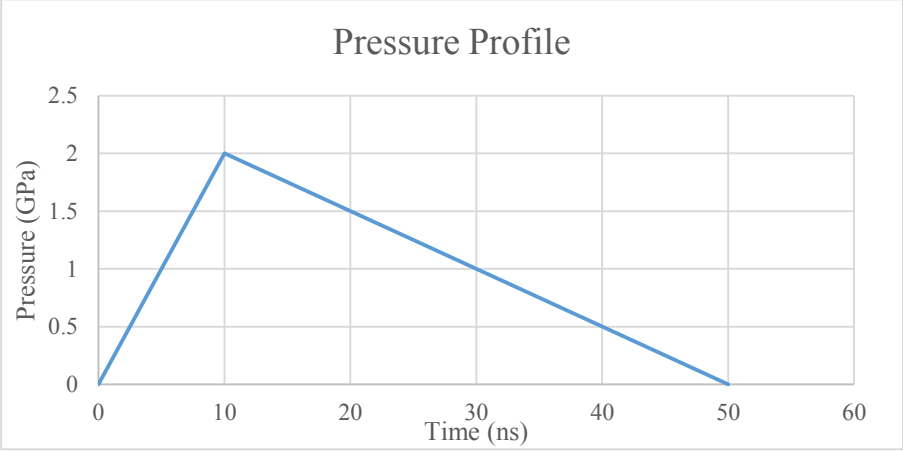

Figure 2.3: Laser induced pressure profile following the confined mode of generation with water as confining medium at an intensity of 2 GW/cm².

Impact Spot: d (cm)	0.3
Pulse Duration: τ (s)	0.000000025
Energy: e (J)	3.53
Intensity: Φ ($GW.cm^{-2}$)	2
Dimensions of Target (mm)	6 X 6 X 0.457
Speed of Sound Wave: C_0 ($cm.s^{-1}$)	642000
Density of Al.: ρ ($g.cm^{-3}$)	2.7
Impedance of Al.: Z_2 ($g.cm^{-2}.s^{-1}$)	1733400
Impedance of Water: Z_1 ($g.cm^{-2}.s^{-1}$)	149400
Total Impedance: Z ($g.cm^{-2}.s^{-1}$)	275090.25
α for Al.	0.25
Shock Pressure P (GPa)	2.05

Table 2.2: Laser and other relevant parameters to predict the pressure induced by laser.

Figure 2.4 shows the computed free surface velocities. Table 2.3 compares this simulation work with the measured experimental free surface velocity from Laurent Berthe [Berthe 1997]. The comparison will be performed for the first peak; this is sufficient to for NDE as elaborated in section 2.5.

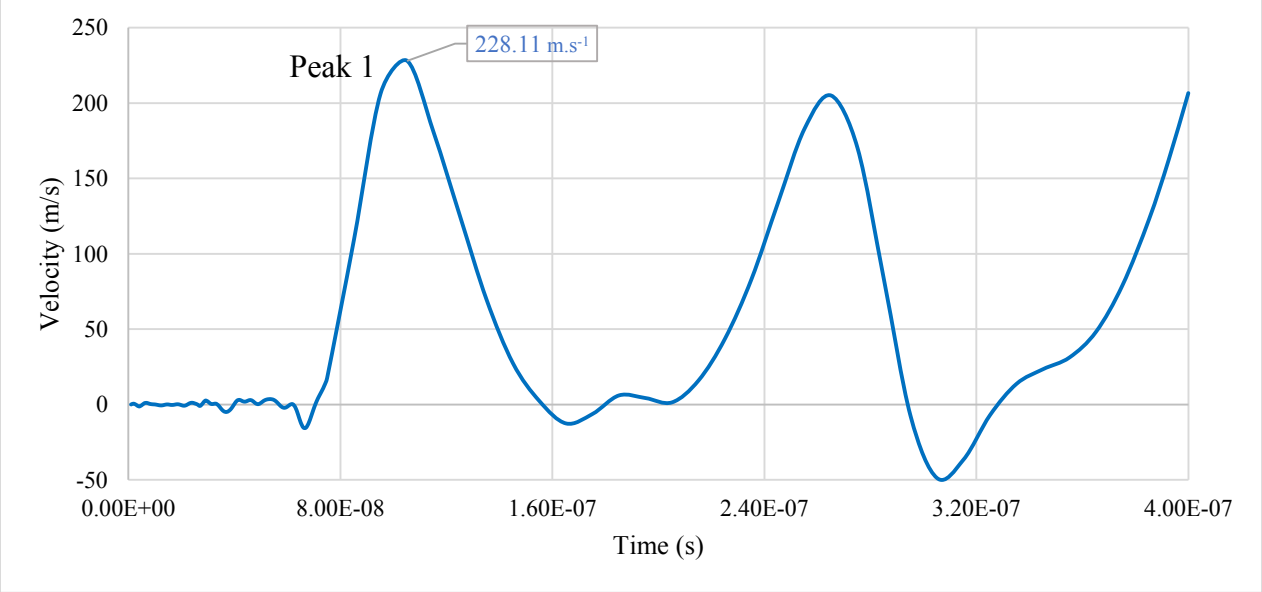

Figure 2.4: Free surface velocity of an aluminium target calculated using ANSYS to validate the numerical model.

	Peak 1		
	Simulation (Figure 2.4)	Experiments [Berthe 1997]	% change
Time evolution	105 ns	100 ns	4.76
Velocity magnitude	228 $m.s^{-1}$	225 $m.s^{-1}$	1.31

Table 2.3: Comparison of values between the simulation work in ANSYS and the experimental work of Laurent Berthe.

Similarly, back free surface velocity of a copper target coated with nickel under water confinement was computed using the parameters set by C. Bolis [Bolis 2007]. Table 2.4 describes the material parameters and Table 2.5 gives the simulation parameters calculated using equation (1.10), followed by equations (2.1) and (2.2). Figure 2.5 shows the calculated back free surface velocity of copper coated with nickel on the back surface, and Table 2.6 compares the simulation result for first peak with the work of C. Bolis [Bolis 2007].

Impact spot: d (cm)	0.1
Pulse duration: τ (s)	10.10^{-9}
Energy: e (J)	0.08
Intensity: Φ ($GW.cm^{-2}$)	1.02
Density: Cu ($g.cm^{3}$)	8.93
Density: Ni ($g.cm^{-3}$)	8.2
Sound wave speed of Cu.: C_0 ($cm.s^{-1}$)	393300
Sound wave speed of Ni.: C_0 ($cm.s^{-1}$)	411900
Impedance: Cu ($g.cm^{-2}.s^{-1}$)	3512169
Impedance: Water ($g.cm^{-}2.s^{-1}$)	149400
Total Impedance ($g.cm^{-}2.s^{-1}$)	286608.31
α for Cu.	0.25
Pressure (GPa)	1.5

Table 2.4: Material information and calculation of laser impact pressure with respect to laser specifications.

Material	Copper	Nickel
Speed of sound wave: C_0 ($m.s^{-1}$)	3933	4119
Thickness: t (μm)	119	88
Element Size: Δl (mm)	0.00671	
Time Step: Δt (s)	$1.67.10^{-9}$	

Table 2.5: Simulation parameters to calculate the back free surface velocity in accordance with the parameters tabulated in Table 2.3.

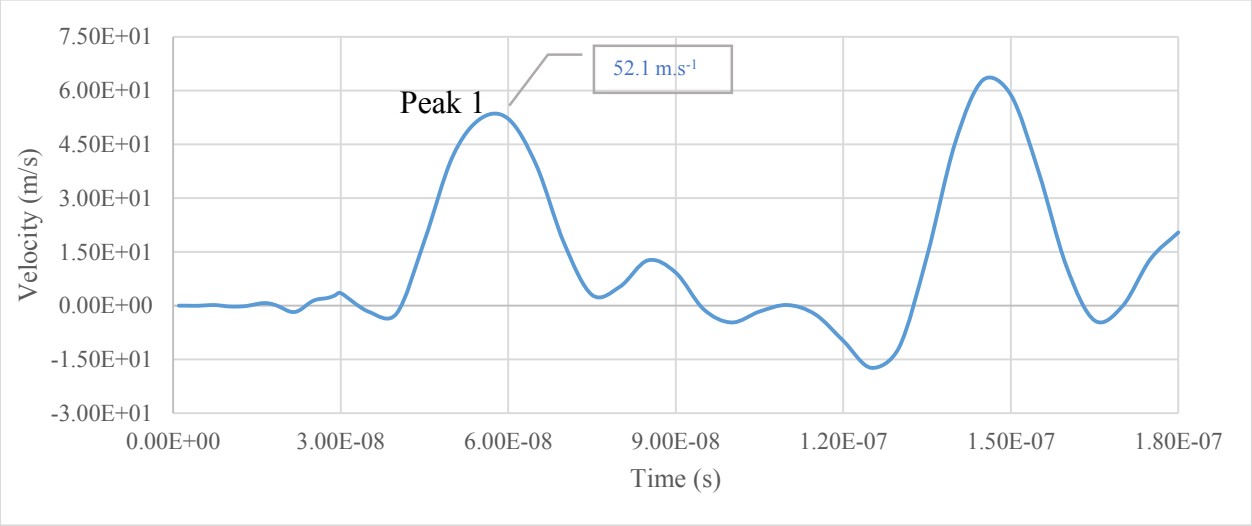

Figure 2.5: Calculated back free surface velocity of copper coated with nickel on its back surface.

The variation in the magnitude of velocity between the simulation carried out for this thesis, and the published experimental work is attributable to the longer time increments. The required time increment calculated is 1.67 ns and is mentioned in Table 2.5. However, to reduce computation time this value was set at 5 ns. This longer time increment has skipped the recording of behaviour of the model while computing.

	Peak 1		
	Simulation (Figure 2.5)	Experiments [Bolis 2007]	% change
Time evolution	60 ns	65 ns	7.69
Velocity magnitude	53 $m.s^{-1}$	63 $m.s^{-1}$	15.87

Table 2.6: Comparison of values between the simulation work in ANSYS and the experimental work of Laurent Berthe.

Although the time evolution of the stress waves closely matched with the results published by Laurent Berthe [Berthe 1997] (Table 2.3) and C. Bolis [Bolis 2007] (Table 2.6), but the computation time for a 3D model was very high depending on the geometrical dimensions of the model and computing capacity. In addition, the free space in the hard disk drive required is over 500 GB for this model to compute. Hence, the approach of simulating the mono – dimensional wave propagation on a 2D model to predict the free surface velocity was adapted [Gay 2011]. This in turn reduces the computation time, as the number of nodes are significantly reduced when moving from 3D to 2D, and requires significantly less free space in the hard disk drive.

Figure 2.6 presents the calculated results of free surface velocity using both 3D and 2D models for the case of aluminium. It can be noticed that the time evolution and the magnitudes of the velocity are identical when the results of 2D model are compared with the results of 3D model from Figure 2.6. Table 2.7 compares the magnitudes of velocities and time evolutions for the first peak or first shock/stress wave arrival between 3D numerical model and 2D numerical model with the experimental results published by Laurent Berthe.

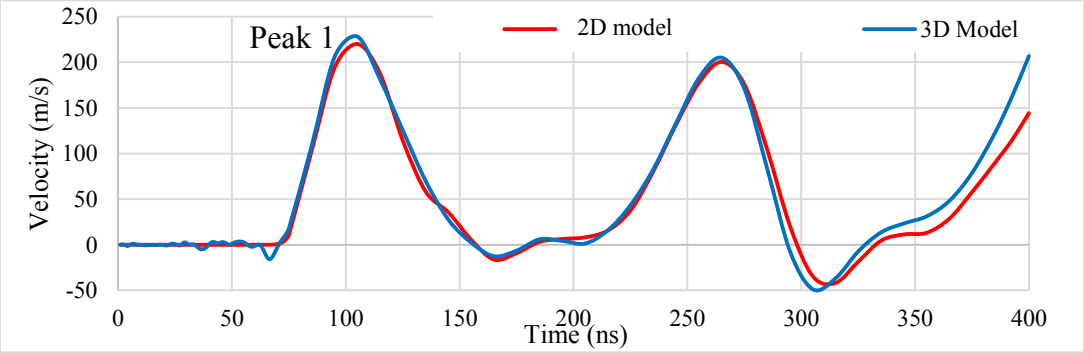

Figure 2.6: Comparison of back free Surface velocities of a representative aluminium mathematical model in both 3D and 2D configurations.

Peak 1	3D model	2D model	% change between 3D and 2D	Experiments [Berthe 1997]	% change between 2D and experiments
Time evolution	105 ns	105 ns	0	100 ns	4.76
Velocity magnitude	228 $m.s^{-1}$	223	3.07	225 $m.s^{-1}$	0.89

Table 2.7: Comparison of values between the 3D and 2D numerical models in ANSYS with the experimental work of Laurent Berthe.

With the 2D model, not only the time of computation can be reduced but also results that are more accurate can be attained, with comparably higher refinement in meshing by shortening the element sizes and with shorter time increments. It can be noticed in Table 2.7, where the % change between the 2D model and the experimental result is lesser than the % change between 3D model and experimental results. Hence, for carrying out the simulation of laser induced stress wave propagation in multi-layered CFRP composites, the 2D model will be adapted.

2.4.2 Validation of CFRP composite model

Numerical models of stress wave propagation in the thickness of laminate composite panels have been developed for an application to understand the case of an impact on plate for the strain rate recording of about 103 s^{-1} [Abrate 1998, and Parga-Landa 1999]. The materials are represented by a stack of layers of uniform thickness and different properties, by taking into account the anisotropy of the ply. The model is represented by alternative plies and interplies. The hypothesis of representation consists of the assumptions concerning the geometry, homogeneity and material behavior:

- The thickness of the plies is considered uniform in the plane of the plate.
- The strata are homogeneous and the local microstructure does not come into consideration.

The properties used in the composite numerical model validation for homogenised carbon/epoxy ply and for the epoxy interply can be found in Table 2.8 as used by Elise Gay [Gay 2011] in accordance with the 3D geometry shown in Figure 2.7 followed by the description of the thicknesses of all the plies and interplies in Figure 2.24.

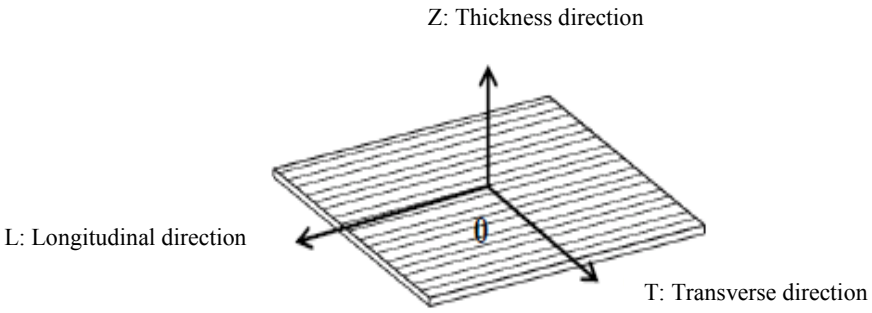

Figure 2.7: Notation system of axes of the unidirectional composite ply.

	ρ ($kg.m^{-3}$)	E (GPa)	ν	G (GPa)	C_0 ($m.s^{-1}$)	Z ($g.cm^{-2}.s^{-1}$)
CFRP Ply	1630	$E_T = 12.6$ $E_L = 201$	$\nu_{LT} = 0.3$ $\nu_{TZ} = 0.27$	$G_{LT} = 4.9$ $G_{TZ} = 4.5$	$C_{0T} = 3000$ $C_{0L} = 8100$	$0.49.10^6$
Epoxy Interply	1260	5.2	0.35	1.6	2600	$0.33.10^6$

Table 2.8: Dynamic properties of homogenized composite plies and epoxy resin interplies [Gay 2011].

For this validation, two numerical models were considered to simulate the stress wave propagation in a composite laminate within the 2D environment. The first numerical model, described in section 2.4.2.1, adapts 2D axisymmetric geometry as used by Elise Gay [Gay 2011]. The second numerical model computes the mono-dimensional waves with an emphasis on propagation by considering the cross-section of the laminate. This will be discussed in section 2.4.2.2.

2.4.2.1 Simulation of 2D axisymmetric composite model

When the sample has equal length and width for an arbitrary thickness, this type of 2D modelling can be utilized to reduce the computation time. In addition, the behaviour of the solid in a 3D perspective can be approximately estimated. Figure 2.8-a shows the boundary conditions of the model, and Figure 2.8-b shows the model with biased meshing, wherein the refinement is coarse in the region away from the impact region.

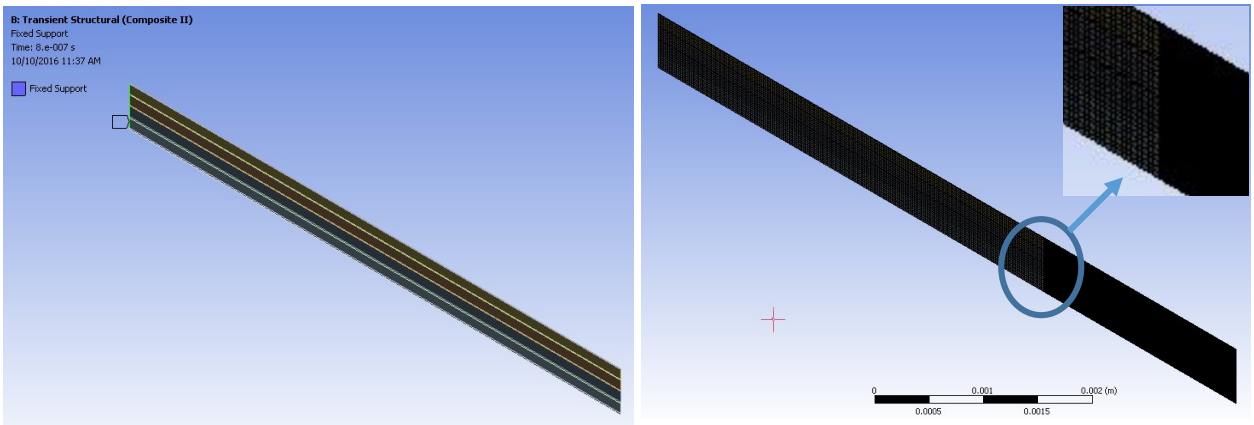

-a- *-b-*

Figure 2.8: 2D axisymmetric model of CFRP composite laminate; -a- the boundary conditions, and -b- the biased meshing wherein the zone of propagation is highly refined and the geometry away from the propagation zone has relatively less refined (2/3 to 1/3) meshing.

From the 3D perspective of the 2D axisymmetric model shown in Figure 2.9, it can be observed that, the energy is predominantly dissipated close to the region of laser impact.

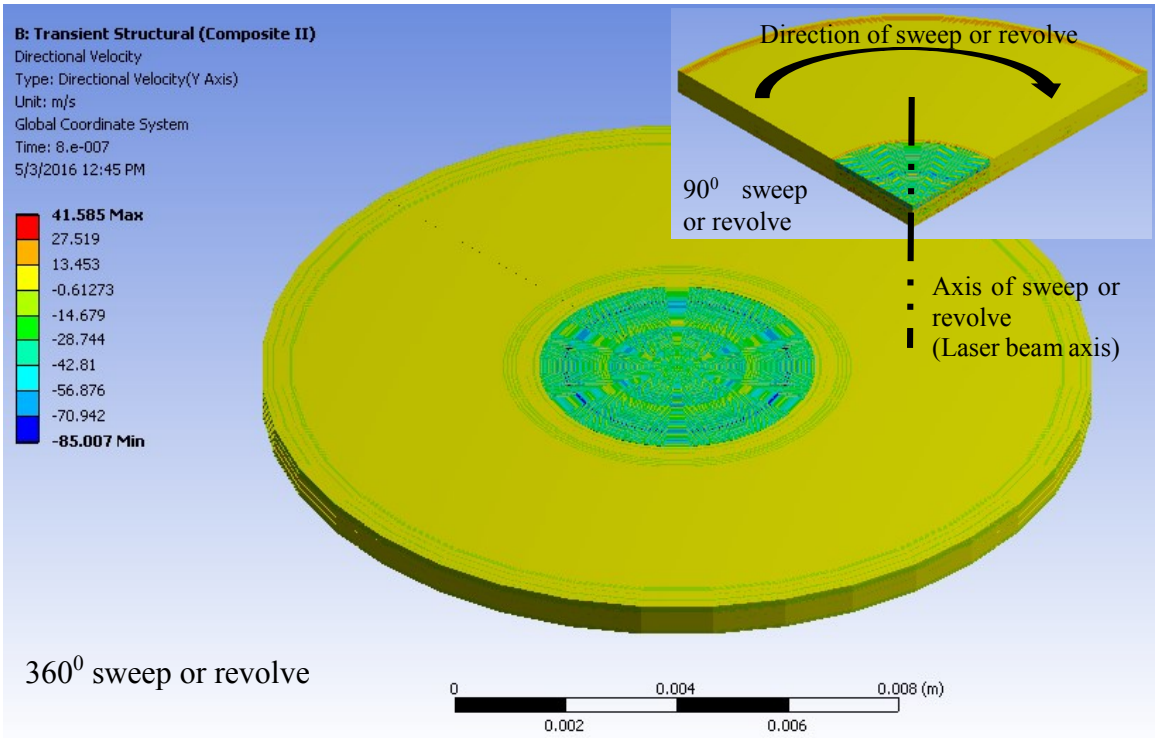

Figure 2.9: The three dimensional (3D) perspective of the 2D axisymmetric model with a 360^0 revolve and 90^0 revolve is presented in the inset.

2.4.2.2 Simulation of 2D cross-sectional composite model

To execute the simulation wherein the behaviour of stress waves around a delamination is properly assessed, 2D axisymmetric model is ineffective as the results are extrapolated with this model. It is hence necessary to build a numerical model, which must not only yield the correct results, but also provide a window of assessment within the laminate for a mono-dimensional stress wave(s). This is needed to understand, the total/partial reflection of wave(s) due to a discontinuity. The modelling of the cross-section of the laminate can be beneficial for this assessment. Figure 2.10 shows the cross-sectional numerical model of the composite laminate.

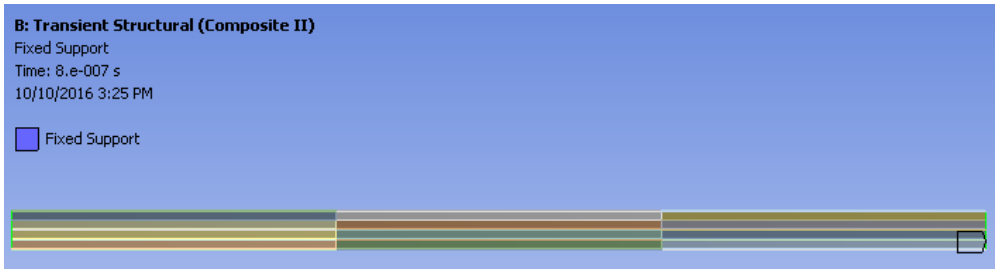

Figure 2.10: 2D cross-sectional numerical model of CFRP composite (15 mm X 0.605 mm).

The factors such as, the biased meshing, and boundary conditions were retained from the previous model. It can be seen in the Figure 2.10, a partition has been created to generate the biased meshing.

2.4.2.3 Simulation parameters and comparison of results

With the description of two numerical models in the 2D environment in the previous sections, the results of those are presented in this section. The pressure profile used in ANSYS for the laser parameters mentioned in Table 2.9, is given by Figure 2.11.

Impact Spot: d (cm)	0.25
Pulse Duration: τ (s)	$9.3.10^{-9}$
Energy: e (J)	0.41
Intensity: φ (GW/cm^2)	0.89
Pressure: P (GPa)	0.36

Table 2.9: Laser parameters used by Elise Gay to record the back free surface velocity of CFRP composite [Gay 2011].

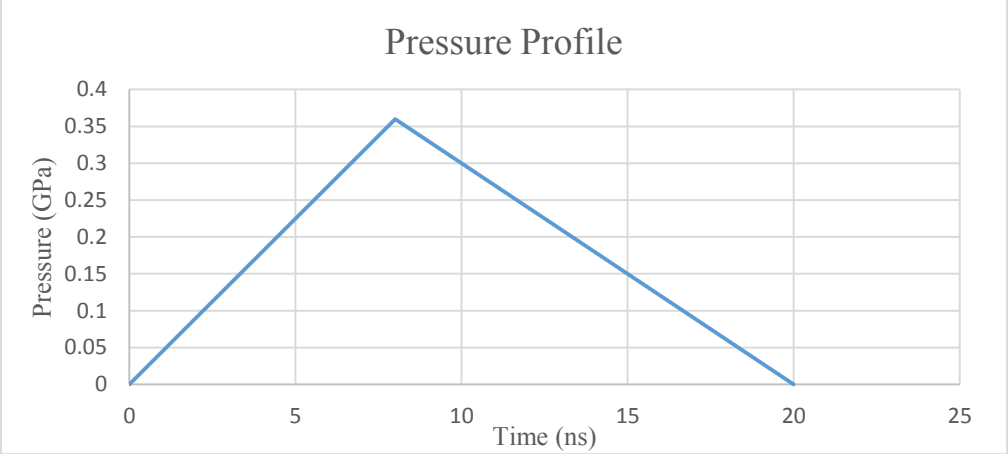

Figure 2.11: Manually adjusted pressure profile according to laser parameters given in Table 2.4.

The conditions of modeling were retained as mentioned in section 2.3.2.2. The computed back free surface velocity of a 4 ply CFRP composite panel (7.5 mm X 0.605 mm) can be seen in Figure 2.12 for 2D axisymmetric model. The results presented in Figure 2.12 closely compares with the work of Elise Gay [Gay 2011, and Gay 2014]. Table 2.10 shows the deviation in the computed results for first peak.

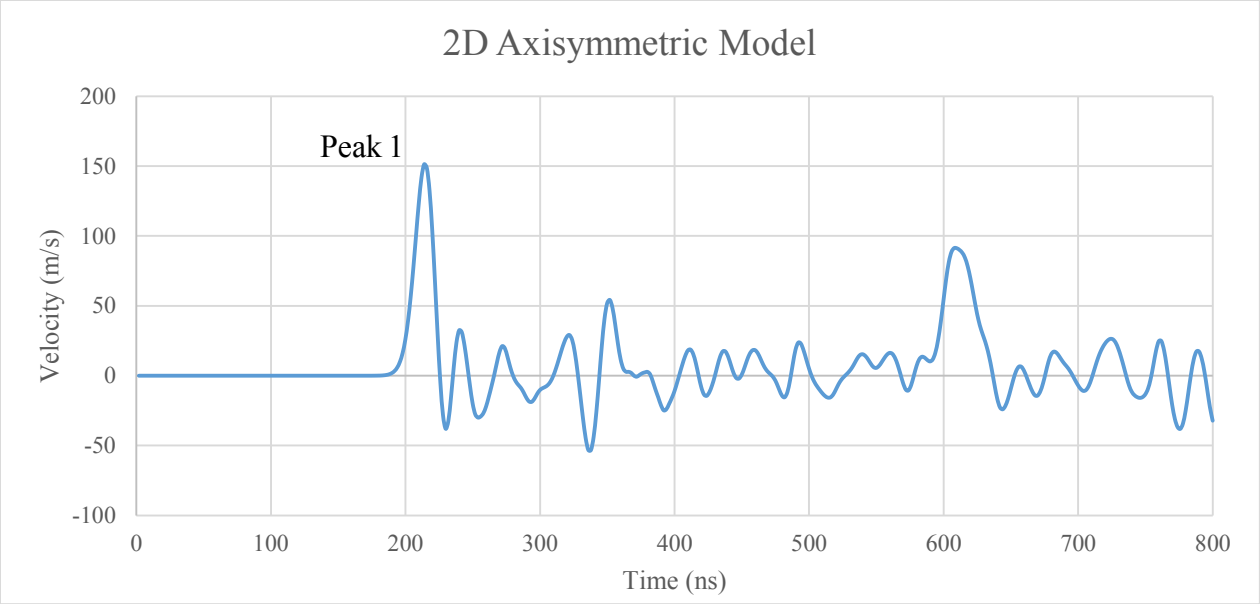

Figure 2.12: Back free surface velocity of 4-ply CFRP composite panel replicating the work of Elise Gay and validating the assumptions considered in the 2D axisymmetric ANSYS modelling.

	Peak 1		
	2D Axisymmetric ANSYS Simulation	Numerical Results from [Gay 2014]	% change
Time evolution	212 ns	200 ns	5.6
Velocity magnitude	151.31 $m.s^{-1}$	158 $m.s^{-1}$	4.4

Table 2.10: Comparison of values between ANSYS computed 2D axisymmetric model with the numerical work of Elise Gay.

A maximum difference of approximately 5% exists for the first peak for both time and velocity. Hence, it is interpreted that the numerical model for composite laminate is validated. While a 2D axisymmetric model is beneficial in understanding the stress wave propagation in composites. A 2D cross-sectional model however has advantages over 2D axisymmetric model, as illustrated in section 2.4.2.2. Figure 2.13 presents the results for a 2D cross-sectional model.

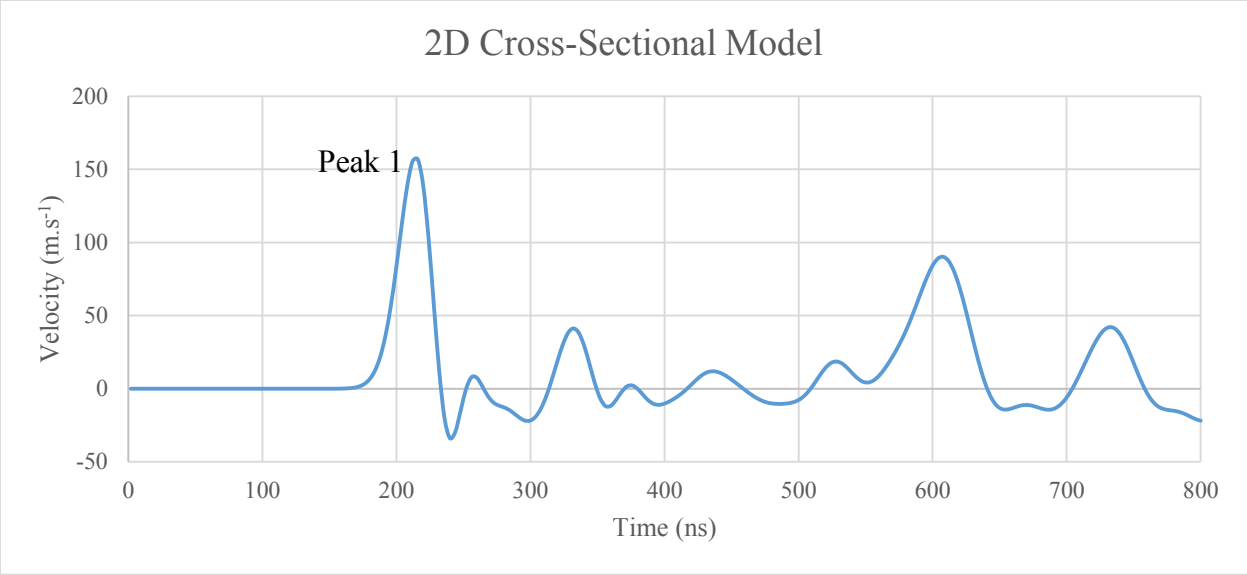

Figure 2.13: Back free surface velocity of 4-ply CFRP composite panel replicating the model used by Elise Gay and validating the assumptions considered in the in the section 2.4.2.2.

From Figures 2.12 and 2.13, it can be observed that both ToF and magnitude of the first stress wave are close enough. However, the second wave has shifted in the Figure 2.13, and is arriving at 608 ns, when compared to the results in Figure 2.12, where the second wave arrives at 612 ns. Although the results post the 400 ns slightly vary in both the 2D models, but the important aspects of first wave arrival time and magnitude remain the same. This is sufficient to carry out the NDE of composite laminate, which will be illustrated in the section 2.5. This 2D cross-sectional model, comparably posits detailed and explicit information when the simulation of a model with a delamination within it is carried out. Results of 2D axisymmetric and 2D cross-sectional model are shown in Table 2.11, where they compare favorably with variations under 4% for both velocity magnitude and ToF.

	Peak 1		
	2D Axisymmetric model	2D Cross-sectional model	% change
Time evolution	212 ns	216 ns	1.85
Velocity magnitude	151.31 $m.s^{-1}$	156.91 $m.s^{-1}$	3.57

Table 2.11: Comparison of values between ANSYS computed 2D axisymmetric model and 2D cross-sectional model.

An understanding of the stress wave propagation within the laminate is needed to assess the results properly, during the simulation of models with or without a delamination within them. Next section briefly describes the stress wave propagation in a composite laminate using the results of 2D cross-sectional model.

2.4.2.4 Discussion of stress wave propagation

It can be noticed from the results presented in Figure 2.13 that the first principal stress wave arrives at the back free surface at 216 ns for a laser impact pressure of 0.36 GPa, and the second acceleration arriving at the back free surface at 608 ns. This calculated back free surface velocity, corresponding to the manually predicted pressure profile presented in Figure 2.11, correlates with the numerical study carried out 2D axisymmetric model in the aspects of both ToF and magnitude of velocity. The reduction in the magnitude of the second principal stress wave arriving at the back surface at 608 ns can be attributable to the material hydrodynamic damping and the attenuation of energy [Gay 2014 a, and Dhulkhed 2016].

The velocity at the point of impact on the impact side of the composite model is also calculated, and Figure 2.14 shows the calculated velocity over time. It can be noticed from Figure 2.14 that the first major acceleration arrives at the surface of impact at 412 ns, that is to say the stress waves take 206 ns to propagate from impact surface to the back surface and 206 ns to return to the impact surface. Hence, the nature of variation of time evolution of stress waves is directly dependant on the thickness of the specimen, should the properties remain same.

Figure 2.15 describes the propagation of principal stress wave on a space-time diagram as a function of thickness and time. However, this diagram ignores the reflections at every interface. The observation of back free surface velocity from Figure 2.13 can be related to the wave propagation within the material depicted in Figure 2.15. This leads to the understanding of the principle as follows: The load at time 0, on the front surface will induce a compression hence a compressive stress wave shall propagate through the material arriving at the back surface at 216 ns (first longitudinal wave). This wave then reflects from the back surface and propagates as a tensile wave reaching the impact surface at approximately 200 ns. From the space-time diagram, it can also be interpreted that the second longitudinal wave arriving at the back surface at 608 ns, and this would be a stress wave with reduced magnitude for both compressional and the tensile wave.

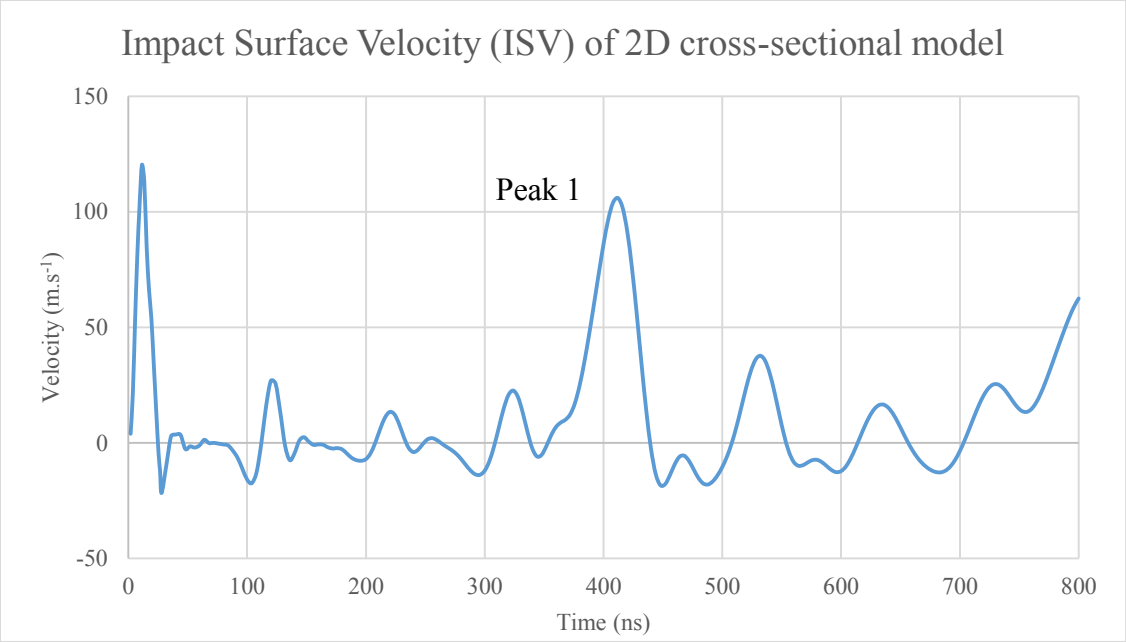

Figure 2.14: Calculated velocity of impact surface of a 4-ply composite laminate on a 2D cross-sectional model.

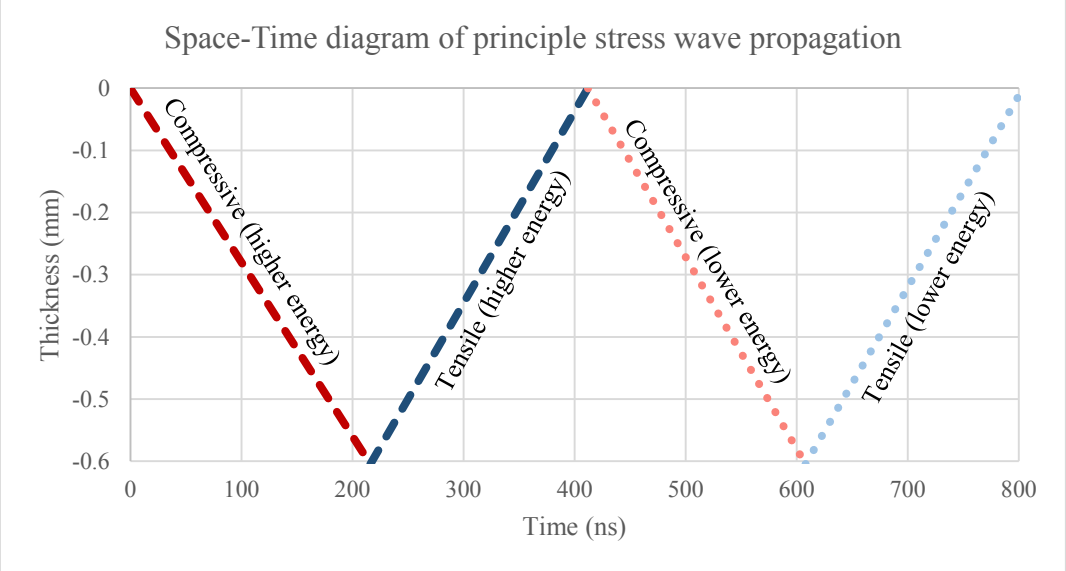

Figure 2.15: Space-Time diagram of the principal stress wave propagation through the thickness of the target material.

Having understood the time evolution of stress waves it is now essential to understand the effect of variation of different parameters on the mechanics of stress wave propagation.

2.5 Effects of variation of parameters

With the successful validation of mathematical models for aluminium, copper with nickel coating, and CFRP composite laminate, now the exploration of variation of different parameters, such as laser specifications, geometry, artificially created flaws, and the material properties, on the propagation of stress waves on CFRP composites can be easily carried out.

2.5.1 Properties

A detailed numerical study has been conducted by Elise Gay [Gay 2011]; some of the important observations are described below –

- The properties such as, density (ρ) and speed of sound wave (C_0) correctly define the impedance ratio between the ply and the interply. A change of one of these two parameters modifies the amplitude of the velocity peaks. The speed of the waves especially affect time synchronization profiles, and induce significant differences in stress wave outlets.
- The transverse modulus of elasticity or Young's modulus (E_T) has a moderate influence on the initial increase of velocity, and hence the wave propagation is within the limits of the interval of variations. An elevation of the modulus provides a very slight approximation of the velocity shifts, with the proportionality ratio existing between the velocity of the waves and the juncture of the modulus.

2.5.2 Morphology

The effect of a variation in thickness, of the surface layer (on the impact surface) to the total constant thickness, on the free surface velocity profile contain differences, representative of experimental dispersion. The emergence of incident stress waves fall out of synchronization when the thickness of the first layer of epoxy increases: the speed of the waves in the interply is lower than the homogenized ply and delays the emergence of incident wave. The differences in velocity magnitude is as well disparate.

This study shows the significant influence of layer thickness on wave propagation and the variable velocity profiles. The relevance of the model is then based primarily on the right representation of the geometry of the laminate according to the fabrication and experiment.

2.5.3 Effects of variation of laser impact parameters

Hitherto the simulation of laser generated stress waves in the target material was carried out for the laser with high energy and low repetition rate. These lasers are comparatively expensive than the high repetition rate and low energy lasers. Thus, by simulating the propagation of stress waves generated by substituting the parameters of a low cost laser with high repetition rate and low energy, it shall become very clear whether these lasers find any applicability in the NDE of any material. The properties and morphology of the model were retained as set by Elise Gay [Gay 2014]. The pressure in the simulation was scaled down to 0.081 GPa to account for the laser parameters mentioned in Table 2.12, and Figure 2.16 shows the pressure profile.

Impact Spot: d (cm)	Pulse Duration: τ (s)	Energy: e (J)	Intensity: Φ ($GW.cm^{-2}$)	Pressure: P (GPa)
0.02	14.10^{-9}	$0.2.10^{-3}$	0.045	0.081

Table 2.12: Parameters of a high repeatability and low energy laser.

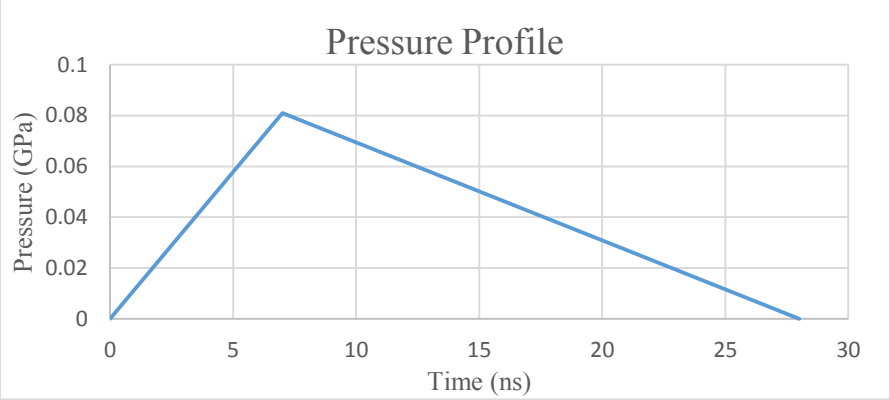

Figure 2.16: Pressure profile adjusted for low energy laser, under the assumption that similar irradiation conditions are maintained as set by Elise Gay [Gay 2011].

Table 2.13 describes the simulation parameters. Figure 2.17 shows the back free surface velocity as a function of time for an applied load of 0.081 GPa. From Figures 2.13 and 2.17 it can be noticed that the first wave arrival time at the back surface remains the same regardless of the pressure magnitude. However, the velocity reduces relative to the reduction in pressure. Table 2.14 compares the results between the high-energy laser (Figure 2.13) and low energy laser (Figure 2.17). Similarly, from Figure 2.13 it can be noticed that, the second wave arrives at the back surface at 608 ns, and the second wave for the reduced pressure arrives at about 616 ns. The change in

arrival time of the stress wave can be attributed to the small spot size (200 µm), leading to a broadband nature of stress wave propagation.

	CFRP	Epoxy
Young's modulus: E (GPa)	12.6	5.2
Density: ρ ($kg.m^{-3}$)	1630	1260
Poisson's ratio: ν	0.3	0.35
Speed of sound wave: C_{0T} ($m.s^{-1}$)	3225.81	2573.62
Element Size: Δl (mm)	0.013	
Time Step: Δt (s)	$4.2.10^{-9}$	

Table 2.13: Simulation parameters for the CFRP target with respect to the properties of carbon/epoxy ply and epoxy interply.

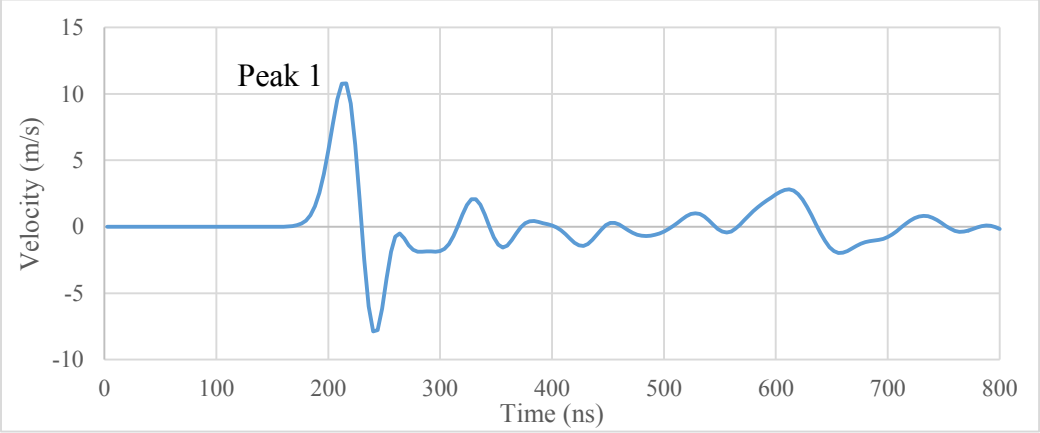

Figure 2.17: Calculated back free surface velocity for a pressure generated by a low energy laser.

	Peak 1		
	High energy laser ($\Phi = 0.89$ GW.cm^{-2}) (Figure 2.13)	Low energy laser ($\Phi = 0.045$ GW.cm^{-2}) (Figure 2.17)	% change
Time evolution	216 ns	216 ns	0
Velocity magnitude	156.91 $m.s^{-1}$	10.792 $m.s^{-1}$	93.12

Table 2.14: Comparison of results for a model with two different laser parameters.

From Table 2.14, it is understood that, the reduction in intensity is at 94.94 %, when the parameters of a low energy laser are considered for calculating the pressure. This percentage reduction is proportionally seen in the percentage change in the velocity magnitude.

2.5.3.1 Study of the effect of a delamination on back free surface velocity

With the clear understanding of the stress wave propagation in the CFRP composite model, it now becomes simpler to simulate the effect of a delamination on the back free surface velocity. The numerical model and the loading parameters of the high repetition rate and low energy laser as mentioned in Table 2.12 are retained for this study. When the probing point is on the back surface and the laser impact is as illustrated in Figure 1.8, the set-up replicates the through-transmission technique of NDE as discussed in section 1.4.4.3. A delamination was introduced in the mid interply of the model to analyze the behaviour when a discontinuity is encountered by the stress waves propagating in the material. The size of the delamination introduced is 0.25 mm X 0.01 mm, and can be seen in Figure 2.18.

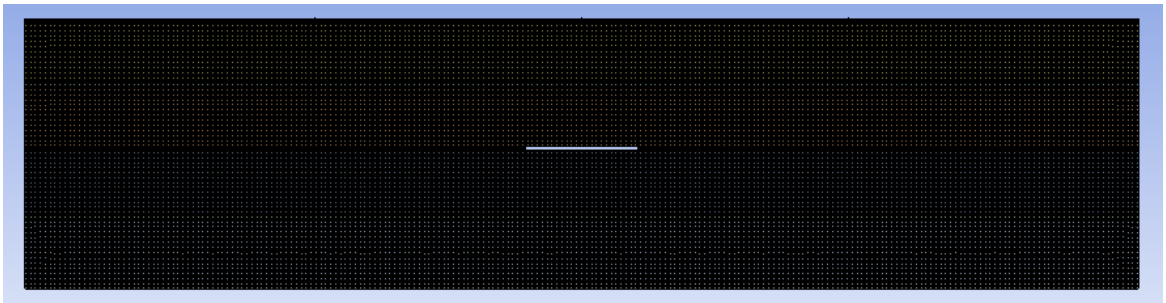

Figure 2.18: 2D cross-sectional model with an artificial delamination, in this picture the delamination is in the middle interply.

The simulation was carried out with a pressure load of 0.081 GPa to note the difference in the behaviour of the numerical model. The back free surface velocity of the numerical model with an artificial delamination as a function of time can be seen in Figure 2.19.

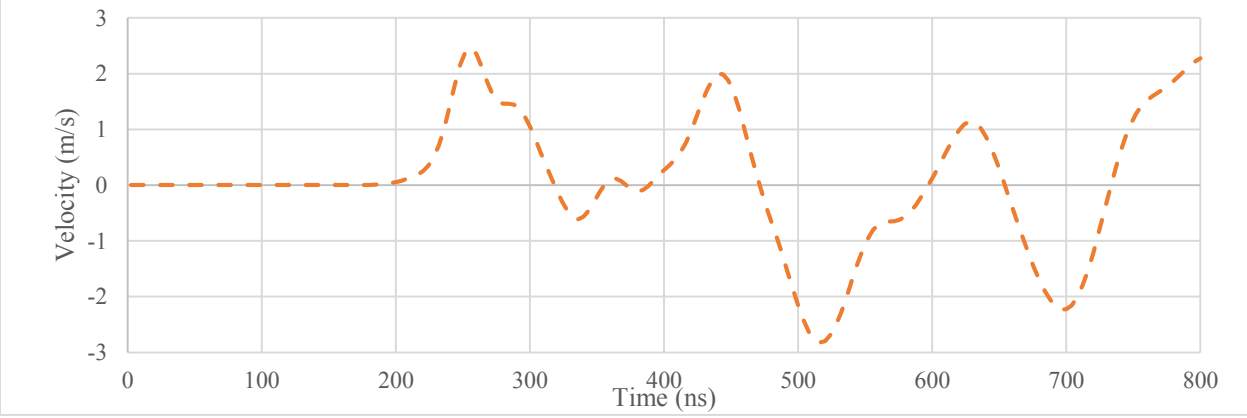

Figure 2.19: Computed back free surface velocity for a model with a delamination in the middle interply of a 4-ply laminate.

From Figure 2.19, it can be interpreted that, the reduction in the back free surface velocity magnitude of the first wave that arrives, is significantly reduced due to the discontinuity in stress wave propagation. However, the time evolution of the principal stress wave remains almost the same, as compared to the numerical model without any artificial delamination from Figure 2.17. The comparison of the two simulation results is shown in Figure 2.20.

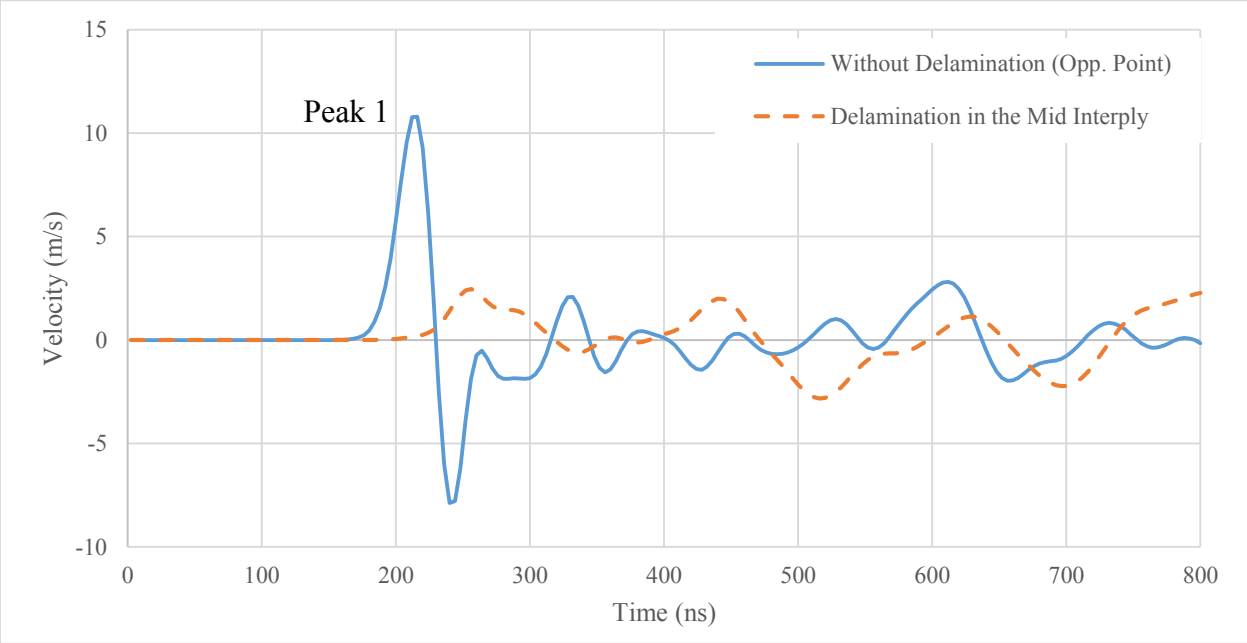

Figure 2.20: Comparison of back free surface velocity as a function of time of models without and with a delamination.

The role of discontinuity in stress wave propagation, due to delamination, leading to reduction in back free surface velocity is shown in Figure 2.21. It can be noticed that the pressure is deposited on the specimen which generates stress waves in Figure 2.21-a. When these stress waves encounter a discontinuity due to delamination, the wave propagation is interrupted and hence the velocity of back free surface is reduced as seen in Figure 2.21-b. These waves reflect from the surface of the delamination as shown in Figure 2.21-c, and this behavior of the stress waves continues until the waves attenuate. One important observation that can made here is that, if the laser beam diameter is smaller than the size of the delamination, the stress waves shall be completely shadowed by the delamination, resulting in minimal surface motion on the back surface. In this work, the computation was carried out with an impact spot size of 200 µm, and the delamination has the dimensions of 250 µm X 10 µm. Hence, it is reasonable to imply that the stress waves are eclipsed by the delamination. However, this phenomenon requires an experimental validation.

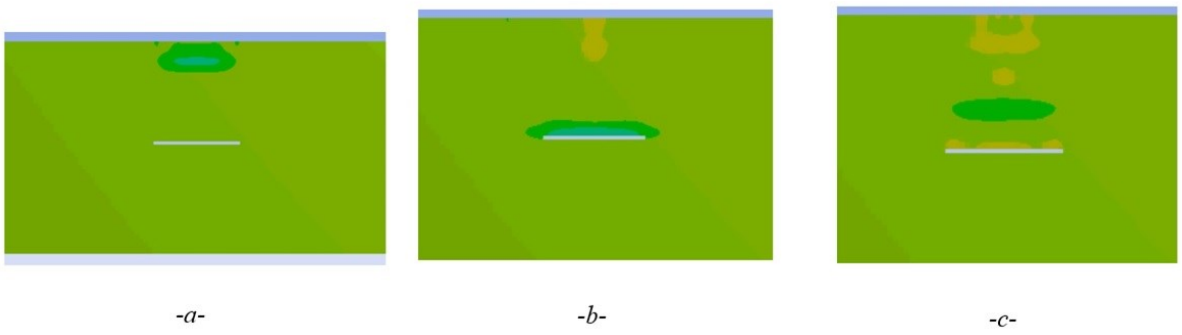

Figure 2.21: Stress wave propagation in the model with an artificial delamination in the middle interply.

The laser ultrasound NDE of a material requires proper understanding of the behaviour of the specimen post the laser-matter interaction to characterize the size and depth of the flaw(s) within the laminate. From Figure 2.13, 2.14 and 2.20, it is easy to interpret that the time evolution of the stress waves change with respect to the depth of the surface on which these waves may fully or partially reflect, and as well the location of the probe point. Keeping the location of probe point at the back surface, the simulation is carried out by maintaining the same dimensions of the delamination and only varying the depth by introducing the delamination at different interplies within a 4-ply laminate. Figure 2.22 shows the calculated back free surface velocities with delaminations at different interplies. i.e., at different depths.

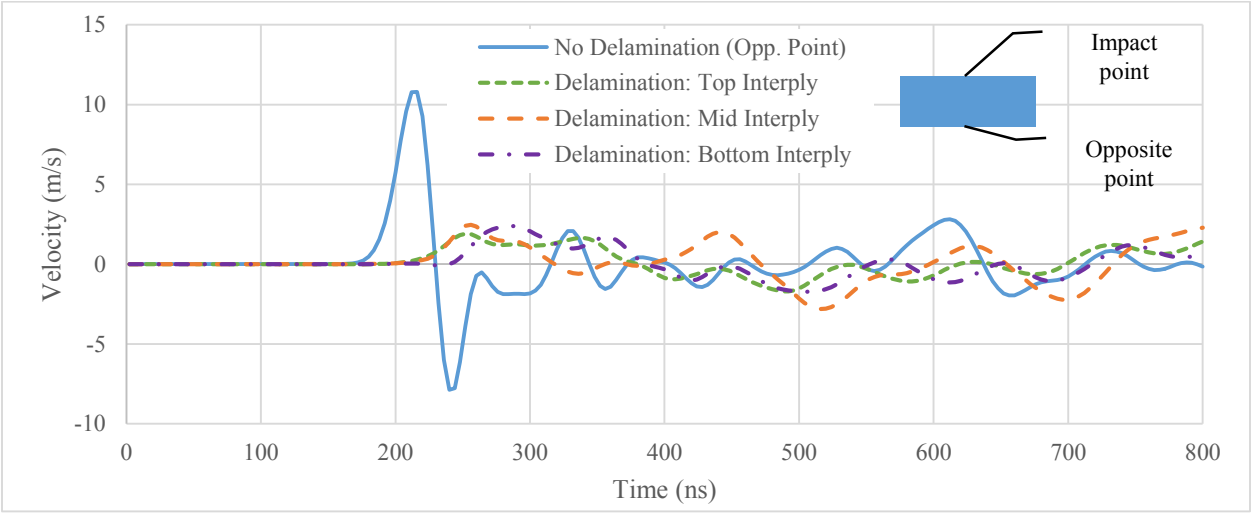

Figure 2.22: Comparison of back free surface velocities of the model without any delamination and the models with delaminations at different depths (probe at opposite point).

From Figure 2.22, the calculated back free surface velocities of the model with delamination at different depths does not provide any indication in finding out the depth of the delamination. It is

mainly attributable to the size of the delamination and the laser spot size. Thus, it requires the probing point be relocated to a location, wherein the results attained are comparable.

2.5.3.2 Study of the effect of a delamination on impact surface velocity

Here, the velocity probe point is relocated at the location of the laser impact, and the velocities of the surface of laser impact were computed for the models with delamination at different depths/interplies and the results were compared with the model without any delamination. This set-up replicates the pulse-echo technique of NDE as discussed in section 1.4.4.1. Figure 2.23 shows the calculated velocities of the impact surface for all the models under consideration.

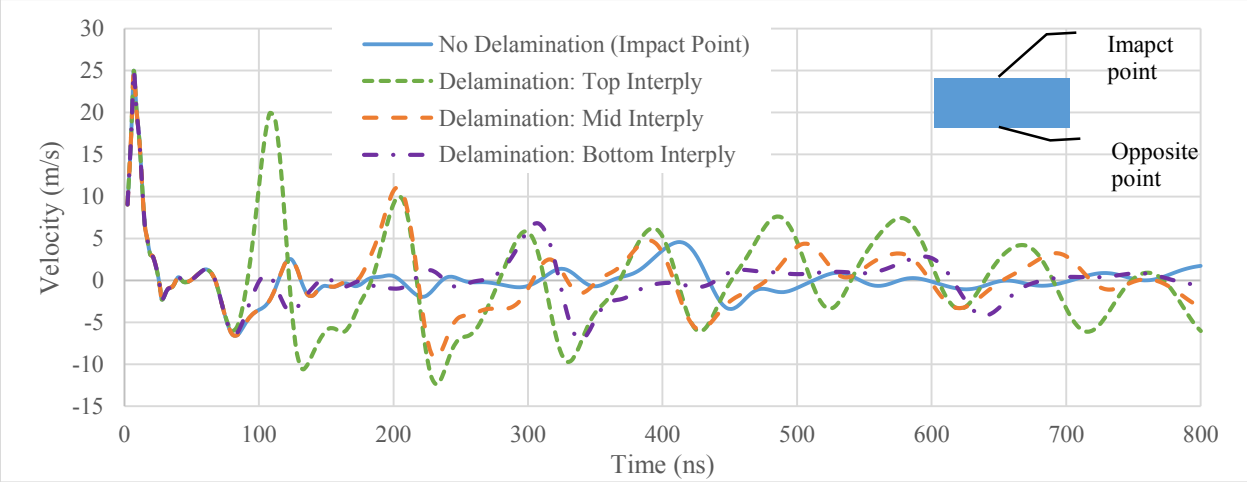

Figure 2.23: Comparison of impact surface velocities of the model without any delamination and the models with delaminations at different depths (probe at impact point).

The velocities calculated at the surface of laser impact do provide an indication of depth of delamination. It can be observed from Figure 2.23, the first principal stress wave measured at the location of laser impact for all the models under consideration follow a trend wherein a difference persists in the magnitude of velocity and the ToF. This magnitude of velocity is directly related to the ToF of the stress waves, as the stress waves experience attenuation, which will lower their energy when they propagate much deeper through the thickness of the composite laminate. The geometry and thicknesses of plies and interplies can be seen in Figure 2.24.

The first major velocity measured at the impact surface post the reflection of stress waves at the back surface for the model without any delamination is at 404 ns. The reason for lower velocity magnitude is that the waves travel through the thickness of 0.605 mm to reflect at the back surface and the stress waves travel through the same thickness to reach the impact surface where the

velocities are measured. Similarly, if the stress waves encounter a discontinuity closer to the impact surface, the waves shall attenuate less and the magnitude of velocity will be higher. The velocity curve for the delamination at the top interply i.e., right below ply 1, has its peak measured at 108 ns at a magnitude of 19.923 $m.s^{-1}$. Same trend follows for the delamination at middle interply wherein the peak is measured close to 204 ns at a magnitude of 11.084 $m.s^{-1}$, and for the delamination at bottom interply wherein the peak is measured close to 308 ns at a magnitude of 6.781 $m.s^{-1}$. The reason for the variation in the time evolution of ToF of the stress waves is due to the variation in the thickness of ply above the bottom interply, which can be seen in Figure 2.24.

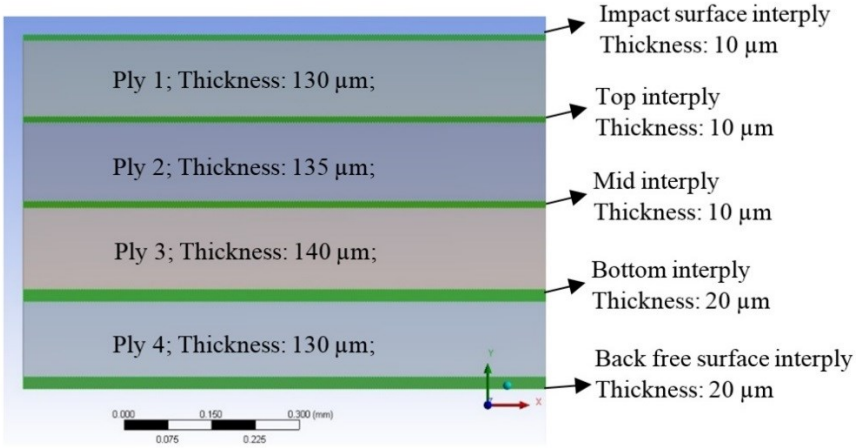

Figure 2.24: 2D representation of the laminate and thicknesses of homogenised carbon/epoxy plies and epoxy interplies.

A comprehensive study by simulation of stress wave propagation in composite laminates and noting the changes at every interply for better understanding the adaption of laser ultrasound NDE, has now been carried out. Thus, it now becomes very important to explore a less time consuming and more efficient simulation process. This can be achieved by incorporating changes in the numerical model of composite laminate. Next section discusses the simulation with a simpler numerical model.

2.5.4 Variation in numerical model for efficient simulation

In this section, modelling of composite laminate with homogenised outer zone has been illustrated. It is well understood from the previous sections that, the stress wave propagation zone is mostly near the laser impact region; hence, a biased meshing was adapted to save the computation time. To reduce the computation time further, the zone that is out of the stress wave propagation region

is homogenised and all the node to node connections between plies and interplies were eliminated. Figure 2.25 represents the numerical model with homogenised outer zone. The properties assigned to the plies and interplies positioned in the stress wave propagation zone remain the same as mentioned in Table 2.8.

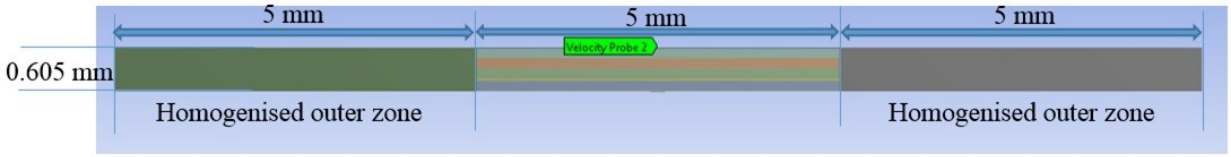

Figure 2.25: Numerical model (15 mm X 0.605 mm) with homogenised outer zone of laminate.

The properties assigned to the outer zone is based on the proportions of thicknesses of plies and interplies shown in Figure 2.24, and is illustrated below:

Total thickness of laminate, T_L = 0.605 mm;

This thickness is the summation of thicknesses of plies (T_P) and thicknesses of interplies (T_I), i.e., $T_L = \Sigma T_P + \Sigma T_I$;

From Figure 2.24, ΣT_P = 535 µm; and ΣT_I = 70 µm;

Hence, it can be estimated that homogenised carbon/epoxy plies are 88.43% of thickness of laminate, and epoxy interplies are 11.57% of thickness of laminate. With this understanding, the proportional values of properties such as, density, elastic modulus, Poisson's ratio, and bulk modulus can be deduced. The deduced properties are given in Table 2.15.

Density, ρ ($kg.m^{-3}$)	Modulus of elasticity, E (GPa)	ν	G (GPa)
1587.19	E_T = 11.74 E_L = 178.35	ν_{LT} = 0.305 ν_{TZ} = 0.279	G_{LT} = 4.52 G_{TZ} = 4.16

Table 2.15: Homogenised ply and interply properties.

The properties mentioned in Table 2.15 are assigned to the homogenised outer zones. The computation was carried out with laser parameters as used by Elise Gay, mentioned in Table 2.9. The computed results for velocity over time on the back surface and impact surface with this numerical model are shown in Figures 2.26-a, and 2.26-b respectively.

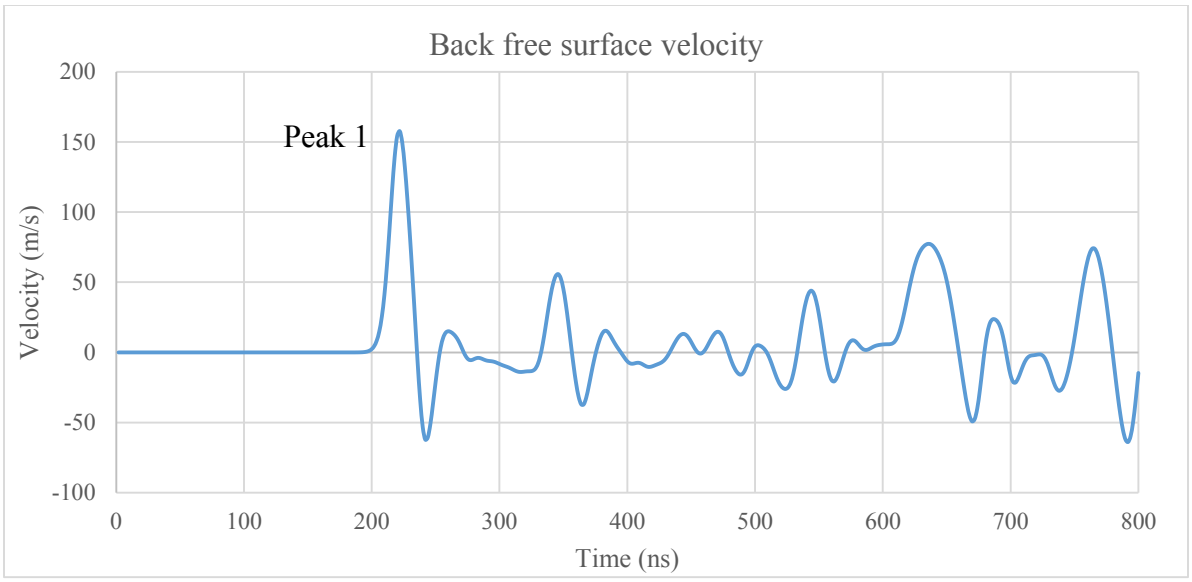

-a-

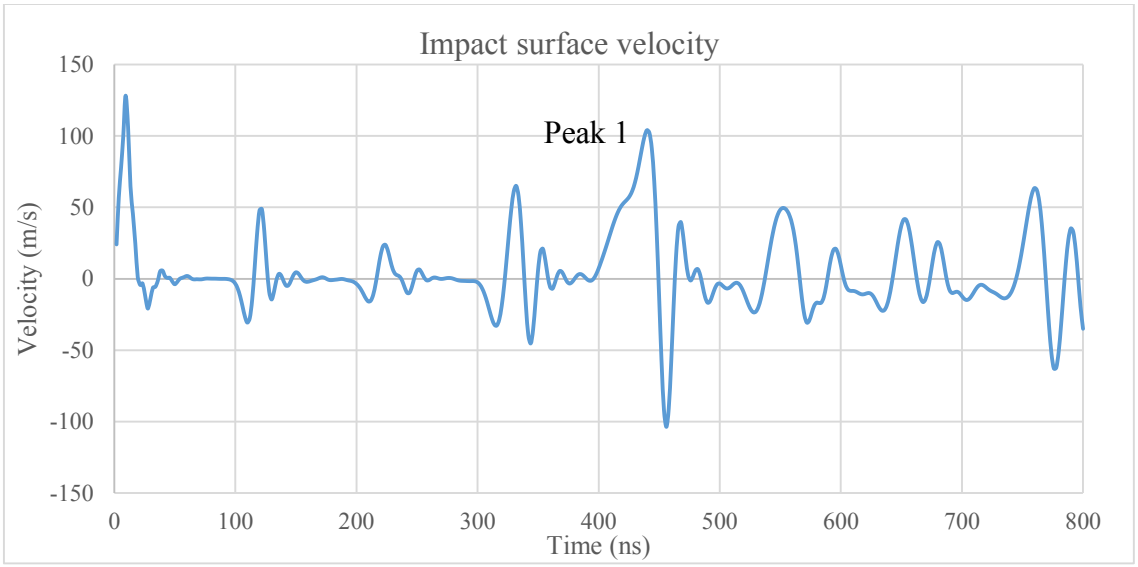

-b-

Figure 2.26: Computed results of numerical model with homogenised outer zone; -a- back free surface velocity over time; -b- impact surface velocity over time;

Comparison of Figure 2.13 and Figure 2.26-a for back free surface velocity shows no significant change for the first peak. Similarly, comparison of Figure 2.14 and Figure 2.26-b for impact surface velocity shows a minimal change in the time evolution for the first peak. However, the magnitude of velocity has a significant variation. This is due to the coarser mesh around the partition, which was created for biased meshing. The stress waves, due to this coarser mesh, would propagate more non-uniformly, and this effect is more pronounced when the waves are reflected

on the back surface. Hence, a variation is not noticed at the back surface and is only noticed at the impact surface. However, the explanation posited here is based on probable causes. The percentage change is mentioned in Table 2.16.

	Peak 1 (back free surface velocity comparison)		
	2D Cross-sectional model (Figure 2.13)	2D-homogenised outer zone (Figure 2.26-a)	% change
Time evolution	216 ns	221 ns	2.26
Velocity magnitude	156.91 $m.s^{-1}$	157.71 $m.s^{-1}$	0.51

-a-

	Peak 1 (impact surface velocity comparison)		
	2D Cross-sectional model (Figure 2.14)	2D-homogenised outer zone (Figure 2.26-b)	% change
Time evolution	412 ns	440 ns	6.57
Velocity magnitude	106.02 $m.s^{-1}$	104 $m.s^{-1}$	1.9

-b-

Table 2.16: Comparison of results for peak 1 between 2D cross-sectional model and 2D cross-section with homogenised outer zone model: -a- back free surface velocity, -b- impact surface velocity.

Apart from less deviation in the time evolution, this computation consumes about $2/3^{rd}$ of the time for completion, when compared with the computation of numerical model described in section 2.4.2.2. Hence, it is inferred that the homogenised model can be used if the computation of thicker composite laminates needs to be carried out.

However, if there is a requirement to simulate the surface waves in composite laminates, one must be careful in using this type of numerical model. In addition, if the laser spot is not circular, using this type of numerical model may impart errors.

2.6 Summary

In this chapter, a preliminary numerical model for laser ultrasound NDE was created for metals. The modelling environment considered were both 3D and 2D. The results of the back surface velocity from the simulation was then compared with the experimental results of NDE on aluminium alloy and copper-nickel alloy available from the literature. Successful validation of this model enabled to study the stress wave propagation in composites. For the composite simulation,

axisymmetric and cross-sectional models were studied, within the 2D environment. The axisymmetric model is beneficial in understanding the mechanism of stress waves, whereas with the cross-sectional model explicit results can be obtained at every ply/interply of composite laminate. Hence, a 2D cross-sectional model was adapted for further studies.

This study reviewed the changes in the parameters such as, material properties, material morphology, parameters of laser that is of high repetition rate and low energy, and a discontinuity in the form of delamination within the material. With the low energy laser, a reduction in the magnitude of velocity is observed, proportional to the reduction in laser intensity. The ToF however, remained the same, regardless of pressure magnitude. A comparative analysis was done to characterize the depth of delamination, by recording the results on the back free surface. It is found that, with this set-up, the depth of delamination is difficult to predict. Relocation of probing point at the surface of impact eliminated this problem. With this set-up, the finding out the depth of delamination would essentially be the changes observed in, ToF and magnitude of velocities. In addition, it was noted that the reflection of waves due to discontinuity is highly dependent on the spot size of laser and the size of delamination. For higher simulation efficiency, the numerical model was changed wherein the region/zone that is out of the propagation zone is homogenised. It was noticed that the deviation in the results for the homogenised numerical model are minimal. This numerical model reduced the time of computation by approximately 33%.

In the next chapter (Chapter 3), the experimental verification of characterizing the depth of discontinuity/delamination using the speed of stress wave propagation (speed of sound) and calculating the ToF will be done.

CHAPTER 3. Fabrication and experimental study of NDE of CFRP composites

3.1 Introduction

The numerical study carried out in the previous chapter has posited the knowledge of different parameters and their effects on the response of composite laminates for the successful NDE. To follow up with that work, in this chapter the composite laminates will be subjected to the real-time NDE, in a state-of-the-art facility for laser ultrasound NDE of materials available at Tecnar Automation Ltée. The experiments will be conducted in both the through-transmission and pulse-echo set-ups. The direct mode of ablation is adapted for the experimental results. The detection laser records the change of phase of the light reflected from the laminate, which is demodulated into the displacement, while the numerical simulation results are velocity. However, according to the theory, the time evolution of the stress waves must remain the same. Hence, it is reasonable to use the displacement results as well, to study the ToF experimentally.

3.2 Fabrication of CFRP composite laminates

The composite panels that are fabricated for NDE, and to understand the complementing aspect of the numerical study, are of two types.

- CFRP composite laminate without any delamination
- CFRP composite laminate with a delamination

The fabrication details such as, the curing cycle, lay-up/orientation and introduction of delamination are discussed in next sections.

3.2.1 Fabrication of CFRP composite laminate without any delamination

The fabrication and NDE of CFRP composite laminate without any delamination is essential to understand the changes in the laminate with a delamination. The laminate carries the details as mentioned in Table 3.1. The fabrication technique adapted is out-of-autoclave (OOA), the curing cycle is shown in Figure 3.1, and vacuum bagging arrangement is shown in Figure 3.2. Microscopic images of the laminate are shown in Figure 3.3, wherein the ply orientation can be clearly observed.

Material (prepreg)	CYCOM® 5320-1/ T650/35 3k
Cured thickness of 1 ply	0.125 mm (approx.)
Fibre	Cytec T650/35 3k
Resin	CYCOM® 5320-1
Tape	Unidirectional
Orientation	$[(0/90)_8]_S$
Dimensions (L X B X H)	50 mm X 40 mm X 4 mm

Table 3.1: Details of CFRP laminate without any delamination.

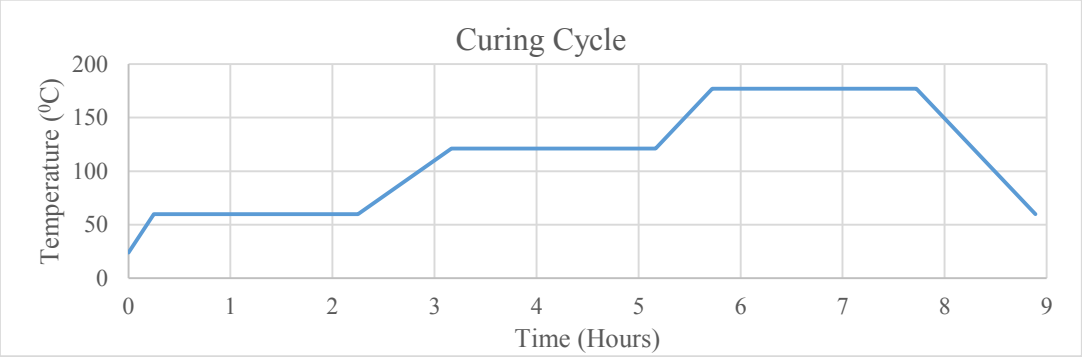

Figure 3.1: Curing cycle of CFRP composite laminate.

More information about the lay-up procedure and curing can be found in the information file available for the CYCOM® 5320-1 EPOXY RESIN SYSTEM given in the appendix.

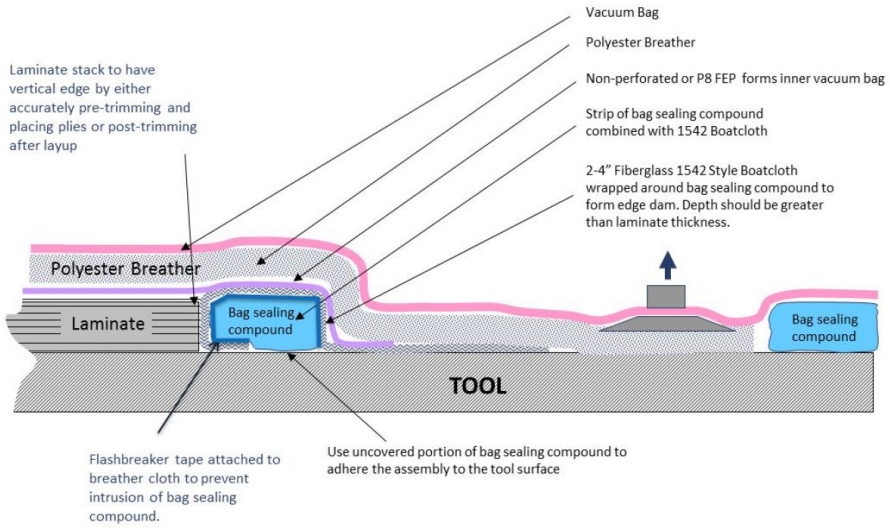

Figure 3.2: Vacuum bagging arrangement for the curing process of CFRP composite laminate as explained in the information file associated with the CYCOM® 5320-1 EPOXY RESIN SYSTEM.

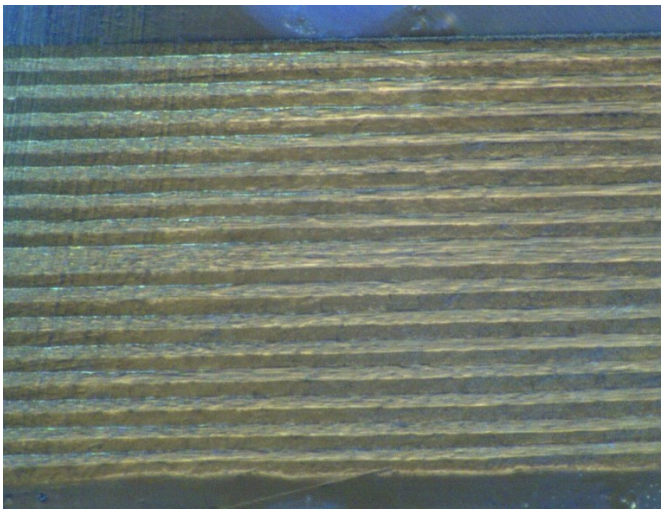

Figure 3.3: Microscopic image of the composite laminate of lay-up sequence - $[(0/90)_8]_s$.

3.2.2 Fabrication of CFRP composite laminate with a delamination

The fabrication of composite laminate with a delamination, to carry out the experiments to distinguish the change in the response of material such that successful NDE is done, involves the same vacuum bagging arrangement and curing cycle as illustrated in the previous section. The delamination is introduced by using an aluminium foil of 10 mm X 10 mm X 0.015 mm. The foil is placed at a location as shown in Figure 3.4. The location selected to create the delamination using aluminium foil can benefit in carrying out two experiments, i.e., at two different depths.

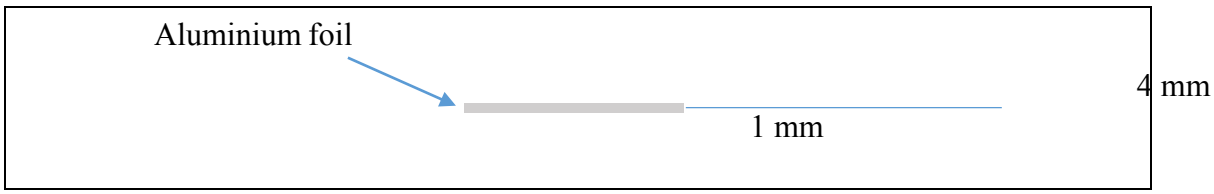

Figure 3.4: Composite laminate with aluminium foil introduced as delamination, and its position (picture not to scale).

The experiments can now be carried out for the two laminates, one with a delamination and one without a delamination, to understand the depth of delamination. This is in continuation of the numerical study carried out in the sections 2.5.3.1 and 2.5.3.2 of Chapter 2. The setting of numerical model in section 2.5.3.1 replicates the conventional through-transmission technique of NDE, and replicates the conventional pulse-echo technique of NDE in section 2.5.3.2. With laser ultrasound NDE set-up available at Tecnar Automation Ltée, both the conventional NDE set-ups will be considered to carry out the experiments. In addition, from the numerical study it was

concluded that, the numerical model setting explained in section 2.5.3.2 is effective in characterizing the depth of delamination and was proven in the numerical study, hence this shall be experimentally verified.

3.3 Ultrasound generation and detection systems

3.3.1 Laser for ultrasound generation

For the ultrasound generation, laser pulses of the order of 10 ns are used on multiple instances [Arrigoni 2008 a, Gay 2011, Sun 2013, and Karabutov 2014]. For even higher frequencies, pulse widths of the order of 100 ps (resulting in the ultrasound frequency of 100-MHz range) are needed, or even femtosecond laser systems may be necessary for GHz range. The laser power depends on the test material and if ablation is acceptable. The power of lasers ranging from few nJ to several hundred mJ have been used to produce ultrasound in structures. The choice of laser wavelength primarily depends on the absorption properties of the material. Wavelengths of lasers for ultrasound generation ranging from ultraviolet to infrared and higher have been used [Krishnaswamy 2003]. More details about the lasers for ultrasound generation can be found in [Scruby 1990]. The parameters of ultrasound generation laser at Tecnar facility whose rise time is 4 ns are given in Table 3.2.

Wavelength: λ (nm)	Impact Spot: d (cm)	Pulse Duration: τ (s)	Energy: e (J)	Intensity: Φ ($GW.cm^{-2}$)
532	0.1	10.10^{-9}	$41.7.10^{-3}$	0.53

Table 3.2: Parameters of ultrasound generation laser at Tecnar facility.

3.3.2 Optical detection system

Several methods of laser detection of ultrasound have been discussed in section 1.6 of Chapter 1, based on different types of laser interferometer (Fabry-Perot, Michelson, Laser Doppler Vibrometer, intensity modulation, dynamic holography etc.). A phase modulation interferometer has the potential to address the problems associated with other types of interferometers. For example, the surface need not be reflective, which is required for a Michelson type interferometer. In order to achieve such independence, there may sometimes be some drawbacks. For example, Fabry-Perot interferometer will filter out lower frequencies to achieve the independence. Lastly, in dynamic holography, critical response time is associated with the Photo-Refractive Crystal (PRC) process dependant on the crystal material, the applied electric field (when required) and the

total incident optical intensity. With proper choice of parameters, the PRC cannot adapt sufficiently to high-frequency modulations in the signal beam, containing the ultrasonic information, while still adapting to the low-frequency phase modulations caused by environmental conditions [Krishnaswamy 2003]. Hence, to detect the ultrasound, a Pulsed Detection Laser (PDL) coupled to a Two-Wave Mixing (TWM) laser-ultrasonic detection unit is used. The TWM is a fast-response photo-refractive based laser interferometer, which demodulates the change in phase, extracting the ultrasonic information from the PDL light backscattered from the target's surface. The PDL is a frequency-stabilized long-pulse Nd:YAG laser based on a Master Oscillator Pulse Amplification (MOPA) optical setup. The parameters of PDL are given in Table 3.3. The change of phase/displacement information is processed by a band pass filter of 1 MHz to 40 MHz.

Wavelength: λ (nm)	Impact Spot: d (cm)	Pulse Duration: τ (s)	Peak Power: P (W)	Frequency: f (Hz)
1064	0.1	85.10^{-6}	250	60

Table 3.3: Parameters of phase demodulating PDL at Tecnar facility.

3.4 Experimental study

In the numerical study, two set-ups were used to record the ToF for all the models considered. Hence, similar experimental set-ups will be used to validate the theory of ToF. Figure 3.5 shows the experimental set-ups adapted.

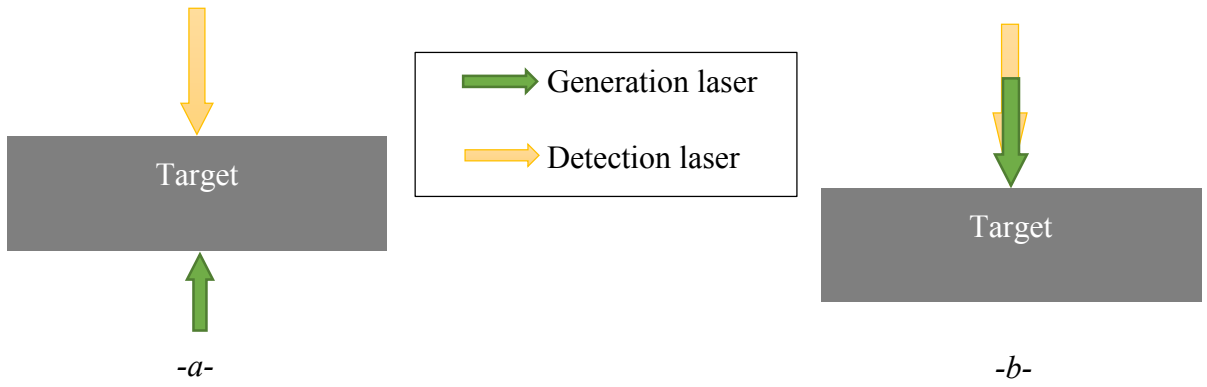

Figure 3.5: Experimental set-ups adapted: -a- through-transmission, -b- pulse-echo (picture not to scale).

Figure 3.5-a shows the through-transmission set-up, wherein the generation laser and the detection laser are aligned and the generation laser is projected on the opposite surface. From Figure 3.5-b, it can be noticed that the generation laser is adjusted to be projected on the same side as the

detection laser. To align the two laser spots, an infrared sensing card is used for detection laser, and laser light of the generation laser is turned on while the Q-switching was disabled. A burn paper is used to check the spot size of the generation laser by subjecting it to a single shot. Sections 3.4.1 and 3.4.2 present the displacement results in through-transmission and pulse-echo set-ups respectively, for both types of CFRP laminates, without and with a delamination.

3.4.1 Through-transmission replication of laser ultrasound NDE

It can be said that, the through-transmission set-up records the Back Free Surface Displacement (BFSD). These displacement results on a laminate without any delamination are presented in Figure 3.6. From Figure 3.6 it is noticed that the first stress wave arrives at the back surface at 1.53 µs and displaces the surface by 36.2 nm. This stress wave is compressive in nature and is illustrated in section 2.4.2.4. Similarly, the experiment is conducted on a laminate with a delamination. It must be noted that the experiment is conducted with only one surface of the laminate subjected to impact. This is sufficient, and section 2.5.3.1 describes the mechanism of stress wave propagation for a through-transmission set-up for a laminate with a delamination. In this mechanism, it was observed that, irrespective of the location of the delamination, the results would be of same nature due to the reflection of stress waves [Dhulkhed 2016]. Hence, conducting the experiment by generating ultrasound only on one of the surfaces is satisfactory for this work. Figure 3.7 presents the BFSD for a laminate with a delamination in through-transmission set-up.

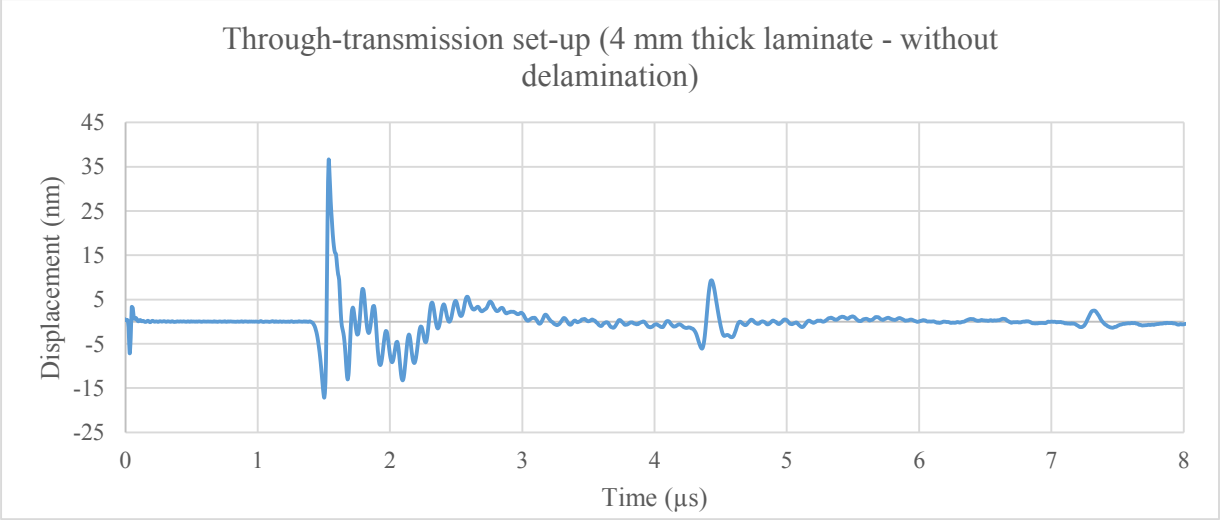

Figure 3.6: Back free surface displacement over time, in a through-transmission set-up on a target without any delamination.

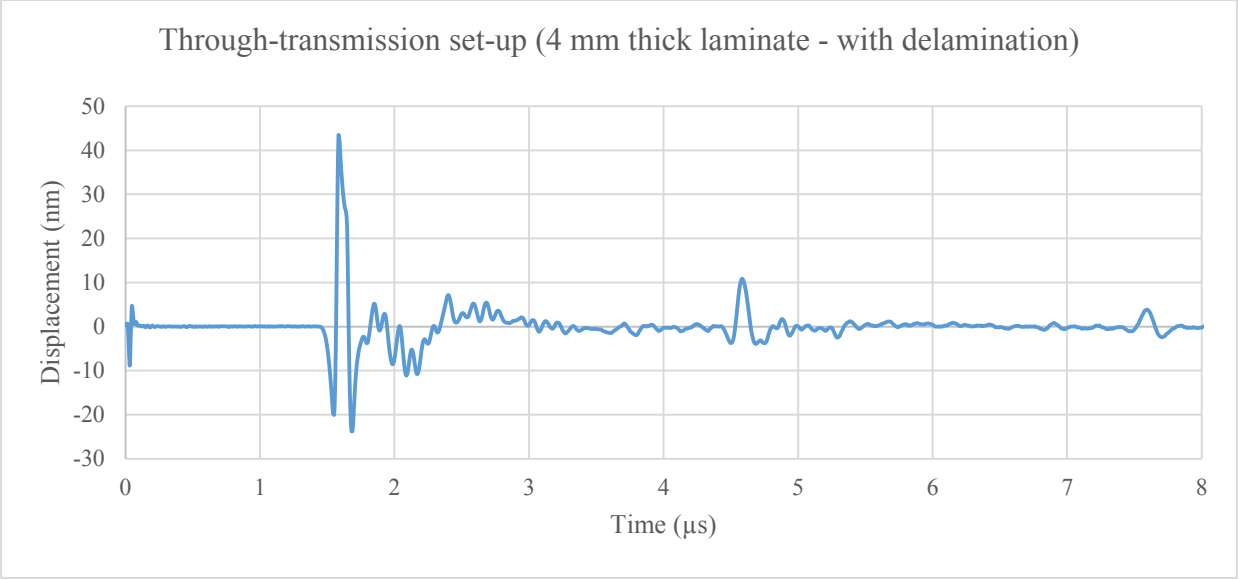

Figure 3.7: Back free surface displacement over time, in a through-transmission set-up on a target with a delamination.

Interestingly, the aluminium inclusion considered to create a delamination like feature, has transmitted the stress waves instead of reflecting them. The time evolution of the first stress wave in Figure 3.7 (1.58 µs) is close to the time evolution of the first stress wave in Figure 3.6 (1.53 µs). However, the magnitude of displacement for the first stress wave is higher when an aluminium inclusion is used (43.3 nm). The reasons for the transmission of stress waves and higher magnitude will be analysed in Chapter 4. Although, the displacement results do not correspond with the numerical study, the pulse-echo set-up is still experimentally studied in the next section.

3.4.2 Pulse-echo replication of laser ultrasound NDE

Having carried out the experimental studies for the through-transmission set-up, the experimental studies are likewise carried out for pulse-echo set-up. The Impact Surface Displacement (ISD) results are presented in Figure 3.8 for a laminate without any delamination. For the laminate with a delamination, two set of results can be obtained, i.e., delaminations at two depth levels from the impact surface, as shown in Figures 3.9. and 3.10 presents the displacement results at the two depths considered.

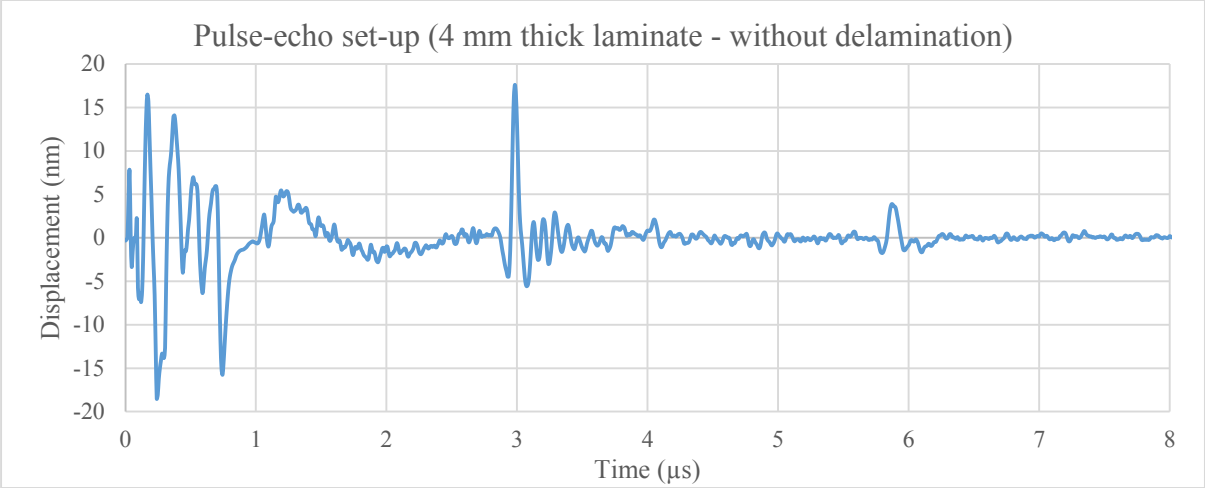

Figure 3.8: ISD results of a laminate without any delamination.

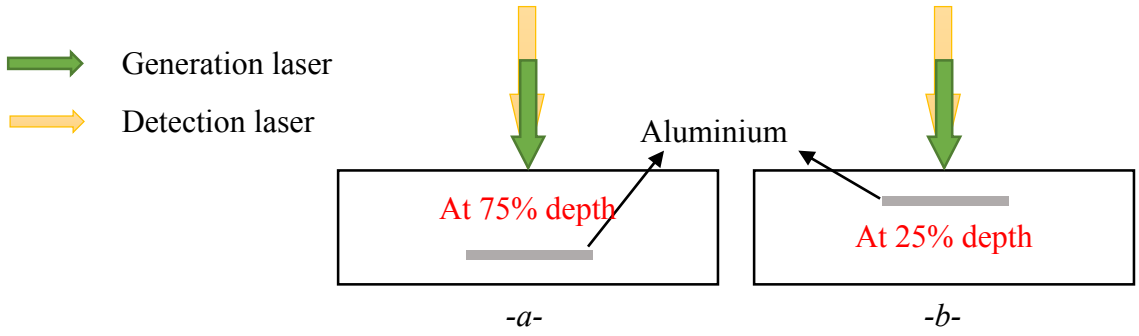

Figure 3.9: Schematic of the delaminations at two depth levels from the impact surface, -a- depth level at 75%, -b- depth level at 25%.

From the results presented in Figures 3.6 and 3.8, it is easily noticed that the arrival time has nearly doubled to 2.98 µs in pulse echo. This stress wave arriving at the impact surface is tensile in nature (refer to section 2.4.2.4). In correlation with the delayed arrival time, the magnitude of the displacement has nearly halved to a value of 17.6 nm. This is in accord with the numerical study. Hence, it can be claimed that the ToF of the stress waves can be used to characterize the depth of a discontinuity or a boundary. However, referring to Figure 3.10, it is noticed that the transmission of stress waves is still predominant at both the depth levels. This is in complete disagreement with the numerical study carried out and illustrated in section 2.5.3.2. Hence, it is imperative to analyse the role of aluminium inclusion used to create a delamination like feature. This analysis along with analysis of the through-transmission set-up will be done in Chapter 4.

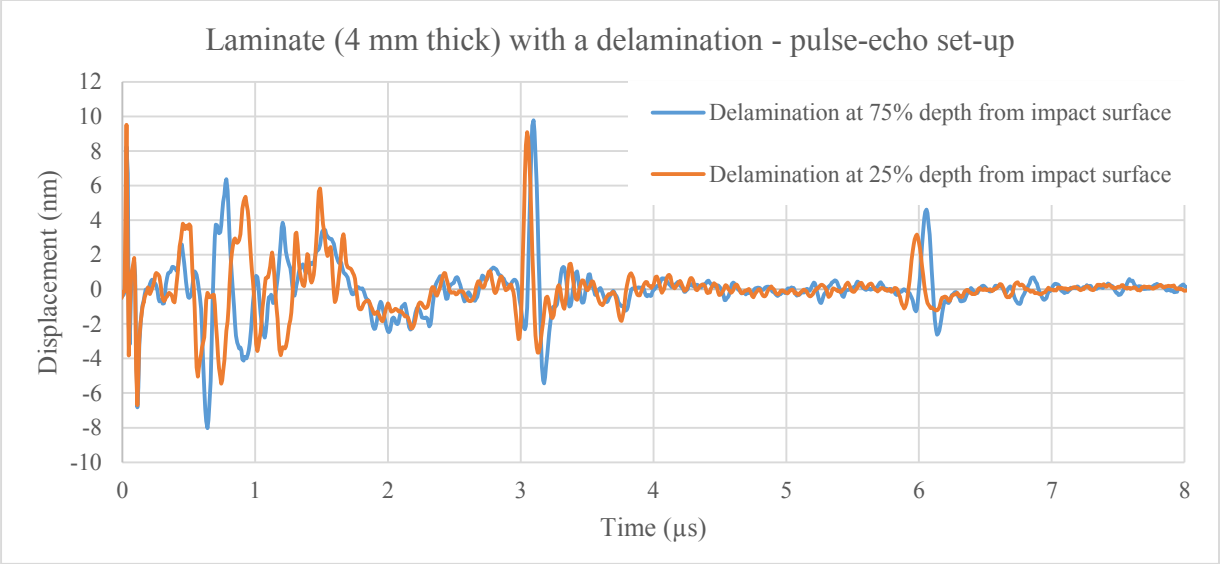

Figure 3.10: Displacement results in pulse-echo set-up for a laminate with a delamination.

Before proceeding to do this analysis, it is a good proposition to validate the concept of reflection of stress waves at boundaries by testing a sample with different thickness. With this validation, the expertise of gauging the thickness, of different materials using lasers, gains substantially, and the behaviour in the bulk of the material can also be numerically studied. Next section describes the study of ToF of stress waves on a laminate with different thickness.

3.5 Experimental study of ToF on a laminate with different thickness

To carry out this experiment, the thickness of the laminate can be either increased or reduced. Since, any increase or reduction in thickness of laminate, ToF would either increase or reduce. This increase or reduction in ToF is expected in both the set-ups. Hence, the experiments will be conducted in both the experimental set-ups adapted in the previous section. The laminate of dimensions 50 mm X 40 mm X 2 mm is fabricated. The material and curing cycle for this laminate remain the same as illustrated in section 3.2.1. The lay-up orientation of the laminate is changed to $(0/90)_8$. Figure 3.11 presents the displacement results for the laminate of 2 mm thickness in both the experimental set-ups.

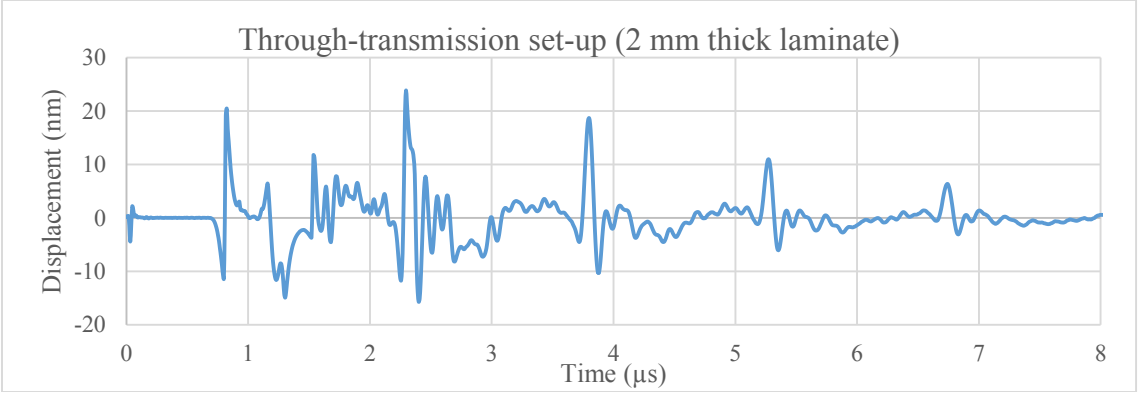

-a-

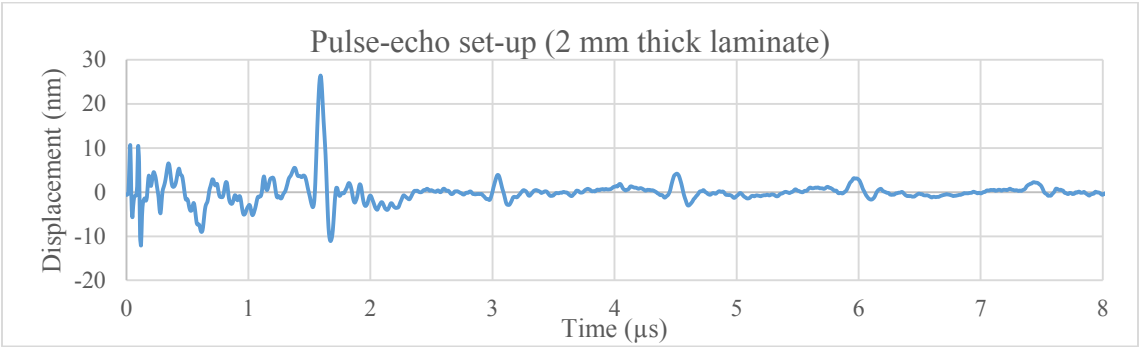

-b-

Figure 3.11: Displacement results for a 2 mm thick a laminate: -a- through-transmission set-up, -b- pulse-echo set-up.

From Figure 3.11-a and 3.11-b, it is observed that the nature of stress wave movement remains the same, as it was in a laminate of 4 mm thickness. Nevertheless, the reduction of thickness has prompted the stress wave to arrive at the boundaries early, when compared with displacement results in Figures 3.6 and 3.8. The ToF of first stress wave arriving at the detection point has nearly doubled in pulse-echo set-up (1.59 µs) when compared to the through-transmission set-up (0.82 µs). However, the magnitude displacement value has reduced in through-transmission set-up, indicating that the attenuation of energy is very high. This is in contradiction to the nature of change of values for a laminate with 4 mm thickness. Additionally, the displacement magnitudes of stress waves arriving at subsequent time intervals in the through-transmission set-up are still superior, while there is a sharp decrease in magnitudes in the pulse-echo set-up.

It is assumed that for the unexpected and contradicting displacement results in through-transmission set-up (Figure 3.11-a), small thickness variation of the laminate or the misalignment of the two beams might be the reason. Since, the small variation of thickness might as well persist

in the laminate that is 4 mm thick; even then, the experimental results did not contradict the theory. Thus, an experimental investigation of only the misalignment of one of the laser beams is necessary, to perhaps understand the anomalies in the displacement results. In the next section, the misalignment of ultrasound generation laser with respect to the detection laser axis will be performed and the effects will be studied in the though-transmission set-up.

3.6 Effects of misalignment of laser beams on results

To study the effects of misalignment of two laser beams in through-transmission set-up, the generation laser is moved by 2 mm, 5 mm and 10 mm with respect to the detection laser beam. Figure 3.12 shows the experimental arrangement to study the effects of misalignment in the results, and displacement profiles are presented in Figure 3.13. The effect of generation laser beam misalignment gets quite pronounced with increasing offsets.

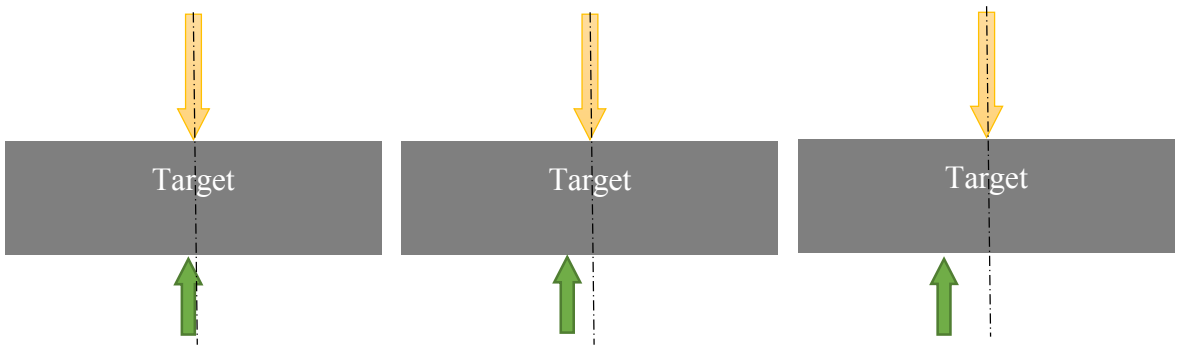

-a- *-b-* *-c-*

Figure 3.12: Experimental arrangement to study the effect of misalignment of generation laser with respect to the detection laser in a through-transmission set-up: -a- 2 mm offset, -b- 5 mm offset, and -c- 10 mm offset (Picture not to scale).

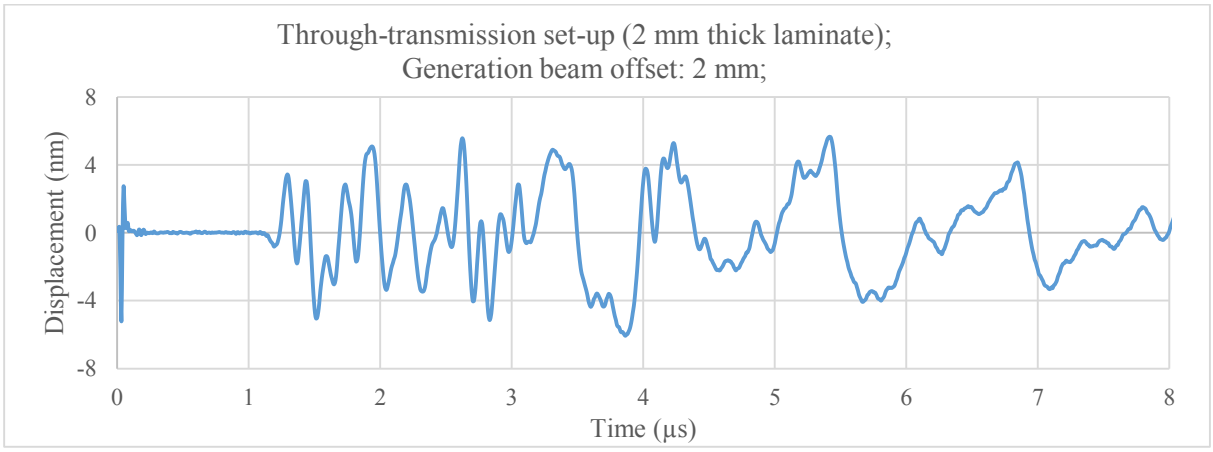

-a-

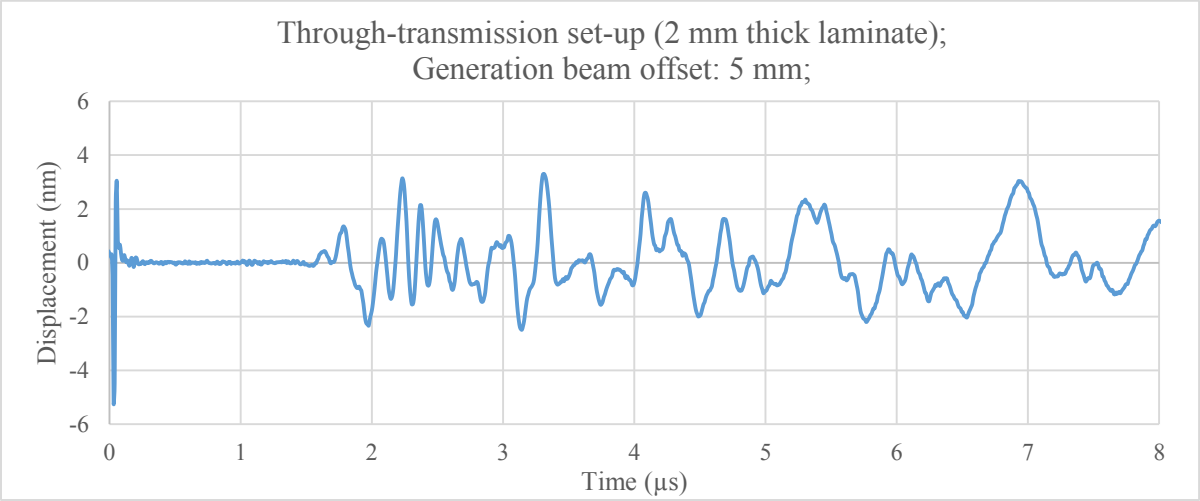

-b-

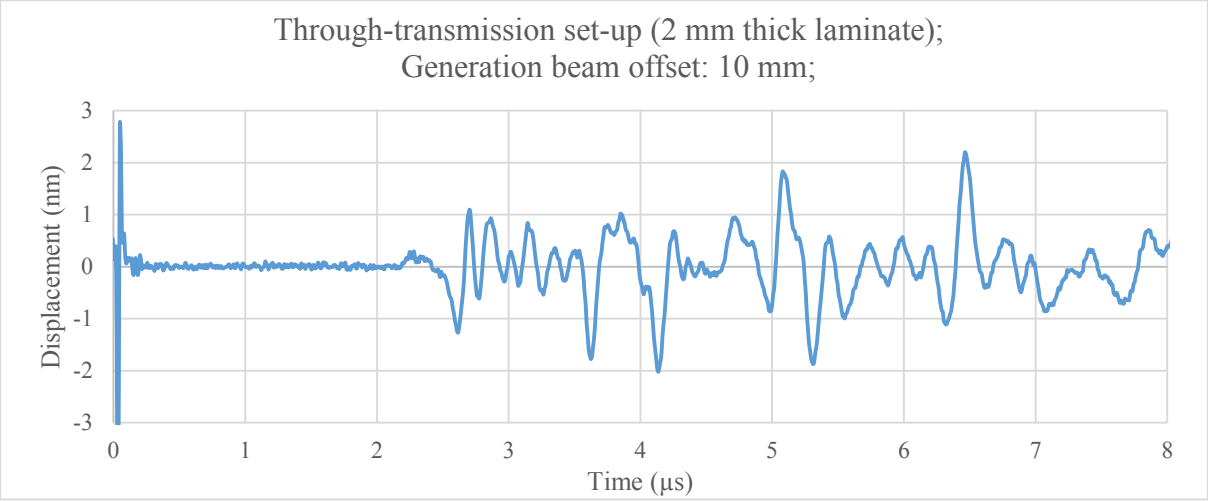

-c-

Figure 3.13: Displacement results of the generation laser beam misalignment with respect to the detection laser for, -a- 2 mm offset, -b- 5 mm offset, and -c- 10 mm offset.

Comparing Figures 3.13-a, 3.13-b, and 3.13-c, it is noticed that, with an increase in the offset/misalignment of laser beam, a reduction of the similar order in the magnitude of displacement occurs. This is due to the fact that, high magnitude stress waves propagate along the ultrasound generation beam axis, or in the volume of material that is under the region of impact spot. These waves are called as, longitudinal stress waves. These stress waves are either compressional or tensile. The stress waves that are detected at an offset of the axis of ultrasound generation beam are shear waves as illustrated in section 1.5 of Chapter 1. These shear waves possess less energy as compared to the longitudinal waves. Moreover, it can be noticed from Figure

3.12 that the propagation length increases for the stress waves, when the generation beam is offset. This is to say, the stress waves consume more time to arrive at the probing surface. A forward shift in the ToF is thus noticed in Figure 3.13-a, for a 2 mm offset of generation laser beam. Hence, the magnitude of the displacement significantly decreases, because of enhanced attenuation. A similar trend can be noticed in Figure 3.13-b and 3.13-c. More information about the nature of stress waves can be found in [Scruby 1990].

3.7 Summary

A follow-up of the numerical study was carried out by conducting the experiments corresponding to the simulation. Two laminates were fabricated to validate the change in ToF experimentally. The ToF for the laminate without any inclusion compared favourably with the numerical study. The aluminium inclusion was used to create a delamination like feature. The results of this laminate however, were not similar to the numerical results. The reason for this significant variation is explained in the next chapter. Since the ToF of the laminates with 4 mm thickness were conclusive, an experimental investigation was hence carried out to verify the ToF on the laminates with different thickness. It was observed that, the displacement results were quite convincing with respect to ToF or time evolution for a 2 mm thick laminate. However, the magnitude of displacements in the subsequent time intervals for the through-transmission experiment, were in contradiction with the numerical study. It was presumed that, the reason for this contradiction is a marginal misalignment in two laser beam projections. Hence, an experimental investigation was carried out to study the effects of misalignment. Three offset values were considered and it was noticed that, as the offset increases, the magnitude of displacement decreases. This validates the ultrasound propagation theory that, the maximum amount of energy will be available in the region, which is directly under the impact spot.

CHAPTER 4. Analysis of experimental study

4.1 Introduction

The experimental investigations conducted in the previous chapter validated the theory of ToF, and complimented the numerical study. However, the experimental study of change in ToF due to a delamination was not successful. The aluminium inclusion used as a delamination like feature transmitted the stress waves instead of reflecting them. This chapter is devoted to understand the reason for this transmission. The numerical study will be carried out in both the through-transmission and pulse-echo set-ups, but on a scaled numerical model by resolving the velocities. Furthermore, effects of the dimensions of the delamination with respect to the spot diameter on the material behaviour will be studied.

4.2 Study of reflection of stress waves

This section deals with the understanding of the change of the properties needed, for a stress wave to reflect when the stress wave is passing an interface of two constituent media. Of all the properties, a high degree of impedance mismatch is necessary. With experimental and numerical studies, this shall be explained.

4.2.1 Mechanism of stress wave reflection

In Chapter 3, the experimental investigation of change in ToF from a laminate that has no delamination to a laminate that has an aluminium inclusion was done. The results are presented in Figures 3.6 and 3.7, for without and with delamination respectively, in through-transmission set-up. These results contradicted the numerical study. Similarly, the experiments were also conducted in the pulse-echo set-up and the results for the laminates without and with delamination are presented in Figures 3.8 and 3.10 respectively. This proved that the aluminium inclusion used to create a delamination like feature was not successful.

To understand the reason as to why the aluminium inclusion did not reflect the stress waves, the explanation in section 2.2 must be recalled. Briefly, when a stress wave is passing an interface the incident wave from the upstream medium is transmitted as a wave of the same nature in the downstream medium that is in contact. The stress wave is simultaneously reflected in the upstream medium and transmitted in the downstream medium, as a wave of relaxation or of shock/stress,

respectively. This phenomenon is dependent on the nature of the incident wave and the adjacent material impedance ratio. Hence, according to this theory, aluminium foil with an impedance of $Z_{Al} = 1.73.10^6$ g.cm^{-2}.s^{-1}, should have reflected the stress waves, when it is in contact with the CFRP composite ply whose impedance is: $Z_{CFRP} = 0.49.10^6$ g.cm^{-2}.s^{-1}. It is thus, very important to numerically study the reason for transmission of stress waves. In this study, the impedance mismatch would be derived for the inclusion materials, whose impedance value is higher than carbon/epoxy ply. This is done, because the creation of delamination like feature is easily possible during fabrication, with materials whose impedance value is higher than carbon/epoxy ply. With numerical study, it can be easily found out the minimum impedance mismatch necessary, when using a metal to create a delamination like feature.

4.2.2 Numerical study of effect of impedance mismatch

If the numerical results presented in Chapter 2 are carefully studied, it can be understood that the delamination created at any of the interplies, acts as an air gap or an in-service disbond. It is hence reasonable to infer that the stress waves fully reflect, and transmit the least amount of energy. This is due to the fact that, the impedance difference between the carbon/epoxy ply and air is significantly high, i.e., $Z_{CFRP} >> Z_{Air}$. The impedance ratio between the carbon/epoxy ply and air at 0° C deduces to Z_{CFRP} ($0.49.10^6$ g.cm^{-2}.s^{-1}) ≈ $11.5.Z_{Air}$ ($0.04286.10^6$ g.cm^{-2}.s^{-1}). In one of the research works, brass as an inclusion has been used to create a delamination like feature in a composite laminate. The inclusion of brass, as a delamination like feature, has been found to be successful [Pelivanov 2015]. This is because, the impedance of brass is much higher than that of aluminium, and is hence significantly higher than carbon/epoxy ply, i.e., Z_{Brass} ($4.06.10^6$ g.cm^{-2}.s^{-1}) > Z_{CFRP} ($0.49.10^6$ g.cm^{-2}.s^{-1}). Thus, a numerical study is carried out to understand the minimum impedance difference required between carbon/epoxy ply and an inclusion material, to study the effect of a delamination in CFRP composites. The numerical model and the loading parameters, which were used in section 2.5.3 of Chapter 2, are retained as it is. Several metallic inserts of size 2 mm X 0.01 mm are simulated, and the ratio of impedance difference required is derived. The size of the insert chosen in the numerical model was to keep the ratio of spot diameter to delamination length constant, because in the experimental investigation, the laser spot diameter for ultrasound generation was 1 mm and the aluminium foil was of 10 mm X 10 mm. The properties of the metal were assigned to a portion of mid-interply shown in Figure 4.1. Figure 4.2

compares the velocity results of a model without any delamination and a model that has aluminium as an inclusion for creating a delamination like feature.

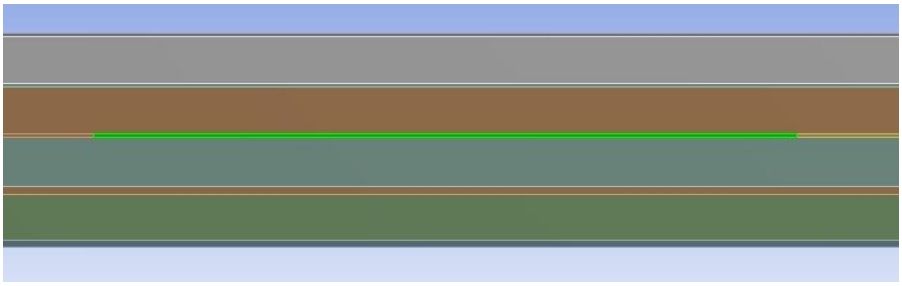

Figure 4.1: Portion (2 mm X 0.01 mm) of the middle interply considered for the assignment of properties of different inclusion materials.

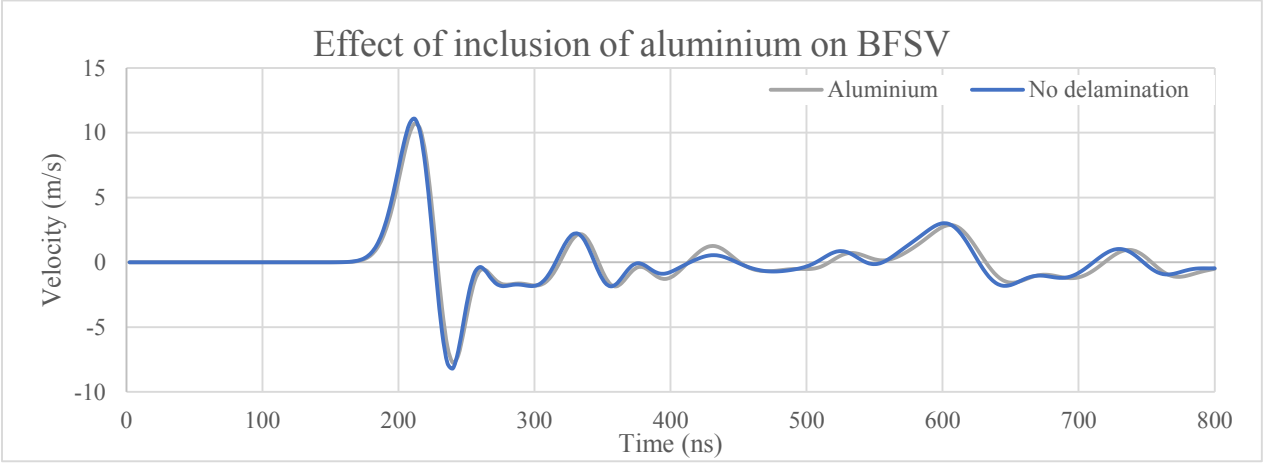

-a-

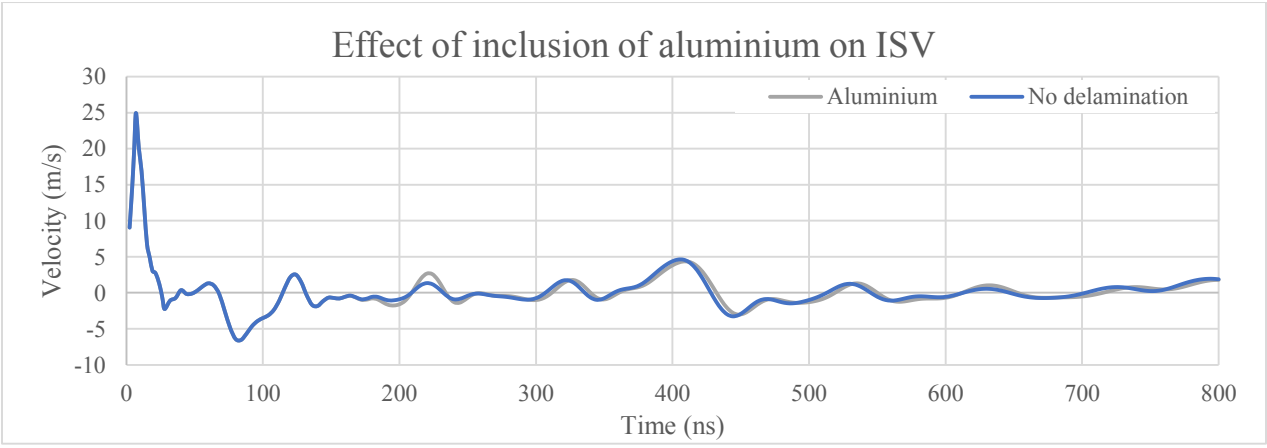

-b-

Figure 4.2: Comparison of results of models with and without an aluminium inclusion on, -a- BFSV, and -b- Impact Surface Velocity.

From Figure 4.2, it is easily understood that aluminium does not reflect stress waves, and that is the reason why, the experimental study of delamination was unsuccessful. Hence, it can be claimed that, aluminium must not be used as an inclusion to create a delamination like feature for the experimental studies in CFRP composites. Since, brass as an inclusion successfully replicated a delamination like feature [Pelivanov 2015]; a simulation of brass insert is carried out. Figure 4.3 presents the comparison of velocity results of a model without any delamination and a model that has brass as an inclusion.

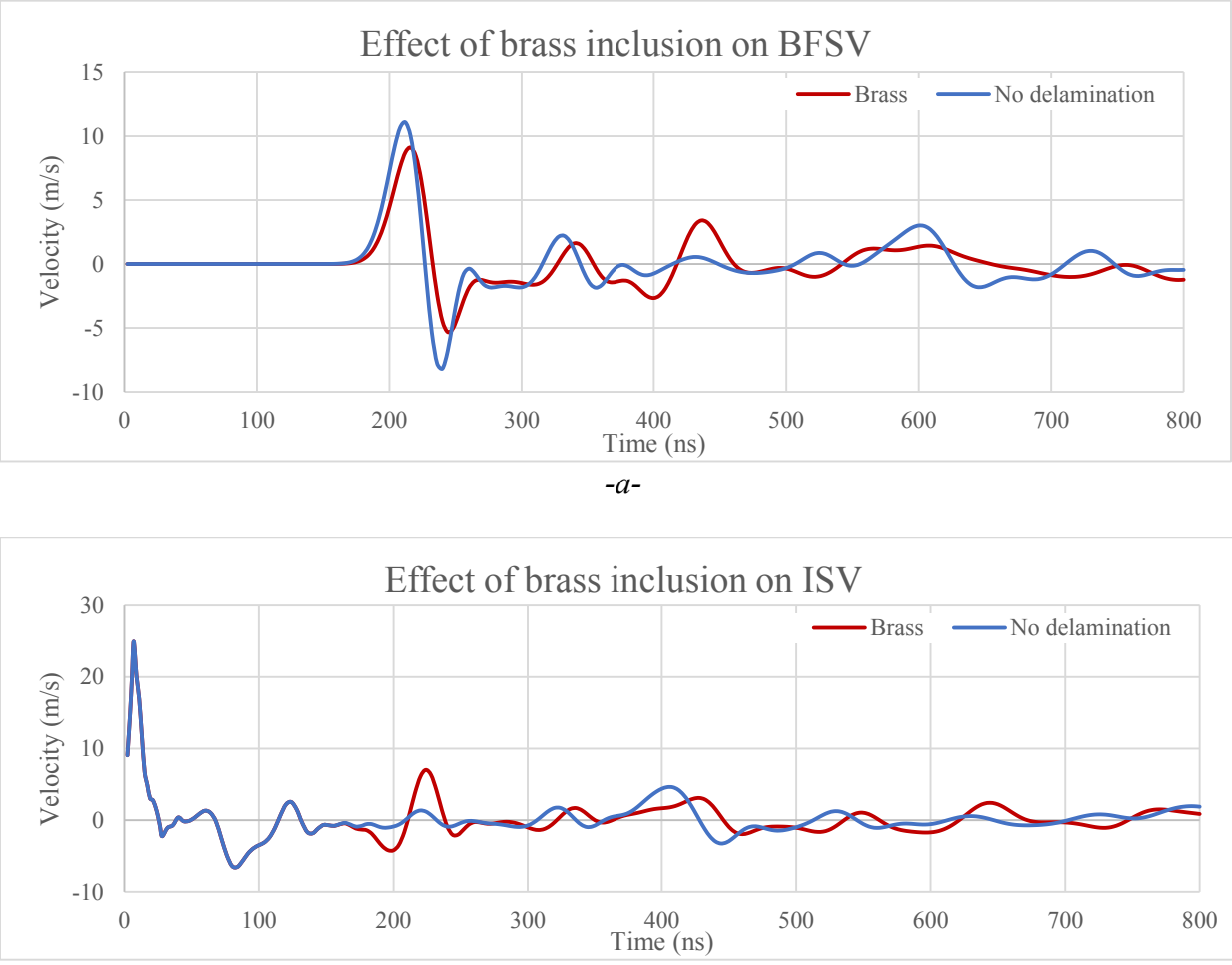

Figure 4.3: Comparison of results of models with and without a brass inclusion on, -a- BFSV, and -b- Impact Surface Velocity (ISV).

With brass as an insert a slight reduction in the magnitude of first compressive stress wave arriving at the back surface is noticed from Figure 4.3-a. Similarly, from Figure 4.3-b, a clear spike in the stress wave is visible at 224 ns. That means, the stress waves are reflected by the brass inclusion, and the probing point on the impact surface records arrival of a tensile stress wave. With an air

gap, the time evolution of the stress waves is seen to be close to 200 ns from Figure 2.23 for the pulse-echo set-up. However, because that the stress waves must propagate to and fro the thickness of the interply, a delay in the arrival time at the impact surface is the consequence. Apart from the propagation of stress wave, back and forth the thickness of interply, the change in the speed of sound in brass is also the reason for the change in ToF. Figure 4.4 presents the comparison of velocity results of a model without any delamination and a model that has an air gap. These results however were not obtained by substituting the properties of air at 0˚ C to the mid interply.

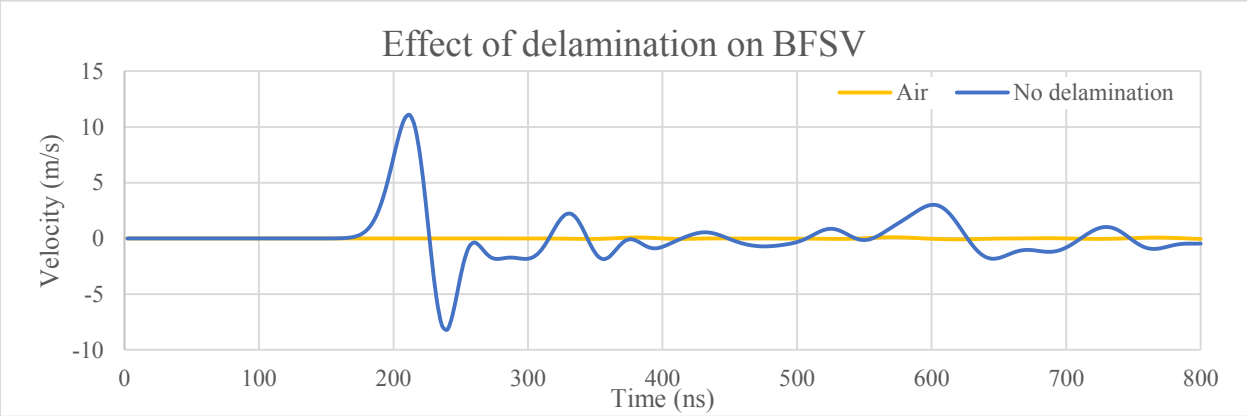

-a-

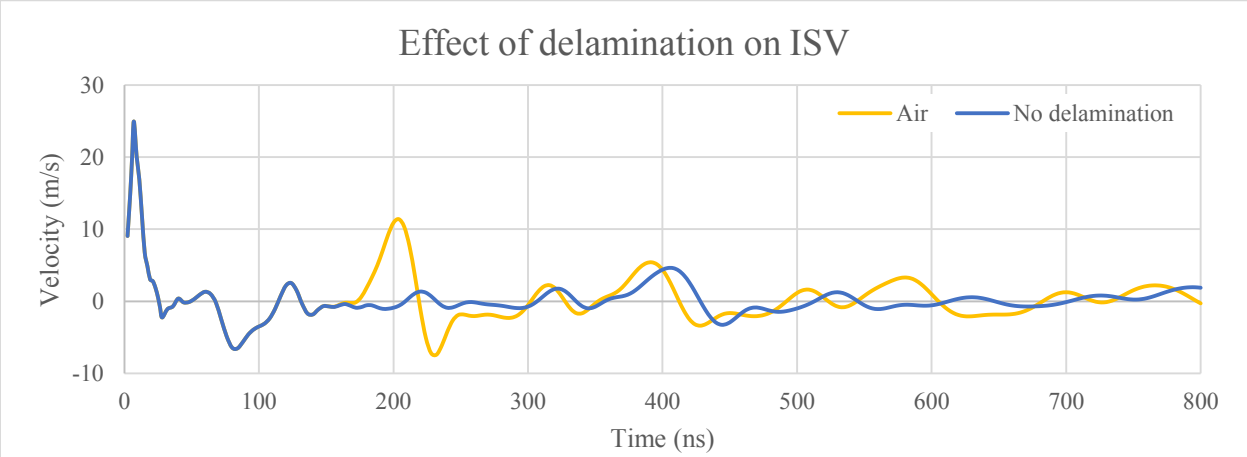

-b-

Figure 4.4: Comparison of results of models without delamination and with delamination on, -a- BFSV, and -b- Impact Surface Velocity (ISV).

With an air gap present, the ToF of the stress waves is seen to be close to 200 ns from Figure 4.4-b, however the magnitude of the velocity is less compared to the results in Figure 2.23. The reason for this is the size of the delamination, and the effects of size of s delamination for a spot diameter, on the behaviour of the material will be studied in section 4.2.

Now that, a change in ToF has been observed in the numerical study on a model with brass inclusion, a simulation of different insert metals, with varied impedance ratios must be carried out to identify the material with proper impedance ratio to replicate the airgap during experiments.

4.2.3 Numerical investigation of required impedance ratio

In this section, a comprehensive investigation of the impedance ratio of different inclusions on stress wave reflection will be done by means of simulation in a composite laminate. In the previous section, it was elaborated that a high degree of impedance mismatch is necessary for the inclusion material for a delamination like feature be created. This study is only useful to carry out the experiments to estimate the change in ToF due to discontinuity for the research purposes.

Two metallic materials were simulated as inserts in a 4-ply carbon/epoxy laminate in the previous section. It can be said that, the impedance ratio between aluminium and carbon/epoxy ply is approximately 3.5, i.e., $Z_{Al} = 3.5.Z_{CFRP}$. Similarly, impedance ratio between brass and carbon/epoxy ply is approximately 8, i.e., $Z_{Brass} = 8.Z_{CFRP}$. Therefore, it can be said that, for an impedance ratio of 8, the inclusion replicates a delamination like feature. Hence, all the metals with an impedance value of at least 8 times more than that of carbon/epoxy composite, would replicate a delamination like feature. However, minimum impedance ratio needed for a material to be used as an inclusion needs to be identified. Impedance ratios between different inclusion materials and carbon/epoxy ply are presented in Table 4.1.

Material	*Impedance, Z ($g.cm^{-2}.s^{-1}$)*	*Impedance ratio (approx.)*
aluminium	$1.73.10^6$	3.5
beryllium	$2.41.10^6$	5
germanium	$2.96.10^6$	6
brass	$4.06.10^6$	8
copper	$4.46.10^6$	9
platinum	$6.98.10^6$	14
tungsten	$10.1.10^6$	20
air (at 0˚ C)	$0.04286.10^6$	0.087

Table 4.1: Impedance values of different inclusion materials and their impedance ratios with carbon/epoxy ply.

Figure 4.5 presents the comparison of velocity results of a model without any delamination, a model with the air delamination, and models with different metallic inclusions listed in Table 4.1.

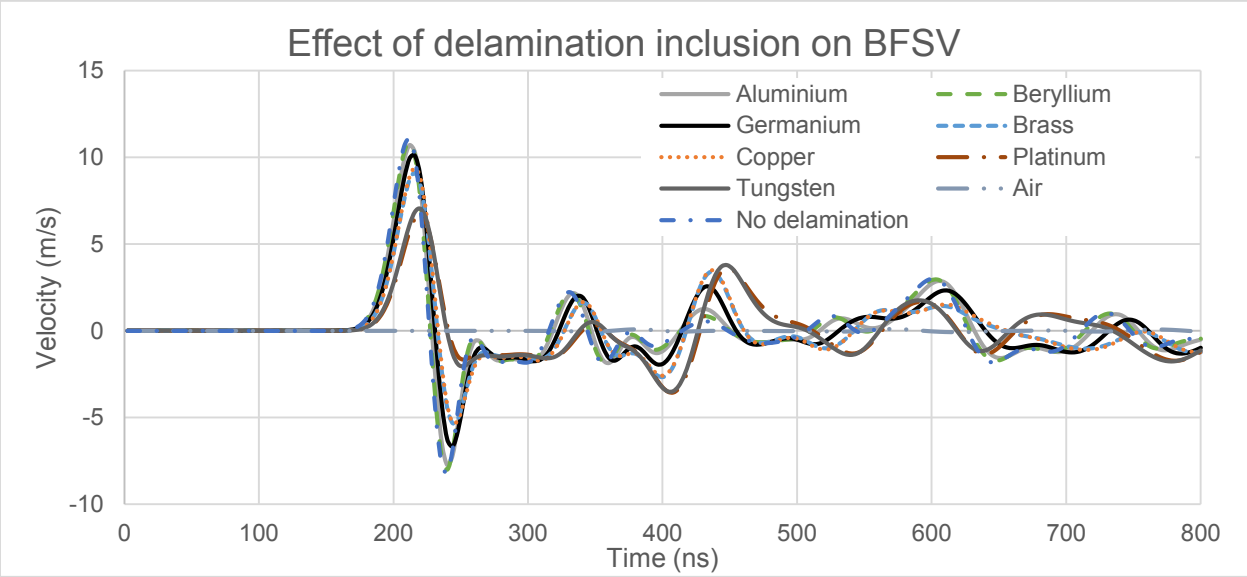

-a-

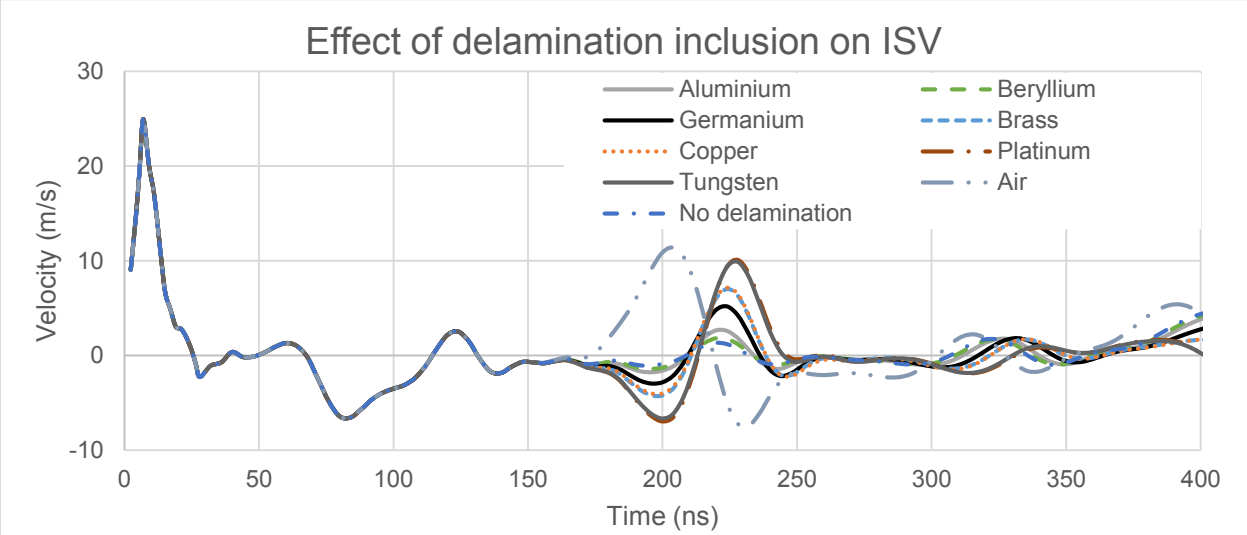

-b-

Figure 4.5: Comparison of velocity results using different inclusion materials, -a- BFSV, and -b- Impact Surface Velocity (ISV).

The From Figures 4.5-a and 4.5-b, it is can be seen that the stress waves were not reflected by the beryllium inclusion. Hence, an impedance ratio of 5, between the inclusion material and carbon/epoxy ply, is not sufficient to reflect the stress waves. Additionally, the velocity results of the numerical model with a beryllium inclusion is very much similar to the velocity results of the

numerical model with an aluminium inclusion. With germanium as an inclusion material, to create a delamination like feature, a marginal reduction in the magnitude of first compressive wave is seen in Figure 4.5-a. A reflection of stress waves does occur, and the probe point records the tensile stress wave arriving at 224 ns, which can be observed in Figure 4.5-b. Hence, it can be said that, the impedance ratio, between the inclusion material and carbon/epoxy ply, must be at least 6, such that the inclusion material replicates a delamination like feature. It is observed that, the velocity profiles in both the set-ups of a model with copper inclusion is very similar to the velocity profiles of a model with brass inclusion. This is expected, because the impedance ratios that these two materials make with respect to the carbon/epoxy ply, are very close, and are given in Table 4.1. For the platinum ($Z_{platinum}$ = $6.98.10^6$ $g.cm^{-2}.s^{-1}$) and tungsten ($Z_{tungsten}$ = $10.1.10^6$ $g.cm^{-2}.s^{-1}$) inclusions, the nature of stress wave propagation changes remarkably, where the magnitude of the first compressive wave has reduced by 50%. In similar fashion, from Figure 4.5-b, it is noticed that the magnitude of the first tensile stress wave almost equals the magnitude of stress wave of a model with an air gap. However, the ToF has delayed, and it is due to the change in the properties of the inclusion material. Another reason for the delay in ToF is that, the stress waves need to travel back and forth the thickness of the interply, where the inclusion is located.

Since, there are many metals or other materials that can be used based on availability, it is thus very important to know the dependence of the individual parameters on the stress wave reflection. The parameters that constitute the impedance value are, material density and speed of sound wave, as narrated in section 1.5.1.2. The properties of carbon/epoxy plies and epoxy interplies are given in Table 2.8. From Table 2.8, the density of the carbon/epoxy ply is 1630 $kg.m^{-3}$, and the density of beryllium is found to be 1870 $kg.m^{-3}$. These two density values are very close to each other. However, the speed of sound wave in beryllium (12890 $m.s^{-1}$) is much higher than carbon/epoxy ply (3000 $m.s^{-1}$). Thus, making the impedance of beryllium almost 5 times the impedance of carbon/epoxy ply. However, the stress waves did not reflect, when beryllium was used as an inclusion material. It can hence be said that, the reflection of stress waves is independent of minimal mismatch in the density values of the two constituent media. Likewise, from Table 2.8, the speed of sound wave in carbon/epoxy ply is 3000 $m.s^{-1}$, and the speed of sound wave in platinum is found to be 3260 $m.s^{-1}$. These two sound wave speed values are very close to each other. However, the density of platinum (21400 $kg.m^{-3}$) is higher than carbon/epoxy ply (1630 $kg.m^{-3}$). Thus, making the impedance of platinum almost 14 times the impedance of carbon/epoxy

ply. This high impedance ratio has ensured the reflection of waves, and it can hence be said that, the reflection of stress waves is again independent of minimal mismatch in the speed of sound wave values, of the two constituent media. It can hence be concluded that, the absolute value of impedance is important to note, when it comes to replicating a delamination like feature by an inclusion material.

4.2.4 Summary of numerical study on effect of inclusion materials

In this section, a summary of the simulation results is posited. Table 4.2 gives the impedance ratios between different materials and the percentage of change in the velocity magnitudes in both the through-transmission and pulse-echo set-ups.

For through-transmission set-up, the velocity magnitude of the first compressive stress wave should decrease. Whereas, for the pulse-echo set-up, the tensile stress wave velocity magnitude, arriving at the probing point post the reflection of stress waves, should increase. In other words, the velocity values should be as close as possible to the values that can be attained, when there is an air gap.

Material	Impedance ratio (approx.)	Velocity (through-transmission) ($m.s^{-1}$)	% change w.r.t. result in no delamination (11.076 $m.s^{-1}$)	Velocity (pulse-echo) ($m.s^{-1}$)	% change w.r.t. result in no delamination (1.35 $m.s^{-1}$)
aluminium	3.5	10.717	3.24 %	2.6	48.07 %
beryllium	5	10.886	1.71 %	1.83	26.3 %
germanium	6	10.084	8.9 %	5.18	73.9 %
brass	8	9.1064	17.78 %	7.02	80.76 %
copper	9	9.3971	15.16 %	7.16	81.14 %
platinum	14	6.7081	39.43 %	10.039	86.55 %
tungsten	20	7.0397	36.44 %	9.87	86.32 %
air (at 0˚ C)	0.087	0.0866	99.21 %	11.39	88.65 %

Table 4.2: Variation in the velocity magnitudes of the numerical model with different inclusion materials, simulated in both the set-ups.

Air as a delamination can further be altered in size, to note the effects of delamination size on the material behaviour for a fixed spot diameter. A numerical study is carried out in this regard, and is discussed in the next section.

4.3 Effect of size of delamination on material behaviour

In the previous section, the numerical study consisted of pressure loading with an impact spot diameter of 200 µm. The size of delamination in 2D environment is adjusted to 2 mm X 0.01 mm. These dimensions were used to scale down the sizes of aluminium foil with respect to spot diameter, to simulate faster. However, in section 2.5.3, the size of delamination replicating an air gap was 250 µm X 10 µm. This study included an understanding of ToF based on the depth of delamination, i.e., delamination at different interplies. To study the effects of change in size of the delamination, the dimensions of delamination (250 µm X 10 µm) will be altered. Section 4.3.1 deals with the study of decrease in the size of the delamination to 100 µm X 10 µm, on material behaviour. Similarly, section 4.3.2 discusses the effects of an increase in the size of delamination on the material behaviour, when the size is increased to 400 µm X 10 µm. The simulation results for a delamination size of 250 µm X 10 µm, have been presented here again in Figure 4.6, for both the set-ups.

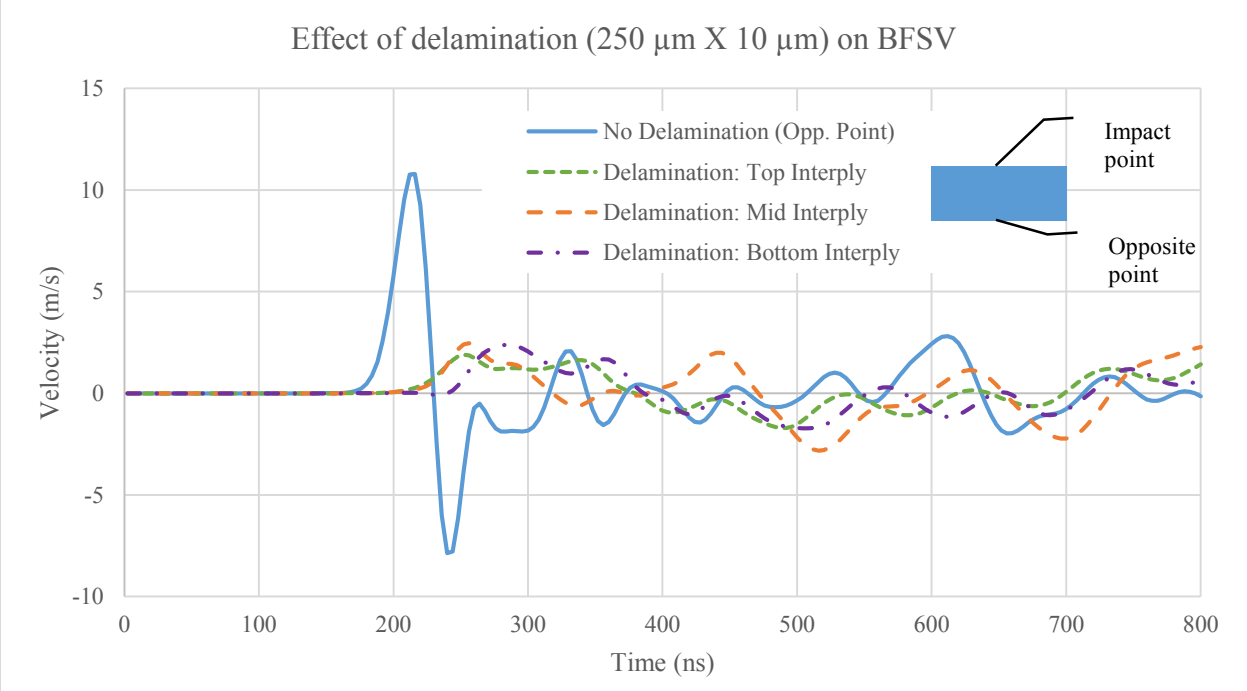

-a-

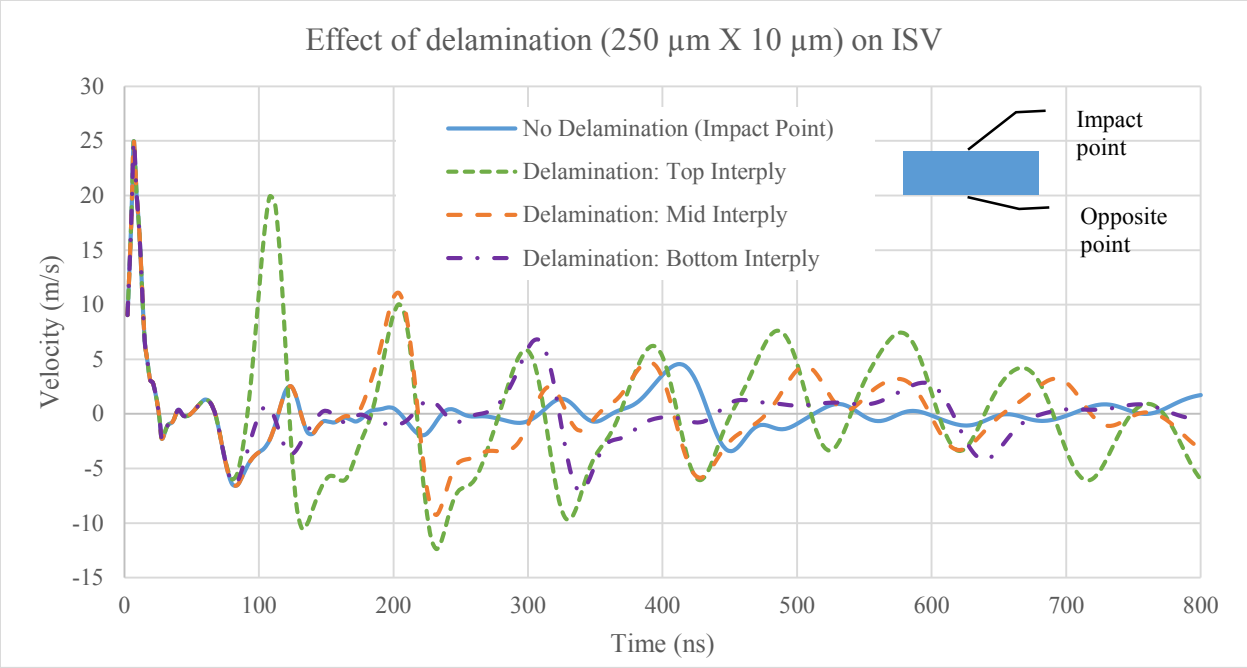

-b-

Figure 4.6: Effect of delamination of size 250 µm X 10 µm for an impact spot diameter of 200 µm on material behaviour for, -a- BFSV (through-transmission set-up), -b- ISV (pulse-echo set-up).

The ToF of stress waves and associated velocity magnitudes for the model with delamination size of 250 µm X 10 µm in pulse-echo set-up (Figure 4.6-b) are given in Table 4.3.

Location of delamination	ToF/time evolution (first wave) (ns)	Velocity magnitude (first wave) ($m.s^{-1}$)
Top interply	108	19.923
Middle interply	204	11.084
Bottom interply	308	6.781

Table 4.3: ToF and velocity magnitudes of stress waves at various depths of delamination of size 250 µm X 10 µm.

For the delamination at bottom interply, the velocity peak is measured close to 308 ns at a magnitude of 6.781 $m.s^{-1}$. The reason for the variation in the ToF of this stress wave is due to the variation in the thickness of ply above the bottom interply, which can be seen in Figure 2.24. With the numerical study, the ToF of stress waves has been found to be the key aspect in distinguishing the depth of delamination using laser ultrasound NDE technique. This ToF can be calculated by dividing the distance or propagation in the thickness direction of the laminate with sound wave velocity estimated using equation (1.10).

4.3.1 Effects of decreased delamination size on material behaviour

The delamination size is decreased to 100 µm X 10 µm, i.e., half of spot diameter (200 µm). The simulation results for this size of delamination have been presented in Figure 4.7, for both the set-ups.

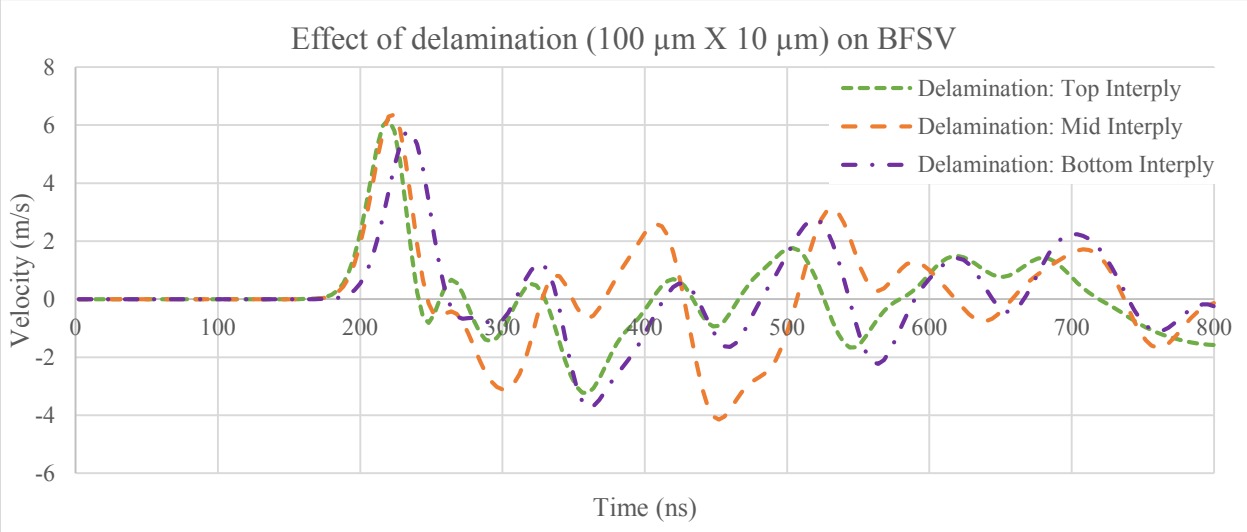

-a-

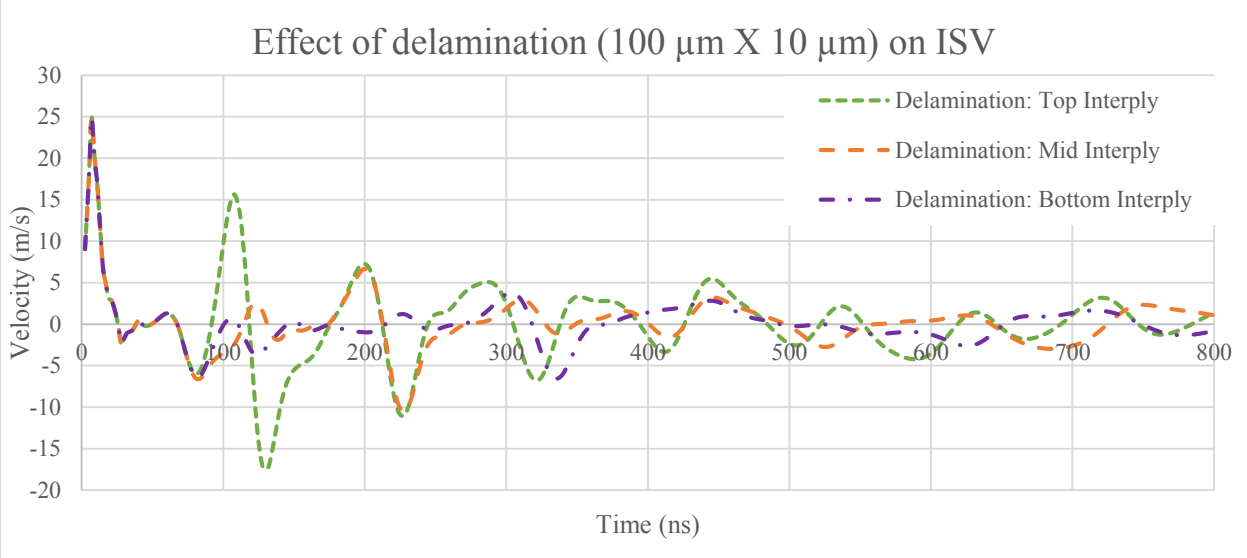

-b-

Figure 4.7: Effect of delamination of size 100 µm X 10 µm for an impact spot diameter of 200 µm on material behaviour for, -a- BFSV (through-transmission set-up), -b- ISV (pulse-echo set-up).

The ToF of stress waves and associated velocity magnitudes for the model with delamination size of 100 µm X 10 µm in pulse-echo set-up (Figure 4.7-b) are given in Table 4.4.

Location of delamination	ToF/time evolution (first wave) (ns)	Velocity magnitude (first wave) ($m.s^{-1}$)
Top interply	108	15.641
Middle interply	200	6.671
Bottom interply	304	3.804

Table 4.4: ToF and velocity magnitudes of stress waves at various depths of delamination of size 100 µm X 10 µm.

From the ToF and velocities mentioned in Tables 4.3 and 4.4, it can be noticed that the ToF values are very close. However, the magnitudes of velocities have decreased with the decrease in size of delamination. When the spot diameter is larger than the size of the delamination, not all the stress waves are reflected off the surface of discontinuity. Only those stress waves whose propagation is interrupted tend to reflect, and other stress waves continue to propagate. Thus, only a partial amount of energy is available in the stress waves arriving at the probing end on impact surface. This results in lower magnitudes of resolved velocities.

Another aspect of reduction in velocity magnitudes could be the broadband nature of stress wave propagation. This phenomenon is more pronounced in the velocity profile at the bottom interply (refer to Figure 4.7-b). Thus, the reduction in the velocity magnitude of the stress wave reflected off the delamination at bottom interply, arriving at the impact surface, is significantly reduced.

4.3.2 Effects of increased delamination size on material behaviour

Similarly, the delamination size is increased to 400 µm X 10 µm, i.e., twice the spot diameter (200 µm). The simulation results for this size of delamination have been presented in Figure 4.8, for both the set-ups.

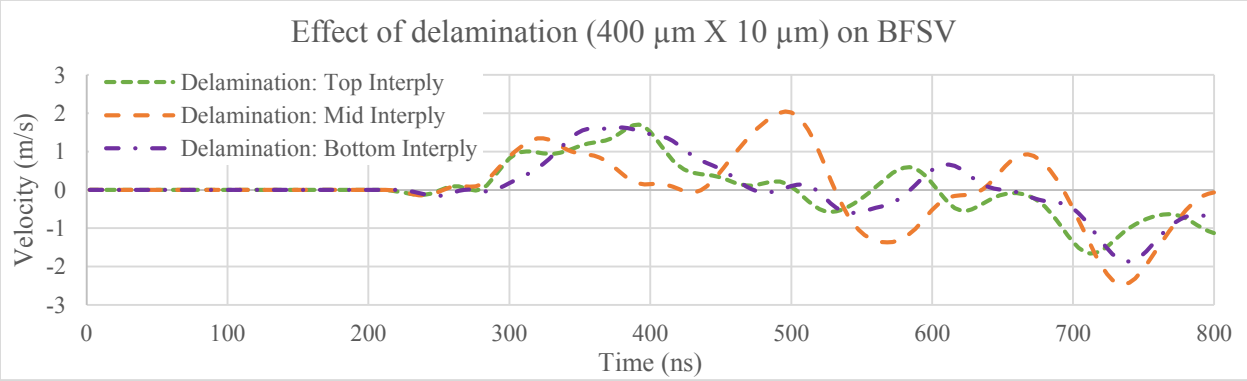

-a-

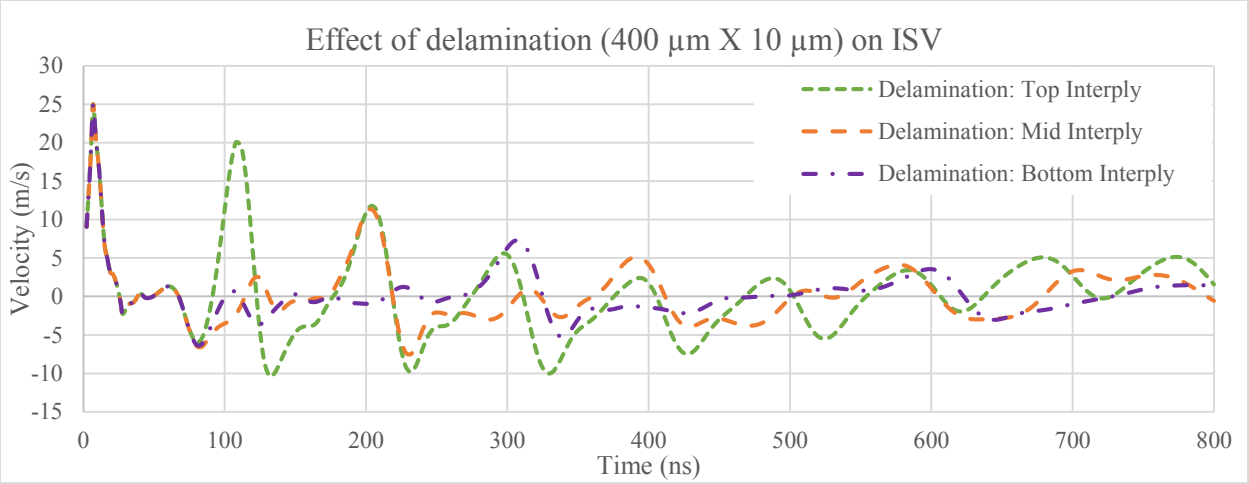

-b-

Figure 4.8: Effect of delamination of size 400 µm X 10 µm for an impact spot diameter of 200 µm on material behaviour for, -a- BFSV (through-transmission set-up), -b- ISV (pulse-echo set-up).

The ToF of stress waves and associated velocity magnitudes for the model with delamination size of 400 µm X 10 µm in pulse-echo set-up (Figure 4.8-b) are given in Table 4.5.

Location of delamination	ToF/time evolution (first wave) (ns)	Velocity magnitude (first wave) ($m.s^{-1}$)
Top interply	108	20.027
Middle interply	204	11.335
Bottom interply	308	7.303

Table 4.5: ToF and velocity magnitudes of stress waves at various depths of delamination of size 400 µm X 10 µm.

From the ToF and velocities mentioned in Tables 4.3 and 4.5, it can be seen that, both the ToF and velocity magnitudes are very close, for ISV. However, the magnitudes of BFSV velocities has significantly reduced, and the ToF has shifted forward (refer to Figure 4.8-a). Thus, it can be said that, the stress waves possess significant energy, propagating above the delamination. This results in much intense reverberation of the subsequent velocity magnitudes, of the stress waves arriving at the probe point, which is observed in Figure 4.8-b.

4.4 Summary

To understand the reason for transmission of stress waves, a numerical simulation was carried out with aluminium as an inclusion material. It was found out that, an impedance ratio of 3.5, between a material and carbon/epoxy ply, is insufficient to create a delamination like feature. Further

simulations were carried out using materials with different impedance ratios and it was concluded that an impedance mismatch of at least 6 between the material and the composite is required for successful replication of the delamination.

Lastly, the size of delamination was altered with respect to the spot diameter and simulated to understand the effects of delamination size on stress wave propagation. It was found that the ToF remains the same, but a proportional change in the velocity magnitudes is noticed. However, the reason for any disproportionate change in velocity magnitude was attributed to the broadband nature of the stress wave propagation.

CHAPTER 5. General conclusion and future outlook

In this thesis, the feasibility study has been successfully carried out to understand the applicability of using a high repetition rate laser for NDE. It can be said that, these low cost lasers have the potential to examine the structures. To achieve this, a numerical model that posits the results based on the laser-matter interaction has been developed, followed by validating the model with experimental and numerical studies from literature for isotropic materials. A numerical model has been validated for multi-layered composites, by taking into account the prime factors from the literature. A feasibility study for a high repetition rate and low energy laser has been conducted, to understand its applicability for the NDE of structures, such that the technology can be at the disposal of many industries and research enthusiasts. The numerical study was then extended to understand the change(s) in ToF, and the presence and depth of a delamination has been quantified, for the loading parameters of a high repetition rate and low energy laser. Experiments were conducted on carbon/epoxy composite laminates, and a correlation of between the numerical and experimental study concerning the behaviour of laminated composites subjected to a laser impact has been derived.

5.1 Main outcomes of this work

- The flaws and their effects in the representative carbon/epoxy composite laminate for the aerospace application are studied. The existing flaw detection methods were briefly described, and the problems that persist in these techniques were depicted. The potential of laser ultrasound NDE to overcome the problems with the existing methods to detect the flaws has been explained, with theoretical and phenomenological backing of the laser impact. An introduction to the optical ultrasound detection systems was discussed.
- The mechanism of stress wave propagation is illustrated, wherein the role of impedance is explained. A re-work of simulation of selected publications were carried out to validate the model for both metals and composites. This validation of numerical models was done, such that the model is capable of positing the results relative to the ultrasound generation and detection.
- Multiple models were compared to know the optimal design of the numerical model for the study of stress wave propagation. Within the same composite model, delamination at different interplies were introduced to attain the results and analyse the changes. This study has enabled

a successful execution of NDE in the industrial contexts using lasers with respect to the experimental set-up, i.e., through-transmission and pulse-echo configurations. The simulation was further extended to study the feasibility of using a high repetition rate and low energy laser for the NDE of materials. With this study, it was understood that, these lasers can be used for the NDE, however an experimental study must be carried out. The numerical model was homogenised in the zone where the stress waves do not propagate in order to reduce the computation time, and the results were comparable with the model without any homogenised zone. With the homogenised outer zone model, computation time was reduced by 33%. In addition, simulation results can be beneficial in selecting the tools based on the resolving capacity and velocity/displacement decoding limits.

- Experimental results for the laminates with and without delamination were presented, which was conducted in two experimental set-ups. A delamination like feature was created using an aluminium inclusion. The characterization of depth of delamination was inconclusive with aluminium inclusion, in both the experimental set-ups. However, the experimental study of ToF of, laminates without any delamination complements the numerical study. This study was done on a laminate with different thickness also. The results in the through-transmission set-up did not match with the numerical study, leading to the study of misalignment of laser beams. It was found that, there is an immense reduction in the magnitude of stress wave, should there be a misalignment of even 2 mm, for the spot diameters of 1 mm.
- An analysis was carried out to study the effect of impedance mismatch on the stress wave propagation. Many inclusion materials were considered for the simulation with the impedance ratio ranging from 3.5 (aluminium) to 20 (tungsten) between the inclusion material and the carbon/epoxy ply. It was observed that, for a material to act like a delamination, an impedance ratio of at least 6 is required. The inclusion materials such as, platinum and tungsten would closely replicate an air gap, in the pulse-echo set-up. Lastly, the effect of variation of delamination sizes on the nature of stress wave propagation and the material behaviour was done.

The potential of the technique and the relevance of the associated industrial tools have been demonstrated to conduct NDE of different materials successfully.

5.2 Future research directions

The experimental investigation of applicability of high repetition rate and low energy laser for the laser ultrasound NDE must be conducted.

In addition to that, some of the follow-up research that can be carried out is narrated below:

- A numerical study involving a 3D model, with the local microstructure, and lay-up of plies of different fibre orientation, can be carried out. A simulation of 3D composites can also be done, to comprehend the stress propagation. An ambitious study would be of simulating the stress wave propagation in a model that is bent at an angle during fabrication, e.g., an angle bar made of composites.
- The broadband nature of stress waves can be understood by simulating a 3D model, to derive a precise relation between the material properties and laser parameters.
- The simulation can also be carried out for studying the effects of other types of flaws on the behaviour of composite laminate. These flaws may include, porosity, resin rich areas, dry spots etc.
- An experimental study to test the efficiency and robustness of the lasers for NDE, can be carried out on angle bars, an examination that is very difficult with the conventional tools.
- A research can be conducted to incorporate an actual delamination (an air-gap or a patch in vacuum), in the multi-layered materials, such that experimental investigations and results can be more realistic.
- A database can be created through a series of experiments on laminates with varied percentage of porosity, resin rich areas, and dry spots, and the results can be compared with the results obtained using conventional tools.
- Undertaking and completion of all the above tasks can benefit in assuring the adaptability of this novel technique in numerous industries.

References

[Abrate 2005] Abrate, Serge. *Impact on composite structures*. Cambridge university press, (2005).

[Adams 1988] Adams, R. D., and P. D. R. D. Cawley. "A review of defect types and nondestructive testing techniques for composites and bonded joints." *NDT international,* vol. 21, no. 4 (1988).

[Ahn 2013] Ahn, Phillip, Zhen Zhang, Cheng Sun, and Oluwaseyi Balogun. "Optical detection of ultrasound using an apertureless near-field scanning optical microscopy system." In *Review of Progress in Quantitative Nondestructive Evaluation: Volume 32*, vol. 1511, no. 1, pp. 360-366. AIP Publishing, 2013.

[Antonelli 2002] Antonelli, G. Andrew, Humphrey J. Maris, Sandra G. Malhotra, and James ME Harper. "Picosecond ultrasonics study of the vibrational modes of a nanostructure." *Journal of applied physics* vol. 91, no. 5 (2002).

[Armstrong 2005] Armstrong, Keith B., L. Graham Bevan, and William F. Cole. *Care and repair of advanced composites*. Society of Automotive Engineers, (2005).

[Arrigoni 2006 a] Arrigoni, M., M. Boustie, C. Bolis, L. Berthe, Sophie Barradas, and Michel Jeandin. "Evolutions of the LASer Adhesion Test (LASAT) for the debonding of coatings on substrates above the millimeter range thickness." In *Journal de Physique IV (Proceedings)*, EDP sciences, vol. 134 (2006).

[Arrigoni 2006 b] Arrigoni, M., Sophie Barradas, M. Braccini, M. Dupeux, Michel Jeandin, M. Boustie, C. Bolis, and L. Berthe. "A comparative study of three adhesion tests (EN 582, similar to ASTM C633, LASAT (LASer Adhesion Test), and bulge and blister test) performed on plasma sprayed copper deposited on aluminium 2017 substrates." *Journal of adhesion science and technology* vol. 20, no. 5 (2006).

[Arrigoni 2008 a] Arrigoni, Michel, Silvio Krüger, Alain Blouin, Daniel Lévesque, Bernard Arsenault, Jean-Pierre Monchalin, M. Boustie, and L. Berthe. "Adhesive bond testing by laser induced shock waves." In *17th World Conference on Nondestructive Testing,* (2008).

[Arrigoni 2008 b] Arrigoni, Michel, J. P. Monchalin, A. Blouin, S. E. Kruger, and M. Lord. "Laser Doppler interferometer based on a solid Fabry–Perot etalon for measurement of surface velocity in shock experiments." *Measurement science and technology* vol. 20, no. 1 (2008).

[Asay 2012] Asay, James R., and Mohsen Shahinpoor, eds. *High-pressure shock compression of solids*. Springer Science & Business Media, 2012.

[Askar'yan 1963] Askar'yan, G. A., and E. M. Moroz. "Pressure on evaporation of matter in a radiation beam." *Soviet Journal of Experimental and Theoretical Physics* vol. 16 (1963).

[Barker 1972] Barker, L. M., and R. E. Hollenbach. "Laser interferometer for measuring high velocities of any reflecting surface." *Journal of Applied Physics* vol. 43, no. 11 (1972).

[Berthe 1997] Berthe, L., R. Fabbro, P. Peyre, L. Tollier, and E. Bartnicki. "Shock waves from a water-confined laser-generated plasma." *Journal of Applied Physics* vol. 82, no. 6 (1997).

[Bolis 2007] Bolis, C., Laurent Berthe, M. Boustie, M. Arrigoni, Sophie Barradas, and Michel Jeandin. "Physical approach to adhesion testing using laser-driven shock waves." *Journal of Physics D: Applied Physics* vol. 40, no. 10 (2007).

[Boustie 1991 b] Boustie, M., and F. Cottet. "Experimental and numerical study of laser induced spallation into aluminum and copper targets." *Journal of applied physics* vol. 69, no. 11 (1991).

[Brenner 2007] Brenner, David J., and Eric J. Hall. "Computed tomography—an increasing source of radiation exposure." *New England Journal of Medicine* vol. 357, no. 22 (2007).

[Cottet 1988] Cottet, F., A. Ng, L. Da Silva, and L. Marty. "Spallation under the action of a laser induced shock wave." *Le Journal de Physique Colloques* vol. 49, no. C3 (1988).

[Davison 2012] Davison, Lee, Dennis E. Grady, and Mohsen Shahinpoor, eds. *High-pressure shock compression of solids II: dynamic fracture and fragmentation*. Springer Science & Business Media, (2012).

[Davy 1988] Davy, Pamela J., and Felicity J. Guild. "The distribution of interparticle distance and its application in finite-element modelling of composite materials." In *Proceedings of the Royal Society of London A: Mathematical, Physical and Engineering Sciences*, The Royal Society, vol. 418, no. 1854 (1988).

[De Rességuier 2005] De Rességuier, T., P. Berterretche, and M. Hallouin. "Influence of quartz anisotropy on shock propagation and spall damage." *International journal of impact engineering* vol. 31, no. 5 (2005).

[Delaye 1995 a] Delaye, Philippe, Alain Blouin, Denis Drolet, and Jean-Pierre Monchalin. "Heterodyne detection of ultrasound from rough surfaces using a double phase conjugate mirror." *Applied physics letters* vol. 67, no. 22 (1995).

[Delaye 1995 b] Delaye, Ph, Louis-Anne De Montmorillon, and Gérald Roosen. "Transmission of time modulated optical signals through an absorbing photorefractive crystal." *Optics Communications* vol. 118, no. 1 (1995).

[Devaux 1993] Devaux, D., R. Fabbro, L. Tollier, and E. Bartnicki. "Generation of shock waves by laser-induced plasma in confined geometry." *Journal of Applied Physics* vol. 74, no. 4 (1993).

[Dewhurst 1999] Dewhurst, Richard J., and Qing Shan. "Optical remote measurement of ultrasound." *Measurement Science and Technology* vol. 10, no. 11 (1999).

[Dhulkhed 2016] Dhulkhed, Shyam, and Sivakumar Narayanswamy. "ANSYS simulation as a feasibility study for high repetition laser ultrasonic non-destructive evaluation (NDE)." In *Photonics North (PN), 2016*, IEEE, (2016).

[Ecault 2013] Ecault, R., M. Boustie, L. Berthe, F. Touchard, H. Voillaume, B. Campagne, and D. Loison. "Development of a laser shock wave adhesion test for the detection of weak composite bonds." In *5th International Symposium on NDT in Aerospace*, (2013).

[Eliezer 1990] Eliezer, Shalom, Irith Gilath, and Tuvia Bar-Noy. "Laser-induced spall in metals: Experiment and simulation." *Journal of applied physics* vol. 67, no. 2 (1990).

[Erhard 2006] Erhard, Gunter, and Martin Thompson. *Designing with plastics*. Munich, Germany: Hanser, (2006).

[Fabbro 1990] Fabbro, R., J. Fournier, P. Ballard, D. Devaux, and J. Virmont. "Physical study of laser-produced plasma in confined geometry." *Journal of applied physics* vol. 68, no. 2 (1990).

[Fox 1974] Fox, Jay A. "Effect of water and paint coatings on laser-irradiated targets." *Applied Physics Letters* vol. 24, no. 10 (1974).

[Garnier 2011] Garnier, Christian, Marie-Laetitia Pastor, Florent Eyma, and Bernard Lorrain. "The detection of aeronautical defects in situ on composite structures using Non Destructive Testing." *Composite structures* vol. 93, no. 5 (2011).

[Gay 2011] Gay, Elise. "Comportement de composites sous choc induit par laser: développement de l'essai d'adhérence par choc des assemblages de composites collés." PhD diss., Ecole nationale supérieure d'arts et métiers-ENSAM, (2011).

[Gay 2014 a] Gay, Elise, Laurent Berthe, Michel Boustie, Michel Arrigoni, and Marion Trombini. "Study of the response of CFRP composite laminates to a laser-induced shock." *Composites Part B: Engineering* vol. 64 (2014).

[Gay 2014 b] Gay, Elise, Laurent Berthe, Michel Boustie, Michel Arrigoni, and Eric Buzaud. "Effects of the shock duration on the response of CFRP composite laminates." *Journal of Physics D: Applied Physics* vol. 47, no. 45 (2014).

[Gilath 1989] Gilath, I., S. Eliezer, and H. Weisshaus. "Damage in 2D carbon-carbon composites by short pulsed laser induced shock waves." *Journal of reinforced plastics and composites* vol. 8, no. 3 (1989).

[Grahn 1989] Grahn, Holger T., Humphrey J. Maris, and Jan Tauc. "Picosecond ultrasonics." *IEEE Journal of Quantum Electronics* vol. 25 (1989).

[Grun 1981] Grun, J., R. Decoste, B. H. Ripin, and J. Gardner. "Characteristics of ablation plasma from planar, laser-driven targets." *Applied Physics Letters* vol. 39, no. 7 (1981).

[Guild 1989 a] Guild, F. J., and R. J. Young. "A predictive model for particulate-filled composite materials." *Journal of materials science* vol. 24, no. 1 (1989).

[Guild 1989 b] Guild, F. J., P. J. Davy, and P. J. Hogg. "A model for unidirectional composites in longitudinal tension and compression." *Composites science and technology* vol. 36, no. 1 (1989).

[Gupta 1990] Gupta, V., and A. S. Argon. "Measurement of Interface Strength by Laser Pulse Induced Spallation." In *MRS Proceedings*, Cambridge University Press, vol. 188 (1990).

[Gupta 1993 a] Gupta, V., and J. Yuan. "Measurement of interface strength by the modified laser spallation technique. II. Applications to metal/ceramic interfaces." *Journal of Applied Physics* vol. 74, no. 4 (1993).

[Gupta 1993 b] Gupta, Vijay, Jun Yuan, and Doris Martinez. "Calculation, measurement, and control of interface strength in composites." *Journal of the American Ceramic Society* vol. 76, no. 2 (1993).

[Harrach 1982] Harrach, R. J., Y. T. Lee, R. J. Trainor, N. C. Holmes, M. D. Rosen, D. L. Banner, and R. J. Olness. "Contrasts in one-and two-dimensional hydrocode calculations of laser-generated shockwaves in disk targets." In *Shock Waves in Condensed Matter-1981*, AIP Publishing, vol. 78, no. 1 (1982).

[Hernández-Valle 2013] Hernández-Valle, F., Rachel S. Edwards, A. R. Clough, M. H. Rosli, and Ben Dutton. "Laser generation and detection for surface wave interaction with different defect geometries." In *Review of Progress in Quantitative Nondestructive Evaluation: Volume 32*, AIP Publishing, vol. 1511, no. 1, (2013).

[Hoa 2009] Hoa, Suong V. *Principles of the manufacturing of composite materials*. DEStech Publications, Inc., (2009).

[Hung 2009] Hung, Y. Y., Yun Shen Chen, S. P. Ng, L. Liu, Y. H. Huang, B. L. Luk, R. W. L. Ip, C. M. L. Wu, and P. S. Chung. "Review and comparison of shearography and active thermography for nondestructive evaluation."*Materials Science and Engineering: R: Reports* vol. 64, no. 5 (2009): 73-112.

[Ing 1991] Ing, R. K., and J-P. Monchalin. "Broadband optical detection of ultrasound by two-wave mixing in a photorefractive crystal." *Applied physics letters* 59, no. 25 (1991).

[Kapadia 2006] Kapadia, Ajay. "Non destructive testing of composite materials." *TWI Ltd* (2006).

[Karabutov 2014] Karabutov, A. A., and N. B. Podymova. "Quantitative analysis of the influence of voids and delaminations on acoustic attenuation in CFRP composites by the laser-ultrasonic spectroscopy method." *Composites Part B: Engineering* vol. 56 (2014).

[Krautkrâmer 1990] Krautkrâmer, J., and H. Krautkrâmer. "Ultrasonic Testing of Materials." Springer Science & Business Media, (1990).

[Krehl 2008] Krehl, Peter OK. *History of shock waves, explosions and impact: a chronological and biographical reference*. Springer Science & Business Media, (2008).

[Krishnaswamy 2003] Krishnaswamy, Sridhar. "Theory and applications of laser-ultrasonic techniques." *Ultrasonic nondestructive evaluation: Engineering and biological material characterization.* CRC press, (2003).

[Kurahashi 2013] Kurahashi, S., Y. Shimada, O. Kotyaev, T. Norimatsu, Y. Kono, S. Nakata, and M. Ishii. "Measurement of depth of surface cracks in concrete by laser ultrasonic technique with multichannel detector." In *Review of Progress in Quantitative Nondestructive Evaluation: Volume 32*, AIP Publishing, vol. 1511, no. 1, (2013).

[Lindgren 2013] Lindgren, Erik, and Lars Hammar. "Evaluation of an automatic system for detection and positioning of small pore defects using digital radiography." In *Review of Progress in Quantitative Nondestructive Evaluation: Volume 32*, AIP Publishing, vol. 1511, no. 1 (2013).

[Malacara 2007] Malacara, Daniel, ed. *Optical shop testing*. Vol. 59. John Wiley & Sons, (2007).

[Mallick 2007] Mallick, Pankar K. *Fiber-reinforced composites: materials, manufacturing, and design*. CRC press, (2007).

[Mayer 2003] Mayer, T., D. Scherling, and J. Sun. "Shearography Testing On Aerospace Cfrp Components." *Journal of Nondestructive Testing* vol. 8, no. 2 (2003).

[Mercier 2009] Mercier, P., J. Bénier, P. A. Frugier, A. Sollier, M. Rabec Le Gloahec, E. Lescoute, J. P. Cuq-Lelandais et al. "PDV measurements of ns and fs laser driven shock experiments on solid targets." In *SHOCK COMPRESSION OF CONDENSED MATTER 2009: Proceedings of the American Physical Society Topical Group on Shock Compression of Condensed Matter*, AIP Publishing, vol. 1195, no. 1 (2009).

[Monchalin 1986] Monchalin, J-P. "Optical detection of ultrasound." *IEEE Transactions on Ultrasonics Ferroelectrics and Frequency Control* vol. 33 (1986).

[Monchalin 1993] Monchalin, Jean-Pierre. "Progress towards the application of laser-ultrasonics in industry." In *Review of Progress in Quantitative Nondestructive Evaluation*, Springer US, vol. 12A and 12B (1993).

[Néron 2013] Néron, C., C. Padioleau, A. Blouin, and J-P. Monchalin. "Robotic laser-ultrasonic inspection of composites." In *Review of Progress in Quantitative Nondestructive Evaluation: Volume 32*, AIP Publishing, vol. 1511, no. 1, (2013).

[Parga-Landa 1999] Parga-Landa, B., S. Vlegels, F. Hernandez-Olivares, and S. D. Clark. "Analytical simulation of stress wave propagation in composite materials." *Composite structures* vol. 45, no. 2 (1999).

[Park 2014] Park, Byeongjin, Yun-Kyu An, and Hoon Sohn. "Visualization of hidden delamination and debonding in composites through noncontact laser ultrasonic scanning." *Composites Science and Technology* vol. 100 (2014).

[Paul 1987] Paul, M., B. Betz, and W. Arnold. "Interferometric detection of ultrasound at rough surfaces using optical phase conjugation." *Applied physics letters* vol. 50, no. 22 (1987).

[Pelivanov 2015] Pelivanov, Ivan, Alex Shtokolov, Chen-Wei Wei, and Matthew O'donnell. "A 1 kHz a-scan rate pump-probe laser-ultrasound system for robust inspection of composites." *IEEE transactions on ultrasonics, ferroelectrics, and frequency control* vol.62, no. 9 (2015).

[Perton 2013] Perton, M., D. Lévesque, J-P. Monchalin, M. Lord, J. A. Smith, and B. H. Rabin. "Laser shockwave technique for characterization of nuclear fuel plate interfaces." In *Review of Progress in Quantitative Nondestructive Evaluation: Volume 32*, AIP Publishing, vol. 1511, no. 1, (2013).

[Phipps 1988] Phipps Jr, C. R., T. P. Turner, R. F. Harrison, G. W. York, W. Z. Osborne, G. K. Anderson, X. F. Corlis et al. "Impulse coupling to targets in vacuum by KrF, HF, and CO2 single-pulse lasers." *Journal of Applied Physics* vol. 64, no. 3 (1988).

[Pouet 1996] Pouet, Bruno F., R. K. Ing, Sridhar Krishnaswamy, and D. Royer. "Heterodyne interferometer with two-wave mixing in photorefractive crystals for ultrasound detection on rough surfaces." *Applied physics letters* vol. 69, no. 25 (1996).

[Radhakrishnan 2008] Radhakrishnan, J., M. Boustie, L. Berthe, Michel Arrigoni, and M. Jouiad. "Interfacial strength measurement of bonded aluminium foils by laser-driven shock waves." In *22nd Conference on Surface Modification Technologies* (2008).

[Ready 1971] Ready, John. *Effects of high-power laser radiation*. Elsevier, 2012.

[Rozmus 1990] Rozmus, W., and V. T. Tikhonchuk. "Skin effect and interaction of short laser pulses with dense plasmas." *Physical Review A,* vol. 42, no. 12 (1990).

[Salzmann 1989] Salzmann, D., I. Gilath, M. Givon, and T. Bar-Noy. "Measurement of the tensile strength of aluminium at a strain rate of 2× 107 s-1." *Journal of Physics D: Applied Physics* vol. 22, no. 9 (1989).

[Sarkissian 1978] Sarkissian, Karekin. "Adhesion measurement of thin films, thick films and bulk coatings." ASTM, (1978).

[Schmerr Jr 2012] Schmerr Jr, Lester W., Brady J. Engle, Alexander Sedov, and Xiongbing Li. "Ultrasonic flaw sizing—An overview." (2012).

[Scruby 1990] Scruby, Christopher B., and Leslie E. Drain. *Laser ultrasonics techniques and applications*. CRC Press, (1990).

[Sherman 2013] Sherman, Bradley, and Oluwaseyi Balogun. "Optical generation of high amplitude laser generated surface acoustic waves." In *Review of Progress in Quantitative Nondestructive Evaluation: Volume 32*, AIP Publishing vol. 1511, no. 1, (2013).

[Shim 2008] Shim, Jaewoo, Elizabeth Hagerman, Ben Wu, and Vijay Gupta. "Measurement of the tensile strength of cell–biomaterial interface using the laser spallation technique." *Acta biomaterialia* vol. 4, no. 6 (2008).

[Speight 1986] Speight, C. S., and P. F. Taylor. "Dynamic fracture criteria from free surface velocity measurements." *Metallurgical applications of shock-wave and high-strain-rate phenomena* (1986).

[Steinchen 1998] Steinchen, W., L. X. Yang, G. Kupfer, P. Mäckel, and F. Vössing. "Strain analysis by means of digital shearography: potential, limitations and demonstration." *The Journal of Strain Analysis for Engineering Design* vol. 33, no. 2 (1998).

[Summerscales 1994] Summerscales, John. "Manufacturing defects in fibre-reinforced plastics composites." *INSIGHT-WIGSTON THEN NORTHAMPTON-* vol. 36, no. 12 (1994).

[Sun 2013] Sun, Guangkai, Zhenggan Zhou, Xiucheng Chen, and Jie Wang. "Ultrasonic characterization of delamination in aeronautical composites using noncontact laser generation and detection." *Applied optics* vol. 52, no. 26 (2013).

[Swacek 2013] Swacek, C. B., J-Y. Kim, and L. J. Jacobs. "Optical excitation of narrowband Rayleigh surface waves for second harmonic generation." In *Review of Progress in Quantitative Nondestructive Evaluation: Volume 32*, AIP Publishing, vol. 1511, no. 1 (2013).

[Thomsen 1985] Thomsen, C., H. T. Grahn, H. J. Maris, and J. Tauc. "Ultrasonic experiments with picosecond time resolution." *Le Journal de Physique Colloques* vol. 46, no. C10 (1985).

[Wagner 1990] Wagner, JAMES W. "Optical detection of ultrasound." *Physical Acoustics* vol. 19 (1990).

[Web link a] *https://www.nde-ed.org/GeneralResources/MethodSummary/RT1.jpg*
Date visited 22nd November 2016.

[Web link b] *http://www.slideshare.net/Vetorix/vetorix-flash-thermography*
Date visited 22nd November 2016.

[Web link c] *http://www.twi-global.com/technical-knowledge/job-knowledge/ultrasonic-examination-part-1-127/*
Date visited 22nd November 2016.

[White 1963] White, Richard M. "Generation of elastic waves by transient surface heating." *Journal of Applied Physics* vol. 34, no. 12 (1963).

[Wilby 2012] Wilby, A. J., and D. P. Neale. "Defects introduced into Metals during Fabrication and Service." *Mater. Scie.* vol. 3 (2012).

[Yang 1974] Yang, L. C. "Stress waves generated in thin metallic films by a Q-switched ruby laser." *Journal of Applied Physics* vol. 45, no. 6 (1974).

[Yuan 1993 a] Yuan, J., and V. Gupta. "Measurement of interface strength by the modified laser spallation technique. I. Experiment and simulation of the spallation process." *Journal of Applied Physics* vol. 74, no. 4 (1993).

[Yuan 1993 b] Yuan, J., V. Gupta, and A. Pronin. "Measurement of interface strength by the modified laser spallation technique. III. Experimental optimization of the stress pulse." *Journal of Applied Physics* vol. 74, no. 4 (1993).

[Zhou 2003] Zhou, M., Y. K. Zhang, L. Cai, Z. H. Shen, X. R. Zhang, and S. Y. Zhang. "Optical interferometry diagnostics in laser-induced spallation on film–substrate systems." *Surface and Coatings Technology* vol. 165, no. 2 (2003).

Appendix

CYCOM® 5320-1 Epoxy Resin System

DESCRIPTION

CYCOM•5320-1 is a toughened epoxy resin prepreg system designed for vacuum-bag-only (VBO) or out of autoclave (OOA) manufacturing of primary structural parts. Because of its lower temperature curing capability, it is also suitable for prototyping where low cost tooling or VBO curing is required.

CYCOM 5320-1 handles like standard prepreg, yet can be vacuum bag cured to produce autoclave quality parts having very low porosity. It offers mechanical properties equivalent to other 350°F (177°C) autoclave-cured toughened epoxy prepreg systems after a 350°F (177°C) post-cure. The laminate can support a freestanding post-cure after an initial low temperature cure. The material can also be cured under positive pressure in an autoclave or press.

FEATURES AND BENEFITS

- Developed for aerospace primary and other structure
- Flexible cure cycles including vacuum bag only, autoclave and press molding
- Very low void content for vacuum bag only cure
- No autoclave required for cure, but autoclave cure options include low pressure autoclave cure and autoclave cure cycles compatible with other Cycom and adhesive products
- Excellent hot/wet and notched properties
- Mechanical properties equivalent to those of autoclave-cured toughened epoxy systems
- Long tack and shop life at room temperature
- Available in woven fabric and unidirectional tape formats including materials for AFP and ATL
- Optimized processing characteristics for both monolithic laminate and honeycomb sandwich parts
- Suitable for producing complex parts
- Low temperature cure capability enables the use of low cost tooling

SUGGESTED APPLICATIONS

- Primary and secondary structure aerospace applications
- Prototype structural part applications
- Vacuum Bay Only primary structure parts

CHARACTERISTICS

Table 1 | Resin Characteristics

Properties	Description
Shelf Life	1 year at < 10°F (-12°C)
Tack Life	20 days at room temperature
Shop Life	30+ days minimum at room temperature
Cured Resin Density, g/cc	1.31
Wet Glass Transition Temperature, °F (°C) [1]*	324 (163)
Average Moisture Uptake, wt %[2]	0.55

[1]Exposure: 24-hour water boil; Test Method: DMA, E' onset

[2]Exposure: 48-hour water boil; Dry at 250°F (121°C) for 24 hours.

* NOTE: Tg data are not applicable for U.S. export control classification or licensing. For export-related information please contact Cytec.

MECHANICAL PROPERTY DATA

Cycom 5320-1 prepregs are supported by an extensive set of multi batch mechanical and physical property databases. Product forms with supporting databases include:

- CYCOM® 5320-1 IM7 12K 145gsm 33% RW unidirectional tape – data available from Cytec on request
- CYCOM® 5320-1 T650-35 3K 8HS Fabric 36% RW - data available from Cytec on request
- CYCOM® 5320-1 IM7 PW Fabric 36% RW - data available from Cytec on request
- CYCOM® 5320-1 T650-35 3K PW Fabric 36% RW – data available from NCAMP
- CYCOM® 5320-1 T650-35 12K 145gsm 33% RW unidirectional tape – data available from NCAMP

NCAMP is the National Center for Advanced Materials Performance

https://www.niar.wichita.edu/NCAMPPortal/default.aspx

Selected data on the above referenced products along with other data are presented in Tables 2 through 6

Table 2 |Lamina Level properties – Unidirectional Tape

Material: CYCOM® 5320-1 IM7 12K 145gsm 33%

Prepreg: CYCOM ®5320-1/IM7 145/33

Fiber: Hexcel IM7 12K **Resin:** CYCOM ®5320-1

Cytec – CYCOM 5320-1/IM7 12K 145/33
Unidirectional Tape
Lamina Mechanical Properties Summary

Tg (dry): 386°F **Tg (wet[1]):** 321°F **Tg Method:** DMA (ASTM D7028, 35mm dual cantilever)

Processing: full vacuum, vacuum bag only room temperature for 16 hours plus integrated 200°F/350°F cure/post cure cycle with a 200°F cure for 10 hours followed immediately under the same vacuum bag by a post cure at 350°F for two hours.

Data reported as normalized (except where noted by parenthesis) by 0.0054 in. (59.9% nominal fiber volume)

Condition	-100°F Dry	75°F Dry	250°F Dry	300°F Dry	180°F Wet[1]	250°F Wet[1]
Property	Mean	Mean	Mean	Mean	Mean	Mean
0° Tensile						
ASTM D3039						
Strength (ksi)[2]	352.2	363.3	359.3		385.7	377.5
Modulus (Msi)	22.7	22.8	23.0		23.1	23.1
Poisson's Ratio	0.31	0.30	0.32		0.35	0.38
90° Tensile						
ASTM D3039						
Strength (ksi)	11.39	11.02	9.46		3.30	2.23
Modulus (Msi)	1.75	1.36	1.21		1.23	1.08
0° Compression						
ASTM D6641						
Strength (ksi)[2]	314.9	301.4	292.4		239.1	190.3
Modulus (Msi)	20.87	20.82	20.96		20.90	21.15
0°/90° Tensile						
ASTM D3039						
Strength (ksi)	189.7	192.5	189.1	185.8	203.1	197.6
Modulus (Msi)	12.30	12.08	12.24	12.07	12.38	12.18
0°/90° Compression						
ASTM D6641						
Strength (ksi)	169.6	159.7	153.9	127.6	125.9	99.6
±45° Tensile In-Plane Shear (500-3,000 µstrain chord)						
ASTM D3518						
0.2% Offset Strength (ksi)	(11.76)	(8.08)	(5.73)	(5.00)	(5.01)	(3.44)
Shear Modulus (Msi)	(0.98)	(0.80)	(0.72)	(0.70)	(0.67)	(0.53)
0° Short Beam						
ASTM D2344						
Strength (ksi)[3]		(19.4)				(8.8)

1 Wet conditioning to equilibrium at 85%RW and 160°F
2 Derived from 0°/90° strength results
3 250°F 2 hr. + 350°F 2 hr. cure

Table 3 | Laminate Level properties – IM7 unidirectional tape

Material: CYCOM® 5320-1 IM7 12K 145gsm 33%

Prepreg: CYCOM ®5320-1/IM7 145/33

Fiber: Hexcel IM7 12K **Resin:** CYCOM ®5320-1

Cytec – CYCOM 5320-1/IM7 12K 145/33 Unidirectional Tape Laminate Mechanical Properties Summary

Tg (dry): 386°F **Tg (wet[1]):** 321°F **Tg Method:** DMA (ASTM D7028, 35mm dual cantilever)

Processing: full vacuum, vacuum bag only room temperature for 16 hours plus integrated 200°F/350°F cure/post cure cycle with a 200°F cure for 10 hours followed immediately under the same vacuum bag by a post cure at 350°F for two hours.

Data reported as normalized (except where noted by parenthesis) by 0.0054 in. (59.9% nominal fiber volume)

Condition	-100°F Ambient	75°F Ambient	250°F Dry	300°F Dry	180°F Wet[1]	220°F Wet[1]	250°F Wet[1]
Property	Mean	Mean	Mean	Mean	Mean	Mean	Mean
Unnotched Tensile "Quasi" 25/50/25							
ASTM D3039							
Strength (ksi)	123.5	133.0		131.5	131.1		129.5
Modulus (Msi)	8.85	8.58		8.40	8.46		8.36
Unnotched Compression "Quasi" 25/50/25							
ASTM D6641							
Strength (ksi)	132.9	120.7		94.3	88.2		67.7
Modulus (Msi)	8.06	7.90		7.86	8.07		7.75
Interlaminar Tension (Angle Bend) "Quasi" 25/50/25							
ASTM D6415							
Strength (ksi)	(10.37)	(9.83)		(8.42)			(3.90)
Open Hole Tension "Quasi" 25/50/25							
ASTM D5766							
Strength (ksi)	72.6	75.7		75.3	76.7		73.9
Open Hole Compression "Quasi" 25/50/25							
ASTM D6484							
Strength (ks)	56.1	53.7		47.0	43.6	39.9	38.6

1 Wet conditioning to equilibrium at 85%RW and 160°F

Table 4 |Lamina Level Properties – T650-35 8 Harness Satin Fabric

Material: Cytec Aerospace Materials CYCOM® 5320-1 T650-35 3K 8HS Fabric 36%

Prepreg: CYCOM ®5320-1 T650-35 3K 8HS 36%

Fiber: Cytec T650/35 3k **Resin:** CYCOM ®5320-1

Cytec – CYCOM 5320-1/8HS T650/35 3k
8-Harness Satin Fabric
Lamina Mechanical Properties Summary

Tg (dry): 374°F **Tg (wet[1]):** 316°F **Tg Method:** DMA (ASTM D7028, 35mm dual cantilever)

Processing: full vacuum, vacuum bag only room temperature for 16 hours plus integrated 200°F/350°F cure/post cure cycle with a 200°F cure for 10 hours followed immediately under the same vacuum bag by a post cure at 350°F for two hours.

Data reported as normalized (except where noted by parenthesis) by 0.0145 in. (56.7% nominal fiber volume)

Condition	-100°F Dry	75°F Dry	250°F Dry	300°F Dry	180°F Wet[1]	250°F Wet[1]
Property	Mean	Mean	Mean	Mean	Mean	Mean
0° Tensile						
ASTM D3039						
Strength (ksi)	117.4	131.3	128.8		138.0	136.4
Modulus (Msi)	10.20	10.02	10.06		10.20	9.97
Poisson's Ratio	0.056	0.048	0.042		0.041	0.041
90° Tensile						
ASTM D3039						
Strength (ksi)	119.3	129.9	133.8	137.0	138.4	134.2
Modulus (Msi)	10.14	9.90	10.00	10.00	10.02	9.94
0° Compression						
ASTM D6641						
Strength (ksi)	121.1	108.8	93.9		77.6	66.0
Modulus (Msi)	10.01	9.18	9.24		9.23	9.18
90° Compression						
ASTM D6641						
Strength (ksi)	122.3	110.6	95.4	87.8	87.9	66.7
Modulus (Msi)	9.42	9.18	9.20	9.30	9.36	9.15
±45° Tensile In-Plane Shear (500-3,000 µstrain chord)						
ASTM D3518						
0.2% Offset Strength (ksi)	(12.13)	(8.29)	(5.67)	(4.72)	(5.23)	(3.31)
Shear Modulus (Msi)	(0.95)	(0.81)	(0.72)	(0.67)	(0.71)	(0.53)
0° Short Beam						
ASTM D2344						
Strength (ksi)	(12.39)	(11.93)	(9.68)	(8.51)	(8.66)	(6.45)

1 Wet conditioning to equilibrium at 85%RW and 160°F

TABLE 5 | Laminate level properties – 8 Harness Satin T650-35 Fabric

Material: Cytec Aerospace Materials CYCOM® 5320-1 T650-35 3K 8HS Fabric 36%

Prepreg: CYCOM ®5320-1 T650-35 3K 8HS 36%

Fiber: Cytec T650/35 3k **Resin:** CYCOM ®5320-1

Cytec – CYCOM 5320-1/8HS T650/35 3k
8-Harness Satin Fabric
Laminate Mechanical Properties Summary

Tg (dry): 374°F **Tg (wet[1]):** 316°F **Tg Method:** DMA (ASTM D7028, 35mm dual cantilever)

Processing: full vacuum, vacuum bag only room temperature for 16 hours plus integrated 200°F/350°F cure/post cure cycle with a 200°F cure for 10 hours followed immediately under the same vacuum bag by a post cure at 350°F for two hours.

Data reported as normalized (except where noted by parenthesis) by 0.0145 in. (56.7% nominal fiber volume)

	-100°F Ambient	75°F Ambient	250°F Dry	300°F Dry	180°F Wet[1]	250°F Wet[1]
Property	Mean	Mean	Mean	Mean	Mean	Mean
Unnotched Tensile "Quasi" 25/50/25						
ASTM D3039						
Strength (ksi)	90.3	96.0	97.5	99.7	89.6	89.1
Modulus (Msi)	7.38	7.12	7.09	7.02	7.04	6.80
Unnotched Compression "Quasi" 25/50/25						
ASTM D6641						
Strength (ksi)	114.2	97.5	77.6	70.3	71.3	60.3
Modulus (Msi)	6.88	6.68	6.69	6.48	6.50	6.42
Interlaminar Tension (Angle Bend) "Quasi" 25/50/25						
ASTM D6415						
Strength (ksi)	(9.61)	(8.40)	(7.14)	(6.68)		(4.04)
Open Hole Tension "Quasi" 25/50/25						
ASTM D5766						
Strength (ksi)	47.0	49.8	54.0	53.6	52.6	54.1
Open Hole Compression "Quasi" 25/50/25						
ASTM D6484						
Strength (ks)	55.4	50.7	44.0	40.3	40.4	35.0

1 Wet conditioning to equilibrium at 85%RW and 160°F

TABLE 6 | Compression After Impact Properties – T40-800B Unidirectional Tape, 145gsm 33%RW 250°F CURE; 350°F Postcure

Properties	Test Method Lay Up	Condition	Results
Compression After Impact Residual Strength, ksi (MPa))	ASTM D7137 or SACMA SRM02R94	RTA	25.6 (176)

CURE CYCLE FLEXIBILITY – T40-800B Unidirectional Tape, 145gsm, 33%RW, Low Temperature Initial Cures Followed by 350°F Postcure

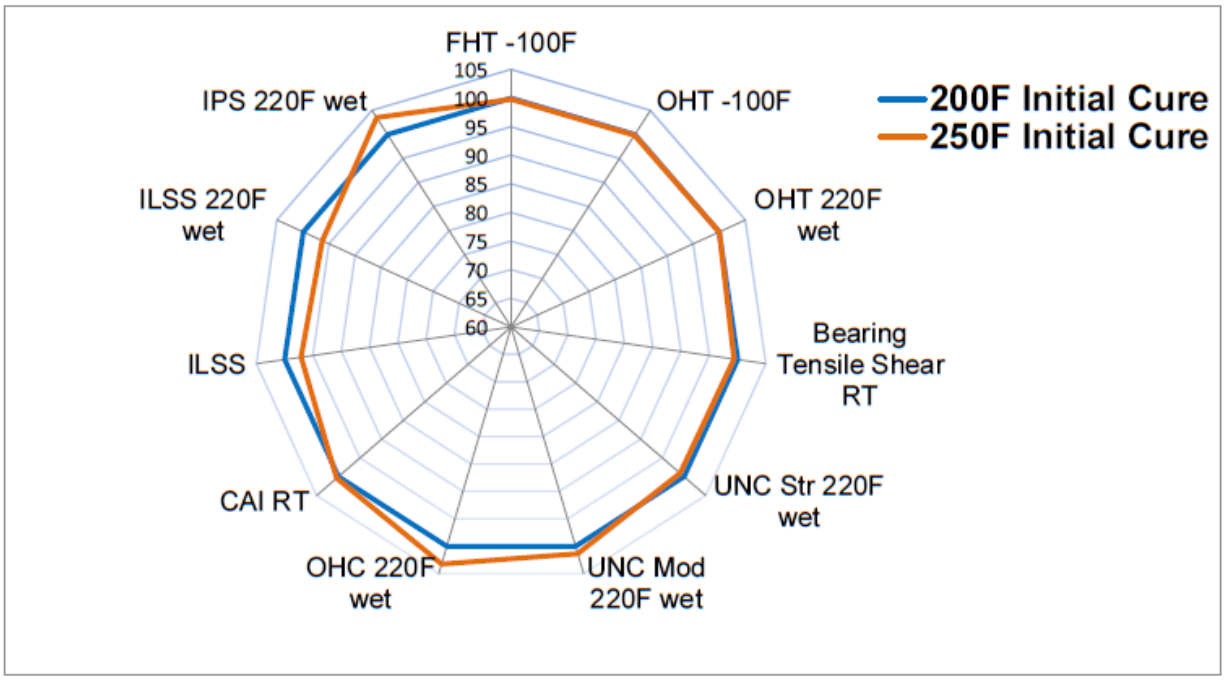

SUGGESTED PROCESSING PARAMETERS

CURE CYCLES

CYCOM•5320-1 offers flexible cure cycle capability. Typical Vacuum Bag Only (VBO) Cure cycles:

Cure Cycle A: Serial Production VBO Cure Cycle:

Heat to 140±5° F for 120±10 minutes; Ramp at 2±1° F per minute to 250±10° F; Hold at 250±10° F for 120±10 minutes; Ramp at 3±1° F per minute to 350±10° F; Hold at 350±10° F for 120±10 minutes; Cool at <10° F to below 140° F.

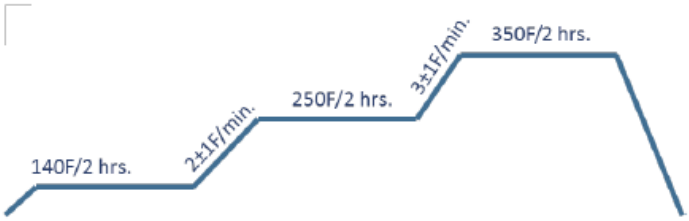

Cure Cycle B: Low Temperature 250°F Initial VBO Cure; Free Standing Post-Cure to 350°F:

Heat to 140±5° F for 120±10 minutes; Ramp at 2±1° F per minute to 250±10° F; Hold at 250±10° F for 120±10 minutes; Cool at <10° F to below 140° F. Ramp at 0.1 to 0.5° F per minute to 350±10° F; Hold at 350±10° F for 120±10 minutes; Cool at <10° F to below 140° F.

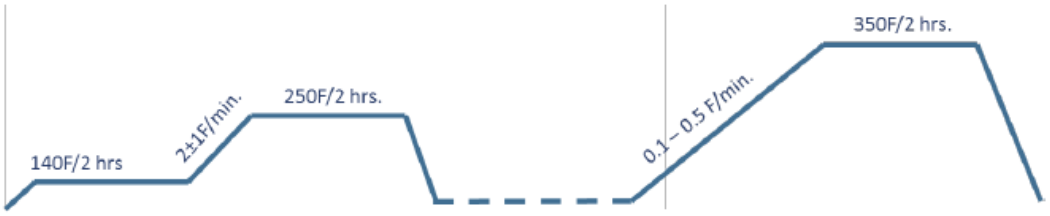

Cure Cycle C: 200°F Low Temperature VBO Initial Cure; Free Standing Post-Cure to 350°F

Heat to 140±5° F for 120±10 minutes; Ramp at 2±1° F per minute to 200±10° F; Hold at 250±10° F for 10 hours ± 10 minutes; Cool at <10° F to below 140° F. Ramp at 0.1 to 0.5° F per minute to 350±10° F; Hold at 350±10° F for 120±10 minutes; Cool at <10° F to below 140° F.

AUTOCLAVE OR POSITIVE PRESSURE CURES

Cycom 5320-1 may be cured under positive pressure in an autoclave or via a bladder or press process. Please contact Cytec for specific processing recommendations.

KINETIC MODEL

The RAVEN Simulation Software by Convergent Manufacturing Technologies, Inc. has characterized several Cytec VBO resin and compatible adhesive systems in their kinetic modeling software. CYCOM 5320-1 VBO resin systems have been characterized in the RAVEN software and are included in a site license for the software.

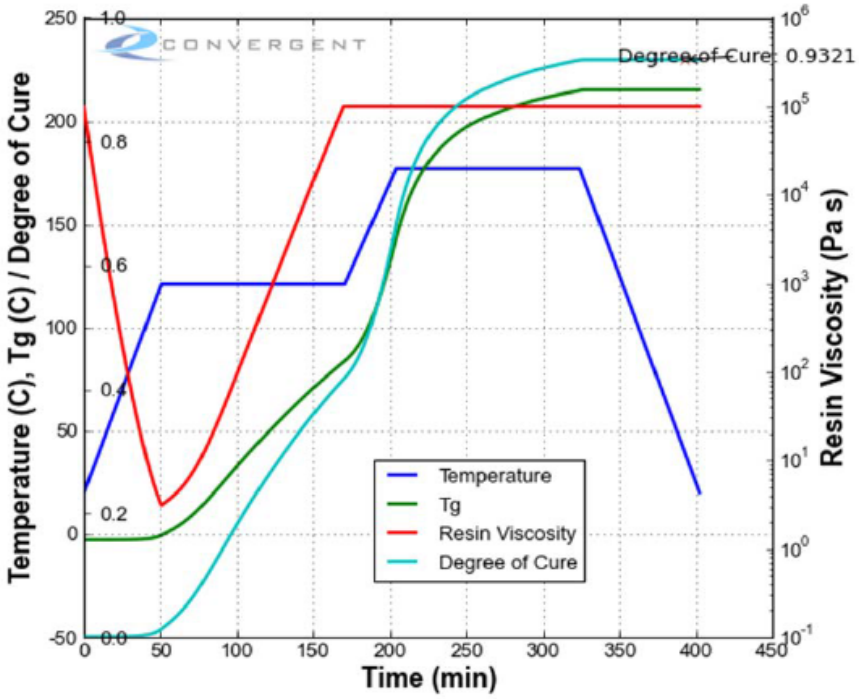

Kinetic Model Output Example For CYCOM 5320-1 (RAVEN® Simulation Software by Convergent Manufacturing Technologies, Inc.)

DEBULKING

Vacuum room temperature debulking cycles are not required to eliminate voids for flat or mildly contoured parts. Debulking should be performed as necessary to eliminate wrinkles and bridging of materials in highly contoured or very thick parts.

VACUUM REQUIREMENT

For vacuum bag only cures, vacuum should be less than 2" of Hg (68 mbar) of absolute vacuum for the given altitude. At sea level a minimum of 28" of Hg (948.2 mbar) is recommended. Shop vacuum is not recommended for use on VBO cured laminates.

LEAK CHECK

A vacuum leak check should be performed prior to cure and heat-up. The test should not be more than a 1" of Hg (34 mbar) vacuum loss in 10 minutes.

VACUUM BAG ARRANGEMENT FOR CURE

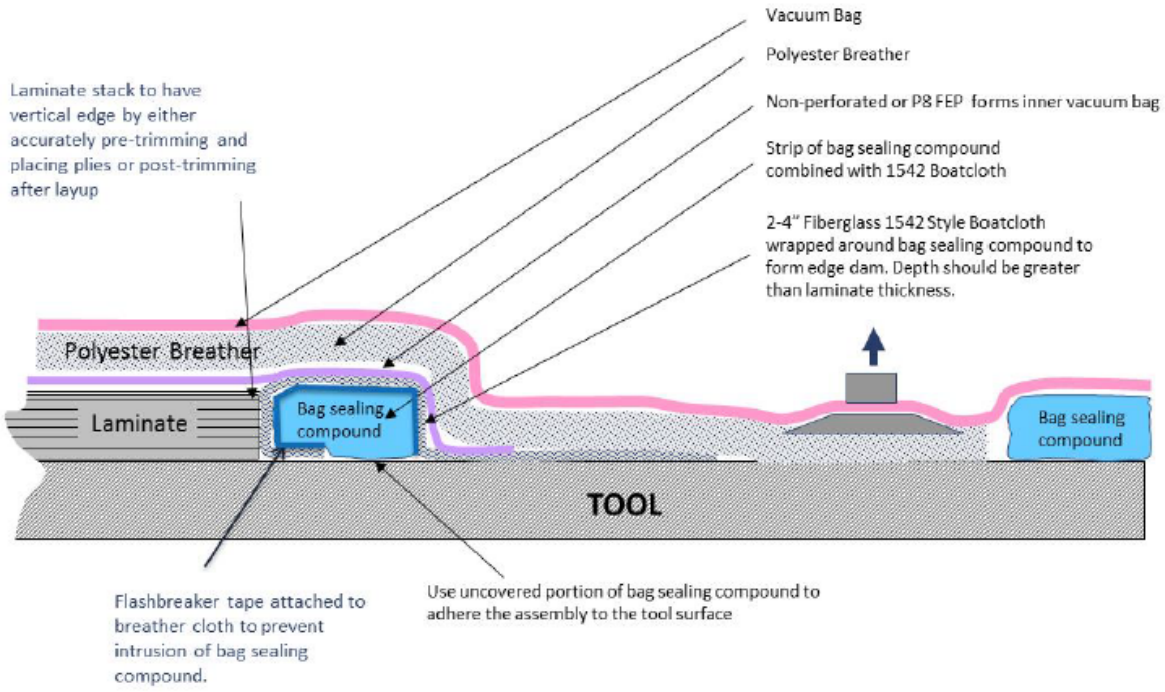

Bagging Material Notes

(1) Any breather material may be used (e.g., A3000-4, A3000-7, 7781 glass, etc.) as long as it effectively removes the air and can withstand temperatures and pressures.

(2) Non perforated solid release film is recommended although the use of perforated release film such as P8 is also possible.

(3) The sealant tape and fiberglass cloth can be exchanged for cork, silicone or any other type of stiff dam as long as there are sufficient breather strings against the edges of the laminate that connect to the breather. The strings should have a twist in them and be placed on all edges between the dam and the laminate. Also note that the edge dams need to be higher than the laminate thickness.

(5) Edge to be trimmed square unless lay-up produces a square edge.

VACUUM COMPATIBLE PROCESSING MATERIALS

The following materials are recommended for use with CYCOM 5320-1. For additional information please contact your Cytec Aerospace Materials Representative.

Table 7 | Compatible Adhesive Materials and Surfacing Film

Film Adhesive	FM 209-1, FM 309-1, FM 300-2
Surfacing Film	SURFACE MASTER 905M

Table 8 | Processing Materials

Sealant Tape	SM5142, SM5153
Breather	A3000-4, A3000-7, Code 4819
Release Film	VacPak A6200, 0.001 inch or 0.0006 inch
Bagging Film	Vacfilm 450V, 0.002 inch or 0.003 inch
Flash Tape	Flash Tape 1, Flash Tape 2

PRODUCT HANDLING AND SAFETY

Cytec Industries Inc. recommends wearing clean, impervious gloves when working with uncured prepreg to reduce skin contact and to avoid contamination of the product. Materials Safety Data Sheets (MSDS) and product labels are available upon request and can be obtained from www.cytec.com or any Cytec location supplying aerospace materials.

DISPOSAL OF SCRAP MATERIAL

Disposal of scrap material must be in accordance with local, state, and federal regulations.

CONTACT INFORMATION

Global Product Referral
tel: 1 800 652 6013 – USA
tel: +1 973 357 3193 – Outside the USA
email: custinfo@cytec.com

DISCLAIMER: The data and information provided in this document have been obtained from carefully controlled samples and are considered to be representative of the product described. Cytec does not express or imply any guarantee or warranty of any kind including, but not limited to, the accuracy, the completeness or the relevance of the data and information set out herein. Because the properties of this product can be significantly affected by the fabrication and testing techniques employed, and since Cytec does not control the conditions under which its products are tested and used, Cytec cannot guarantee the properties provided will be obtained with other processes and equipment. No guarantee or warranty is provided the product is adapted for a specific use or purpose. Cytec declines any liability with respect to the use made by any third party of the data and information contained herein. Cytec has the right to change any data or information when deemed appropriate.
All trademarks are the property of their respective owners.